Shedding Light on the Dark: Exploring the Relation Between Galaxy Cluster Mass and Temperature Through Weak Gravitational Lensing

by

Rutuparna Das

A dissertation submitted in partial fulfillment
of the requirements for the degree of
Doctor of Philosophy
(Physics)
in The University of Michigan
2018

Doctoral Committee:

Professor Gregory Tarlé, Chair
Professor Dragan Huterer
Associate Professor Christopher John Miller
Professor Kathy Romer, University of Sussex

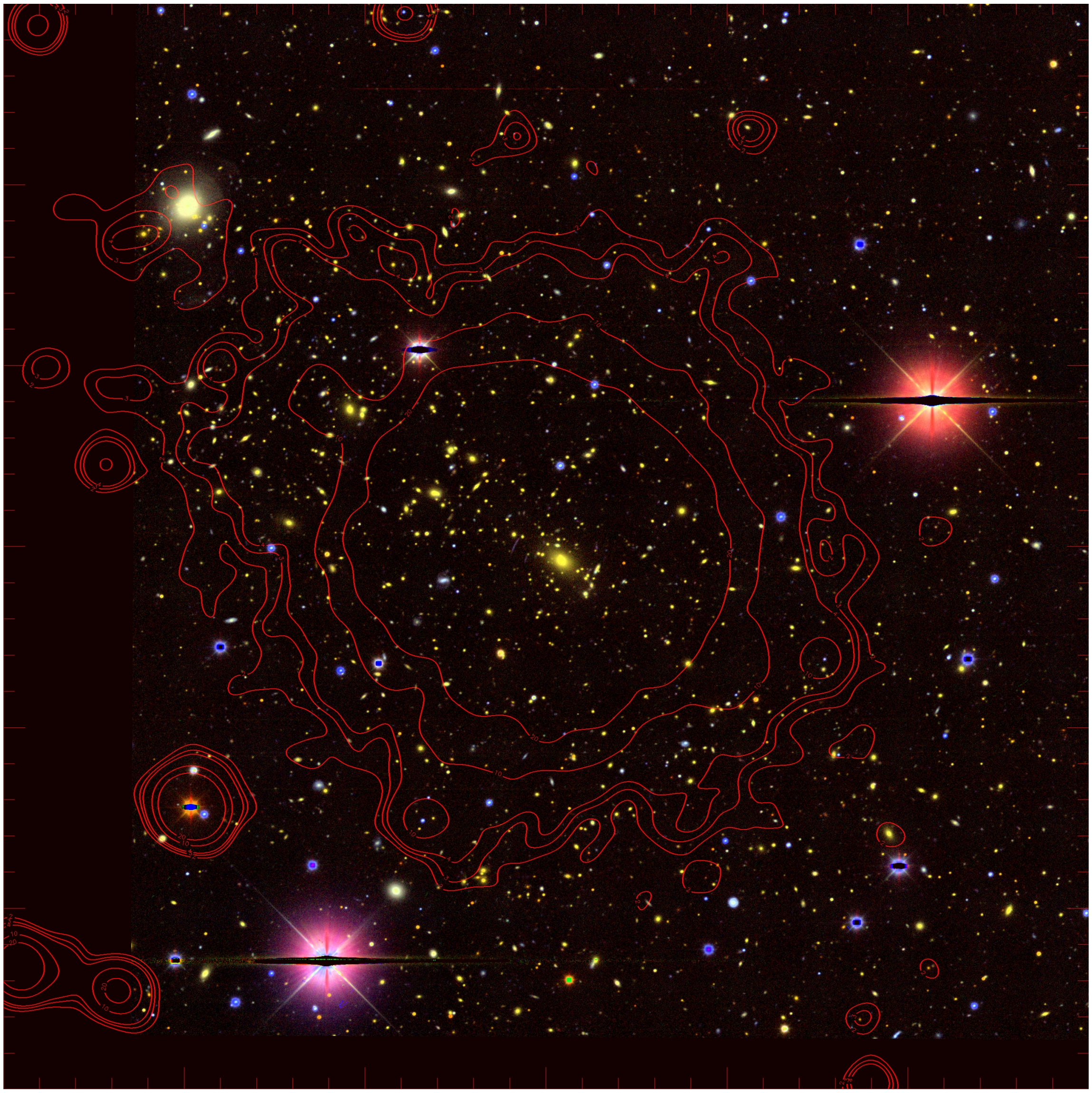

A cluster of galaxies in all its multi-wavelength glory.

Rutuparna Das

rutudas@umich.edu

ORCID iD: 0000-0003-0272-9949

To my family,
for being unwaveringly by my side
through my wanderings of the universe...

And to the universe,
for letting me wander it.

ACKNOWLEDGEMENTS

The stereotypical scientist sits alone in the depths of a lab, kept company only by equations and equipment and the occasional "Eureka!" The real scientist, on the other hand, is surrounded, supported, and kept sane by mentors, colleagues, friends, and family—it takes a village to raise a PhD. I would like to take a few pages here to thank my village.

I must start by thanking my wonderful advisor, Greg Tarllé. From enticing me with pictures of the Chilean night sky the first time I met him, to introducing me to weak lensing as a direct probe of the amazing balancing act between matter and dark energy, to the years of mentorship that followed, Greg has continuously inspired me to study the universe with both rigor and wonder. The next person to thank is Chris Miller, who has pretty much been a second advisor to me. From introducing me to the project that would become my thesis, to guiding me in the art of evaluating data and methods with an analytical eye, Chris has been a constant source of ideas and encouragement through the past several years.

I would like to thank Dragan Huterer and Kathy Romer, not just for making up the rest of my committee, but also for their influence throughout my graduate career. I will always remember Dragan for giving me my first taste of observational studies of dark energy through his class, and for instilling in me an appreciation for the importance of proper handling of uncertainties. Kathy has been an invaluable mentor, from helping with all things clusters and XCS, to pushing me to communicate

and ask for help when needed, to encouraging not only my research but also my efforts in outreach.

The UM Dark Energy Survey group has been a wonderful source of support and ideas. I would like to thank Dave Gerdes, Gus Evrard, Michael Schubnell, and Tim McKay, for their guidance and mentorship through the years. My friends at UM, both within DES and not, have been an invaluable source of camaraderie and support—I will always be grateful to Yuanyuan and Tomasz for showing me the ropes when I first joined, helping me navigate through general cosmology as well as DES policies and data access. Thanks to Anthony, Stephanie, Arya, Jessie, Kevin, Paige, Karishma, and Meryl, and many, many others, for all the conversations and memories.

A cosmic thank you to the Dark Energy Survey Collaboration for being my scientific family for the past six years. I am especially grateful to the Clusters and Weak Lensing working groups, as well as the folks working with XCS. Special shout-out to Joe Zuntz for his incredible patience in guiding me through the measurement of galaxy shapes. I am forever grateful to Tom Diehl for giving me the opportunity to be an observer and run manager, letting me experience the wonder of the DES sky first-hand, and to the team at CTIO for all their help as I did so. DES has also given me the opportunity to meet, work with, and represent an amazing set of early career scientists—I have gained many friends, and look forward to staying in touch as we all move forth in our careers and lives.

I thank the United States Department of Energy (and all the wonderful taxpayers out there) for funding my work and allowing me to pursue my explorations of the universe. I also thank the University of Michigan Department of Physics, not only for several semesters of funding, but also for providing me with an incredibly supportive environment in which to work.

I now turn to those beautiful people who have both shared my joys and given me the strength to keep going through the most difficult parts of these past few years, the family and friends who have been staunchly by my side through this exercise in learning. I must start by thanking my parents—I would not be the person I am today if not for them. My father taught me to wonder at the universe, to always seek to learn, and to forever keep a positive outlook. My mother showed me the value and power of hard work, and kept me going with her constant encouragement and support, not to mention several well-timed care packages. Thanks to Kanha for making sure I never take life too seriously. Thanks to all the wonderful members of my extended family (too many to name individually—their numbers rival those of my scientific family!) for keeping me grounded to what really matters, getting me to lighten up whenever I got too tense, and being very understanding when I failed to return calls for months on end. Thanks to all the friends who have stuck with me from the various walks of my life, who have always been willing to provide a listening ear, a welcome distraction, or a much-needed hug. Finally, I come to the person who has stood by me no matter what, who has challenged and encouraged me to be better than I believed I could, who has never failed to make me smile—thank you, Atulya, for so, so much more than I can ever hope to express. You make my universe go round.

TABLE OF CONTENTS

DEDICATION . . . ii

ACKNOWLEDGEMENTS . . . iii

LIST OF FIGURES . . . viii

LIST OF TABLES . . . x

LIST OF APPENDICES . . . xii

ABSTRACT . . . xiii

CHAPTER

I. Introduction . . . 1

1.1 Dissertation Overview . . . 2
1.2 Modern Observational Cosmology . . . 3
1.2.1 Probes of Dark Energy . . . 4
1.3 Galaxy Clusters . . . 6
1.3.1 Anatomy of a Cluster . . . 8
1.3.2 Cluster Cosmology . . . 9
1.3.3 Direct Measurements of Cluster Mass . . . 10
1.3.4 Cluster Finding and Mass Proxies . . . 16
1.4 The Dark Energy Survey (DES) . . . 20
1.4.1 Star-Galaxy Separation . . . 21
1.4.2 Photometric Redshifts . . . 22
1.5 The DES-SV-XCS Cluster Sample . . . 22
1.5.1 Cluster X-Ray Temperatures . . . 23
1.6 DES Simulated Sample . . . 24

II. Galaxy Shape Measurements . . . 25

2.1 Galaxy Shapes from the Dark Energy Survey . . . 26
2.1.1 Im3shape . . . 28
2.2 Shapes for the DES-SV-XCS Cluster Sample . . . 29
2.2.1 Validating Additional Catalogs . . . 31
2.2.2 Accessing Additional Catalogs . . . 32
2.3 Summary . . . 37

III. Stacked Cluster Weak Lensing Masses . . . 38

3.1 Clusters and Weak Lensing . . . 40
3.1.1 Halo Mass Profile . . . 40

3.1.2 Shear and Surface Mass Density Contrast . . . 41
3.1.3 From Shapes to $\Delta\Sigma$ . . . 42
3.2 Data . . . 43
3.3 Cluster Stacking . . . 46
3.4 Measuring the Stacked Lensing Signal . . . 52
3.4.1 Galaxy Selection . . . 54
3.4.2 $\Delta\Sigma$ Errors . . . 57
3.5 Modeling the Stacked Lensing Profile . . . 58
3.5.1 Modeling $\Delta\Sigma$ for a Cluster Stack with a Wide z Range and Uneven Data . . . 59
3.6 Stacked Weak Lensing Masses . . . 64
3.7 Testing the Stacked WL Masses . . . 66
3.7.1 Analysis Pipeline Validation . . . 66
3.7.2 Shear Profile Tests . . . 70
3.7.3 Cluster Contamination Check . . . 73
3.8 Discussion and Summary . . . 75

IV. The Galaxy Cluster Mass-X-ray Temperature Scaling Relation . . . 78

4.1 Scaling Relation Model . . . 79
4.2 Bayesian Framework and Likelihood Model . . . 80
4.3 Cluster Mass and Temperature Data . . . 82
4.4 The Measured Scaling Relation . . . 84
4.5 Scaling Relation Variations . . . 86
4.5.1 BCG Centering . . . 86
4.5.2 Non-core-excised Temperatures . . . 91
4.6 Discussion and Summary . . . 96
4.6.1 Future Prospects . . . 98

V. Conclusion . . . 102

APPENDICES . . . **106**

BIBLIOGRAPHY . . . **119**

LIST OF FIGURES

Figure

1.1 Recent constraints on cosmological parameters . . . 7
1.2 Color-magnitude diagrams of a cluster . . . 9
1.3 Observed mass function using data from the Chandra X-ray Telescope . . . 10
1.4 Sensitivity of cluster abundances to over time to variations in Ω_M and w_{DE} . . . 11
1.5 Constraints on cosmological parameters w_0 and Ω_{DE} . . . 12
1.6 The (exaggerated) weak lensing effect of a lens on observations of a field of background galaxies . . . 14
1.7 Scaling relations between optical observables and cluster mass . . . 17
1.8 Scaling relations between CMB observables and cluster mass . . . 18
1.9 Scaling relations between X-ray observables and cluster mass . . . 19
2.1 Positions of clusters in our sample . . . 30
2.2 Comparison of official DES-SV IM3SHAPE catalog to GREAT-DES simulations . . . 32
2.3 Comparison of official DES-SV IM3SHAPE catalog to runs of IM3SHAPE on additional areas of sky. . . . 33
2.4 More comparisons of official DES-SV IM3SHAPE catalog to runs of IM3SHAPE on additional areas of sky. . . . 34
2.5 Area covered by catalogs provided . . . 36
3.1 Image of cluster with overlaid optical and X-ray data . . . 44
3.2 Cluster to be excluded due to nearby structure . . . 45
3.3 Temperature and redshift distributions of our four cluster bins . . . 51
3.4 Color-magnitude diagrams of a cluster, overlaid with colorcuts. . . . 56
3.5 Comparison between variations in non-parametric bootstrap sampling for errors . . . 58
3.6 Temperature and redshift distributions of our four cluster bins, unweighted . . . 61
3.7 Temperature and redshift distributions of our four cluster bins, weighted . . . 62
3.8 Comparison between two types of modeling of theoretical $\Delta\Sigma$ profiles. . . . 65
3.9 Best-fit $\Delta\Sigma$ profiles, overlaid on the measured $\Delta\Sigma$ values . . . 67
3.10 Analysis tested on simulated sample from Buzzard v1.1 . . . 69
3.11 Code check with XSHEAR . . . 70
3.12 Robustness checks on our lensing signal . . . 72
3.13 Testing for contamination of the $\Delta\Sigma$ signal by cluster members . . . 74
3.14 Sparse and dense galaxy fields . . . 76
4.1 Comparison of cluster mass-temperature scaling relations from various existing studies. . . . 79
4.2 Measured $M - T_x$ scaling relation . . . 85
4.3 Separations between X-ray and BCG centers . . . 91
4.4 Lensing signals and best-fit models using BCG centering . . . 92
4.5 Comparing measured $M - T_x$ scaling relations: using X-ray barycenters vs BCGs as cluster centers . . . 93
4.6 Comparison between core-excised and non-core-excised cluster temperatures . . . 94
4.7 Comparing measured $M - T_x$ scaling relations: using core-excised vs non-core-excised temperatures . . . 95
4.8 Our measured $M - T_x$ scaling relation, compared with previous literature . . . 97

4.9 Our measured $M - T_x$ scaling relations, using both core-excised and non-core-excised temperatures, compared with previous literature 99
5.1 Inspiration 105

LIST OF TABLES

Table

3.1 List of clusters excluded from weak lensing analysis due to nearby structure. 46

3.2 The set of clusters used in this work - the DES-SV-XCS cluster sample, excluding clusters with large structures nearby. Column 1 is the cluster name given by XCS, and column 2 gives the DES tiling in which it is observed. Columns 3 and 4 give the position of the cluster's X-ray barycenter. Column 5 is the cluster redshift. Columns 6-8 give the X-ray temperature, along with upper and lower bounds on uncertainties. Columns 9-13 give the cluster color through various combinations of filters. 47

3.3 Table 3.2, contd. The set of clusters used in this work - the DES-SV-XCS cluster sample, excluding clusters with large structures nearby. Column 1 is the cluster name given by XCS, and column 2 gives the DES tiling in which it is observed. Columns 3 and 4 give the position of the cluster's X-ray barycenter. Column 5 is the cluster redshift. Columns 6-8 give the X-ray temperature, along with upper and lower bounds on uncertainties. Columns 9-13 give the cluster color through various combinations of filters. 48

3.4 Table 3.2, contd. The set of clusters used in this work - the DES-SV-XCS cluster sample, excluding clusters with large structures nearby. Column 1 is the cluster name given by XCS, and column 2 gives the DES tiling in which it is observed. Columns 3 and 4 give the position of the cluster's X-ray barycenter. Column 5 is the cluster redshift. Columns 6-8 give the X-ray temperature, along with upper and lower bounds on uncertainties. Columns 9-13 give the cluster color through various combinations of filters. 49

3.5 Table 3.2, contd. The set of clusters used in this work - the DES-SV-XCS cluster sample, excluding clusters with large structures nearby. Column 1 is the cluster name given by XCS, and column 2 gives the DES tiling in which it is observed. Columns 3 and 4 give the position of the cluster's X-ray barycenter. Column 5 is the cluster redshift. Columns 6-8 give the X-ray temperature, along with upper and lower bounds on uncertainties. Columns 9-13 give the cluster color through various combinations of filters. 50

3.6 Properties of the stacked T_x bins. Column 1 names each bin, for ease of referral henceforth. Column 2 gives the size of each bin, and columns 3 and 4 give the lowest and highest temperatures in each bin. 52

3.7 Details of radial bins for each stack. Column 1 is the stack id, and column 2 gives the width of each radial bin in that stack. Column 3 gives the center of the first radial bin (if this is shorter than half the bin width, then the first bin stretches from 0 to half the bin width beyond this value), and column 4 gives the number of radial bins used. 53

3.8 Best-fit M_{500} for each stack. Column 1 is the stack id, column 2 gives the best-fit mass, and columns 3 and 4 give the lower and upper bounds respectively on 1σ uncertainties. 66

4.1 Results of Bayesian analysis of cluster mass-temperature scaling relation. We present our primary results, using core-excised temperatures and assuming the X-ray barycenter to be the true cluster center. In addition, we present results of variations in our data: using non-core-excised temperatures, centering on BCGs. See Section 4.5 for further details on the variations. 85
4.2 Additional data for the DES-XCS cluster sample, along with selected data from Tables 3.2-3.5. Column 1 is the cluster name given by XCS, and column 2 gives the DES tiling in which it is observed. Columns 3 and 4 give the position of the cluster's X-ray barycenter, and columns 5 and 6 give the position of the BCG. Columns 7-9 give the core-excised (CE) X-ray temperature, along with upper and lower bounds on uncertainties, and columns 10-12 give the same for non-core-excised (NCE) temperatures. 87
4.3 Table 4.2, contd. Additional data for the DES-XCS cluster sample, along with selected data from Tables 3.2-3.5. Column 1 is the cluster name given by XCS, and column 2 gives the DES tiling in which it is observed. Columns 3 and 4 give the position of the cluster's X-ray barycenter, and columns 5 and 6 give the position of the BCG. Columns 7-9 give the core-excised (CE) X-ray temperature, along with upper and lower bounds on uncertainties, and columns 10-12 give the same for non-core-excised (NCE) temperatures. 88
4.4 Table 4.2, contd. Additional data for the DES-XCS cluster sample, along with selected data from Tables 3.2-3.5. Column 1 is the cluster name given by XCS, and column 2 gives the DES tiling in which it is observed. Columns 3 and 4 give the position of the cluster's X-ray barycenter, and columns 5 and 6 give the position of the BCG. Columns 7-9 give the core-excised (CE) X-ray temperature, along with upper and lower bounds on uncertainties, and columns 10-12 give the same for non-core-excised (NCE) temperatures. 89
4.5 Table 4.2, contd. Additional data for the DES-XCS cluster sample, along with selected data from Tables 3.2-3.5. Column 1 is the cluster name given by XCS, and column 2 gives the DES tiling in which it is observed. Columns 3 and 4 give the position of the cluster's X-ray barycenter, and columns 5 and 6 give the position of the BCG. Columns 7-9 give the core-excised (CE) X-ray temperature, along with upper and lower bounds on uncertainties, and columns 10-12 give the same for non-core-excised (NCE) temperatures. 90
4.6 Best-fit M_{500} for each stack, centered on cluster BCGs. Column 1 is the stack id, column 2 gives the best-fit mass, and columns 3 and 4 give the lower and upper bounds respectively on 1σ uncertainties. 91

LIST OF APPENDICES

Appendix

A. Accessing and Using LensStack . . . 107
A.1 Python and Package Requirements . . . 108
A.2 Running LensStack . . . 109
A.2.1 Required Inputs . . . 109
A.2.2 Outputs . . . 113
B. Running Im3shape . . . 114
B.0.1 Necessary repositories/modules/programs: . . . 114
B.0.2 Steps to Measure Shapes . . . 115

ABSTRACT

The evolution of the abundance of galaxy clusters is a powerful tool for quantifying the presence of dark energy in the universe. To use this tool, it is necessary to measure precise cluster masses. As masses are difficult to measure directly, this often requires understanding the scaling relation between mass and one of several observables. In this dissertation we work with optical data from the Dark Energy Survey's Science Verification (DES-SV) run and X-ray data from the XMM Cluster Survey to examine the scaling relation between cluster mass and X-ray temperature. As our mass measurements are derived using weak gravitational lensing, the first component of this thesis describes the measurement of galaxy shapes, a necessary step in lensing studies. In the process of gathering data to cover our entire cluster sample, we measure ellipticities of approximately 590,000 galaxies, and make this additional data public to complement the official DES-SV shape catalog. The second component of the dissertation describes our measurement of stacked weak lensing masses of 133 clusters. As SV data quality varies over different parts of the sky, we develop a method for modeling observations that accounts for inhomogeneous data quality. This method makes it possible to incorporate clusters with partial data into lensing analyses. In the final section, we constrain the galaxy cluster mass-temperature scaling law, and find it to be consistent with the self-similar model and with previous measurements in the literature. We also examine the effect on the scaling relation of several variations on the data.

CHAPTER I

Introduction

Humans have been curious about the universe since the dawn of our race. The earliest records of this astronomical curiosity are related to timekeeping, from bone sticks dating back to 32,000 BCE Africa and Europe recording the phases of the moon to calendars from an array of ancient civilizations centered around the movements of the moon and Sun. Incorporating celestial measurements into architecture, the ancient Egyptians align the pyramids by the pole star, and orient the Great Temple to match the rising of the sun at the winter solstice. A precursor to object catalogs, the bread and butter of modern cosmology, is found in 2nd millenium BCE Babylon—a catalog of planets, stars, and constellations, amassed from several earlier sources. Chinese astronomers record the appearance of twenty possible supernovae in the 1st millenium CE.

We next remember the ancient Greek philosophers, who represent the celestial motions using epicycles and propose the first-known heliocentric model of the solar system. In the 4th-5th century CE, we find astounding astronomical accuracy in the Indian text *Surya Siddhanta*, which calculates the sidereal year to within three minutes, the moon's period to within a second, and the diameters of Mercury and Saturn to within 1%. A few centuries later, civilizations around the world record a "guest star"—the supernova that created the crab nebula.

In more recent times, we search the skies with the likes of Tycho Brahe, whose mind-bogglingly meticulous records of celestial objects allow his student, Johannes Kepler, to model planetary motion. With improvements in early telescopes, we discover the moons of Jupiter with Galileo Galilei and develop a classical theory of gravitation with Isaac Newton.

Over the last few centuries, we observe our universe through the eyes of ever-increasing numbers of scientists. We discover the rest of the planets in our backyard—modifying the definition of a planet along the way—and look far further out to probe the properties of every type of astrophysical object, from supernovae to distant galaxies. We attempt to comprehend the complexities of gravity and find it to be embedded in the very fabric of space. We look to the earliest moments of the cosmos and endeavor to understand its conception and growth and composition. We discover unthinkably massive structures—clusters of galaxies—at the nodes of an even vaster cosmic web.

Upon learning of the expansion of the universe, we set out to measure how it slows and when it will collapse, only to find to our utter astonishment that it is somehow, inconceivably—impossibly—accelerating.

1.1 Dissertation Overview

Humanity's legacy of curiosity about the universe is exemplified today by the endeavor to quantify dark energy, the name given to the invisible source of negative pressure causing the universe to accelerate, and to understand the history (and perhaps the future) of cosmic expansion. This dissertation focuses on characterizing the relation between galaxy cluster mass and temperature, a step on the path to characterizing dark energy using clusters of galaxies. The next few sections give an overview of modern observational cosmology, focusing in particular on galaxy clusters and methods of observing them. The last few sections of this chapter discuss the datasets used throughout this work. Chapter II focuses on measuring and validating galaxy shapes for weak lensing measurements, and presents measured shape catalogs for public use. Chapter III discusses our cluster weak lensing analysis, including a method we develop to account for inhomogeneities in cluster data, and provides the resulting cluster masses. Chapter IV covers our constraining and examination of the cluster mass-temperature scaling law.

1.2 Modern Observational Cosmology

In our efforts to understand and quantify the cosmos, we divide its energy density into four components: matter, radiation, dark energy, and curvature. The energy density of a flat universe, where there is no curvature, is called the critical density. The "energy budget," or total energy of the universe, can be written as the sum of the energy densities of each of these components relative to the critical density:

$$\Omega_M + \Omega_r + \Omega_{DE} - \Omega_k = 1 \tag{1.1}$$

where Ω_i is the energy density of the component i, divided by the critical density of the universe, and M, r, DE, and k represent matter, radiation, dark energy, and curvature, respectively. The expansion rate of the universe, $H(z)$, can be expressed as:

$$H^2(z) = H_0^2\Big[\Omega_M(1+z)^3 + \Omega_r(1+z)^4 + \Omega_{DE}(1+z)^{3(1+w_{DE})} + \Omega_k(1+z)^2\Big] \tag{1.2}$$

where z denotes the redshift, a measure of time. $z = 0$ signifies present day, making H_0 the current expansion rate of the universe. The exponents of each term dictate how each component affects the expansion rate as time goes by. Note that for dark energy, this exponent is defined in terms of a variable w_{DE}, the dark energy equation of state, defined as the ratio of its pressure to its energy density. In fact, all components affect the expansion rate according to their equations of state; however, w_i for the other components is well understood, leading to the exponents above.

w_{DE} is one of the main parameters used to quantify dark energy. It can be written as the sum of two terms, one constant and one time-dependent:

$$w_{DE}(z) = w_0 + w_a \frac{z}{1+z} \tag{1.3}$$

Precise measurements of w_0 and w_a can inform us about the effect of dark energy on our universe, and how that effect is changing over time. If $w_{DE} = -1$, dark energy can be modeled as a cosmological constant, with no time dependence.

For more thorough background and derivations, see the recent review of cosmology by Huterer & Shafer (2018).

Recent observations imply the current status of the universe to be flat, with Ω_r orders of magnitude smaller than Ω_M and Ω_{DE}. This results in a universe consisting almost entirely of matter and dark energy:

$$\Omega_M + \Omega_{DE} \approx 1 \tag{1.4}$$

Recent results from the Dark Energy Survey find $\Omega_M = 0.279^{+0.043}_{-0.022}$ and $w_{DE} = -0.80^{+0.20}_{-0.22}$ (DES Collaboration et al. (submitted)). As this analysis assumes a flat cosmology, constraints on Ω_M also imply constraints on Ω_{DE}.

1.2.1 Probes of Dark Energy

There are various methods in use today to measure these parameters and quantify the presence of dark energy in the cosmos. These include, but are not limited to:

- **Type Ia Supernovae (SNe)** result when white dwarfs in binary star systems accrete mass from their companions and approach the Chandrasekhar limit, the amount of mass necessary for a supernova to occur. The similar nature of Type Ia Sne progenitors across the universe makes them standard candles—they exhibit a predictable absolute luminosity, allowing theoretical predictions of observed luminosity, which is tied to the expansion of the universe. Comparing observed luminosities to those predicted by cosmological models led to the discovery of dark energy, and continues to constrain cosmological parameters today. See Howell (2011) for a review.

- **Baryon Acoustic Oscillations (BAO)** are relics of the decoupling of matter and radiation. Concentrations of primordial plasma, caught between gravity and radiation pressure, exhibit oscillatory behavior. At the time of decoupling, photons disperse, leaving behind shells of baryonic matter with known radius, and providing standard rulers for cosmology. Observing this radius at various distances is another modern probe of cosmic expansion. See Bassett & Hlozek (2009) for a review.

- The **Cosmic Microwave Background (CMB)** provides us with an image of the universe at the time of recombination, before the rise of dark energy. Oscillations of matter-radiation couplings—similar to BAO—have left imprints that can be observed today by measuring the distribution of hot and cold spots on the CMB. Due to the absence of dark energy at the time of recombination, this distribution can be characterized based solely on interactions between matter and radiation, giving us a second standard ruler. Dark energy influences the later universe, and thus affects the distance between us and the CMB. This in turn affects the angle that this standard ruler subtends on the sky, making the angular distribution of CMB anisotropies a powerful probe of cosmology. See Hu (2001) for a review.

- **Weak Gravitational Lensing** is the slight bending of light from background objects by the gravitational potential of foreground objects. This phenomenon manifests through distortions in both shapes of faraway galaxies and CMB anisotropies. As this effect depends entirely on mass, it provides powerful insight into the cosmic distribution of otherwise-invisible dark matter, allowing us to probe cosmological parameters by comparing observed rates of structure growth to those predicted by models. See Hoekstra & Jain (2008) for a review.
- **Galaxy Clusters** are massive objects whose growth is hampered by the presence of dark energy. We explore this cosmological probe further in the next section.

Each of these methods exhibits various strengths and weaknesses, constraining some cosmological parameters better than others. By combining the results from multiple probes, we can understand the presence and history of dark energy more precisely than with any one method. Figure 1.1 shows recent measurements of cosmological parameters through the combination of several probes. For overall reviews of modern observational cosmology, see Weinberg et al. (2013) and Huterer & Shafer (2018).

1.3 Galaxy Clusters

Galaxy clusters are the most massive gravitationally-bound objects in the universe, weighing in at $10^{13} - 10^{15}\mathrm{M}_{\odot}$ (mass of the Sun) of matter. Their large gravitational potentials cause them to accrete mass, growing over time. However, the presence of Dark Energy causes expansion, hindering this growth. This means that one of the most powerful methods of characterizing the evolution of the dark energy

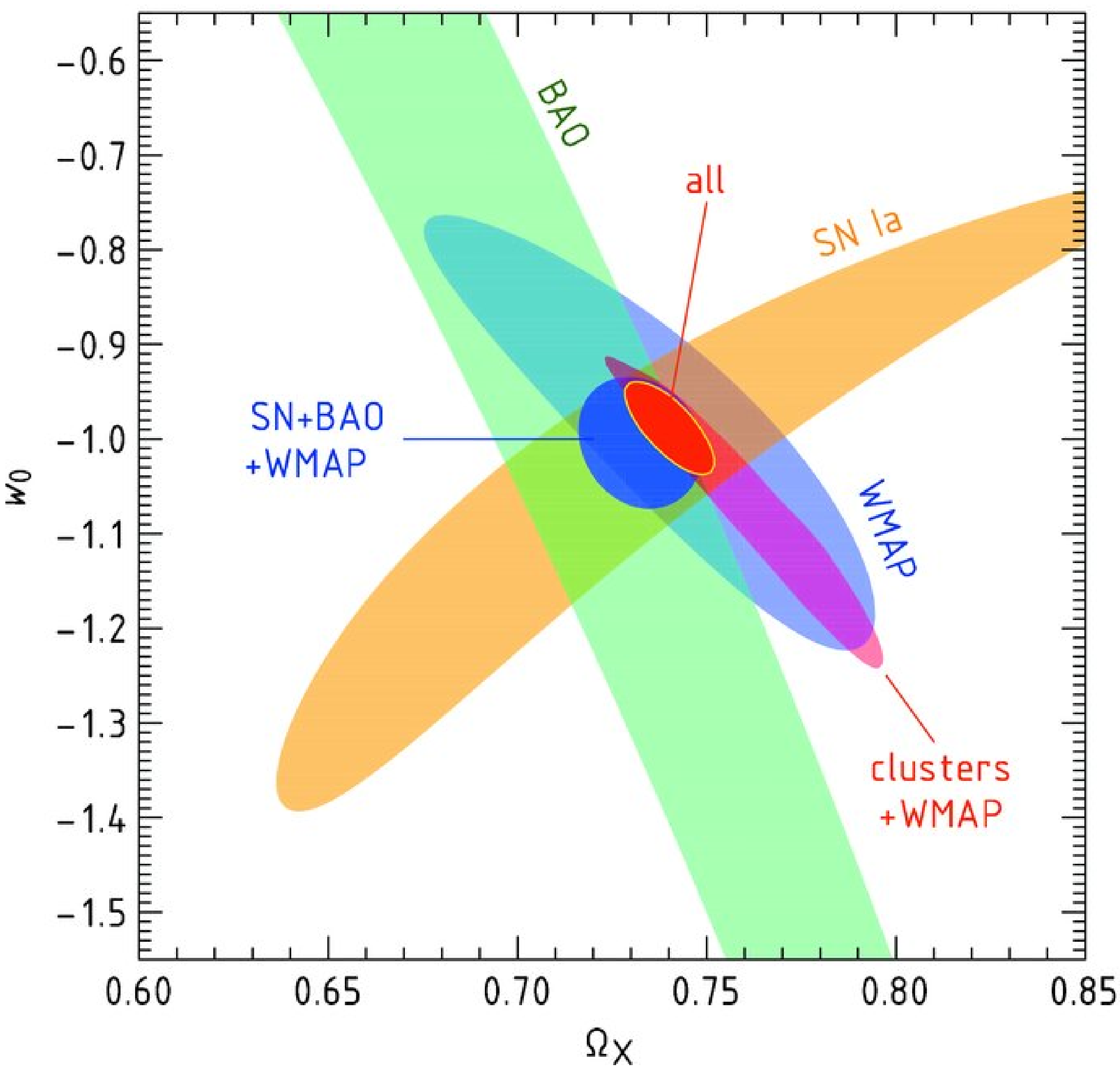

Figure 1.1 Recent constraints on cosmological parameters, combining various cosmic probes, from Vikhlinin et al. (2009b). Individual probes cannot constrain all parameters—for example, as seen above, BAO analysis is not informative about the value of w_0, and using SN Ia does not strongly constrain Ω_{DE} (marked as Ω_X in this figure). However, combining several methods leads to the much tighter constraints given by the red field marked "all."

equation of state, $w(z)$, is the study of how the number density of massive clusters varies over time. By comparing the observed abundances of galaxy clusters over a wide range of redshifts to simulations of the evolution of dark matter halos under varying cosmological models, we can extract $w(z)$ (see reviews in Weinberg et al. (2013) and Voit (2005)).

1.3.1 Anatomy of a Cluster

Galaxy clusters are made up of $\sim 90\%$ dark matter and $\sim 10\%$ baryons. A cluster, or collapsed dark matter halo, is defined as a sphere of radius r_x, where the matter density inside that radius is equal to x times the critical density of the universe at the cluster's redshift z, written $\rho_{crit}(z)$. The resulting mass within that radius is taken to be the cluster mass, M_x:

$$\begin{aligned} M_x &= \frac{4}{3}\pi r_x^3 \times x\rho_{crit}(z) \\ \rho_{crit}(z) &= \frac{3H^2(z)}{8\pi G} \end{aligned} \tag{1.5}$$

where $H^2(z)$ is the Hubble constant at the cluster's redshift, and G is the universal gravitational constant. The most commonly used measurements in cluster studies are M_{200} and M_{500}.

Most of a cluster's baryons exist in the form of ionized hydrogen and helium atoms, and make up the superheated gas permeating the halo, known as the intracluster medium (ICM). This gas can be observed through various methods, discussed in section 1.3.4, and is a gateway into learning more about the properties of clusters.

Only about a tenth of the baryonic matter rests in cluster galaxies. Cluster members include a set of elliptical and lenticular galaxies known as the red sequence. These old galaxies show a tight correlation between their colors and brightnesses, or magnitudes, and are instrumental in detecting clusters and measuring their properties such as redshift (Bower et al. (1992)). Figure 1.2 show the color-magnitude diagrams of several clusters' red sequences. Redder galaxies are brighter, with a lower magnitude. The extremely low scatter seen here is instrumental in identifying and characterizing these red sequences. The brightest of these galaxies are known as BCGs, or brightest cluster galaxies. They are often assumed to be at—and used as measures of—the centers of clusters.

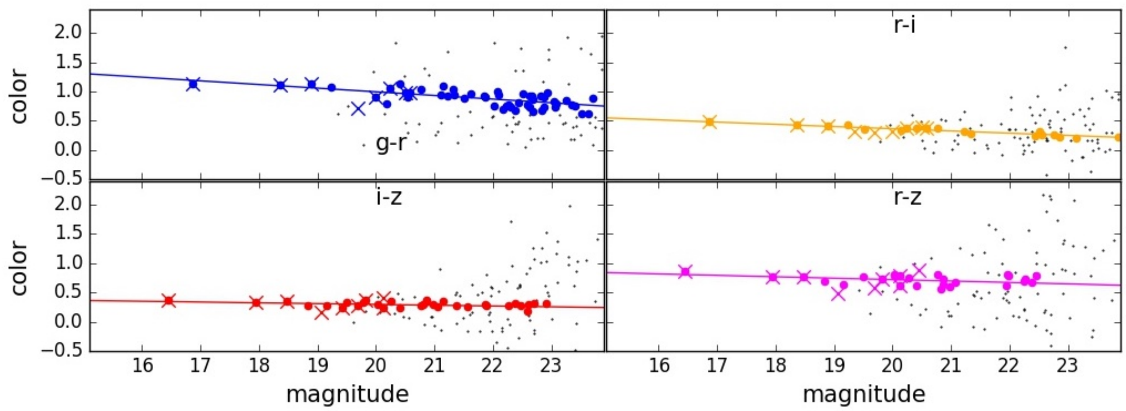

Figure 1.2 Color-magnitude diagrams of a cluster, through multiple filters. Includes all objects within a 3 arcmin × 3 arcmin cutout around the cluster center, with member galaxies marked in color. For member galaxies, lower magnitudes correlate with greater brightness, and color is defined as the difference in magnitudes of the object in images taken with different optical filters.

1.3.2 Cluster Cosmology

The cluster mass function, $N(M, z)$, measures the number density of galaxy clusters as a function of mass and redshift, and is the key to probing dark energy with galaxy clusters. We observe this mass function in the nearby recent (low-redshift) universe as well as the faraway old (high-redshift) universe, and compare the observed structure growth rate to those calculated from varying cosmological models. Figure 1.3, adapted from Vikhlinin et al. (2009b), shows an observed mass function compared with expected values using two different values of Ω_Λ. Note that the models not only cause the expected mass functions to shift, but also change the observed cluster abundances. This is because measuring cluster masses requires use of the distance-redshift relation, which is also affected by cosmological parameters. Figure 1.4, adapted from a review of observational cosmology by Huterer & Shafer (2018), shows the sensitivity of expected cluster counts to Ω_M and w_{DE}. Recent results in cluster cosmology from Vikhlinin et al. (2009b) are shown in Figure 1.5.

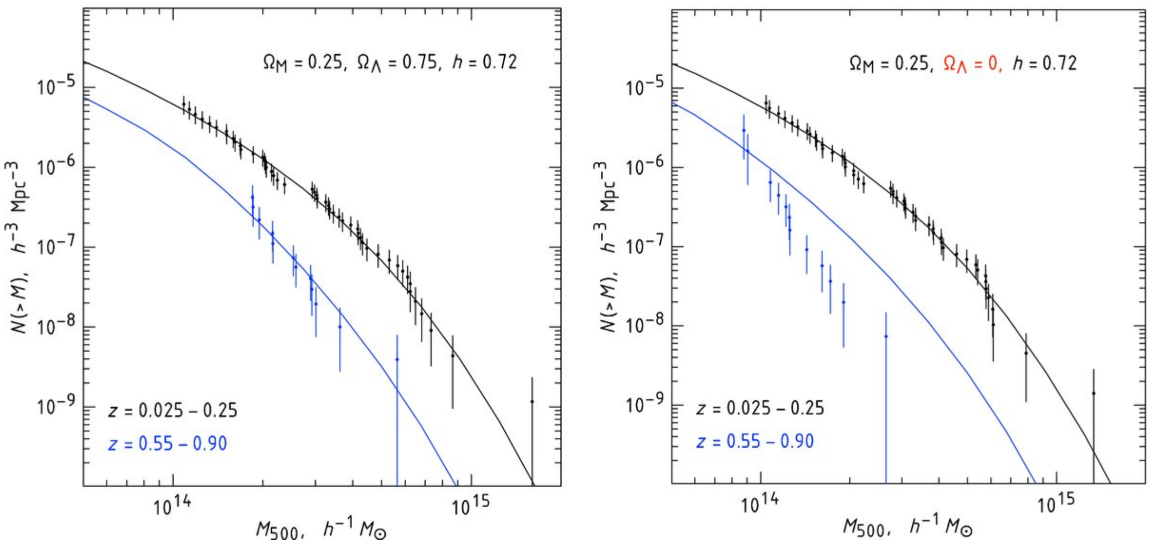

Figure 1.3 Observed mass function using data from the Chandra X-ray Telescope (data points and errors), overlaid with expected mass functions (solid lines) at different redshifts from two cosmological models. The modeled absence of dark energy (right panel) predicts a much higher cluster growth rate than the one observed. Figure credit Vikhlinin et al. (2009b).

In order to find the cluster mass function, $N(M, z)$, it is necessary to obtain precise measurements of cluster masses over a large range of redshifts and masses. This is complicated by the fact that $\sim 90\%$ of a cluster's mass is made up of dark matter, which does not interact with photons and thus cannot be detected using traditional electromagnetic telescopes.

1.3.3 Direct Measurements of Cluster Mass

There are several methods of directly measuring cluster mass, among them weak lensing, dynamical mass measurements, and X-ray hydrostatic measurements. Un-

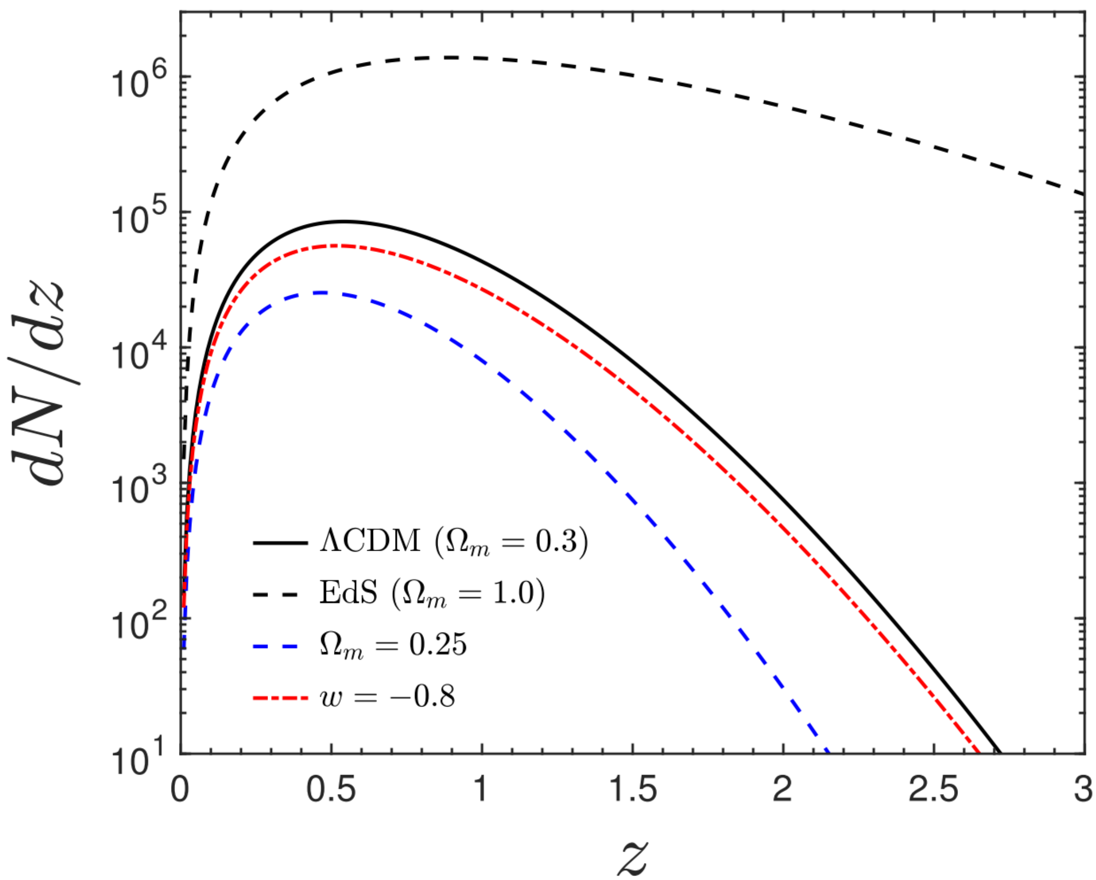

Figure 1.4 Sensitivity of cluster abundances over time to variations in Ω_M and w_{DE}. Comparing observed abundances to these expectations from a variety of cosmological models lets us constrain these parameters. Figure credit Huterer & Shafer (2018).

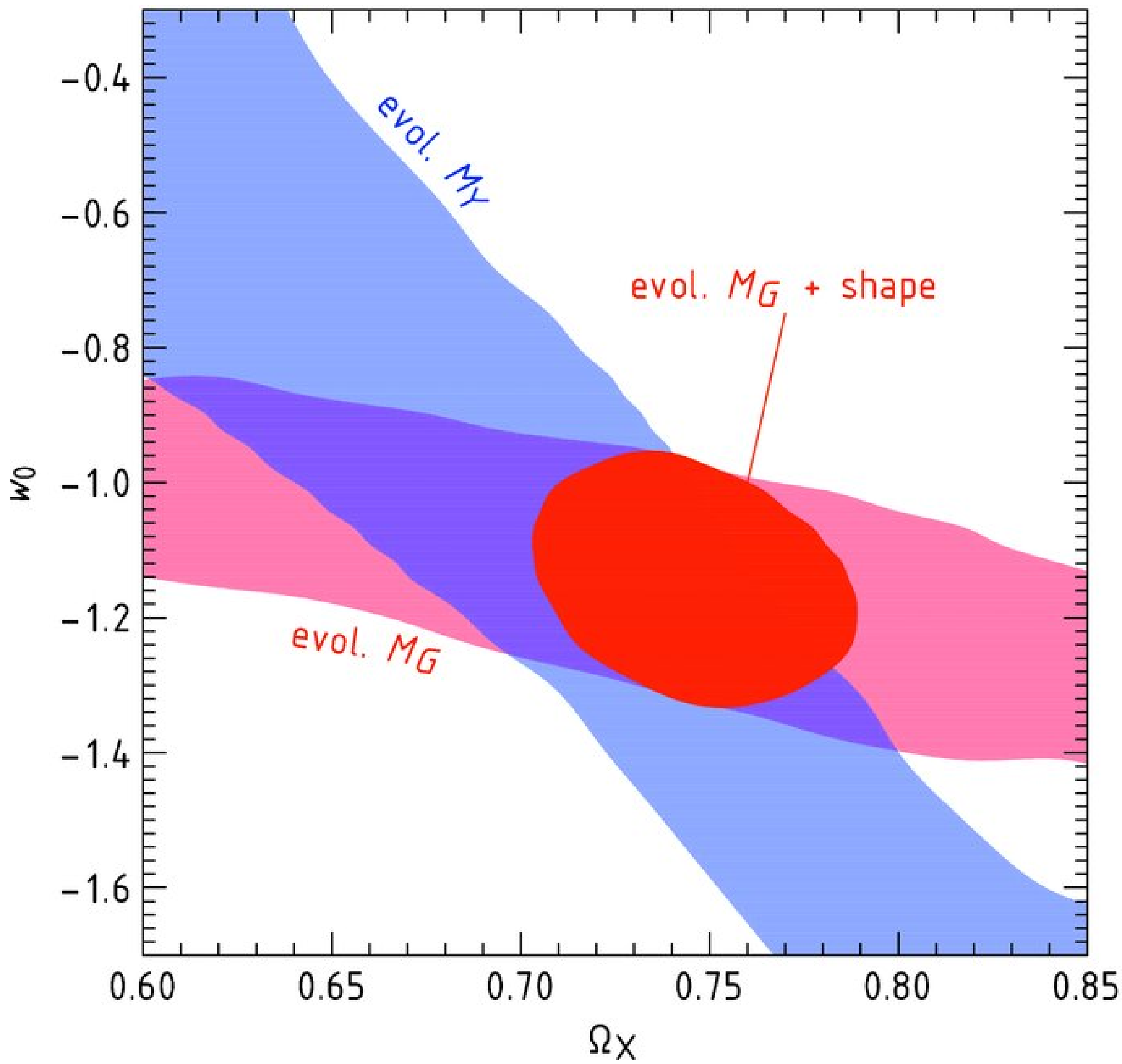

Figure 1.5 Constraints on cosmological parameters w_0 and Ω_{DE} (here named Ω_X) using two different methods of cluster mass measurement, by Vikhlinin et al. (2009b). Combining the evolution of the mass function with information about its shape gives tighter constraints, as seen by the red ellipse.

fortunately, these measurements are highly susceptible to systematic bias, making it difficult to simultaneously characterize both the data and the errors. Here, we review some of these methods and their challenges.

Weak Lensing Mass

As discussed in Section 1.2.1, lensing is the distortion of light traveling from faraway objects as it passes by strong gravitational fields on its way to our telescopes. Galaxy clusters provide such strong gravitational fields, and studying the light from galaxies behind clusters gives us a direct way of measuring cluster mass.

As noted in the name, weak lensing very faintly distorts observations from background galaxies. This distortion, known as shear, is too faint to be discernible by looking at images of clusters, but can be detected statistically with large ensembles of galaxies. Galaxies are intrinsically elliptical, and, in the absence of a lens, will be observed to be randomly oriented on the sky. Shear causes galaxies to seem to align around the central cluster, giving the ensemble a non-zero tangential component of ellipticity. Figure 1.6 shows an exaggerated visualization of this effect. Note that, as expected, the distortion is greatest near the cluster center, and fades as we move further away.

The amplitude of the lensing signal is directly affected by the strength of the gravitational potential causing the distortion. By measuring this shear in the shapes of the background galaxies, we can calculate the amount of mass necessary in the foreground to create the signal observed.

While this seems simple enough in theory, cluster weak lensing is riddled with the same challenges as using lensing as a cosmological probe in its own right. First and foremost, galaxy shapes are notoriously hard to measure. Uncontrollable factors such as humidity and wind cause their own distortions to light as it travels through

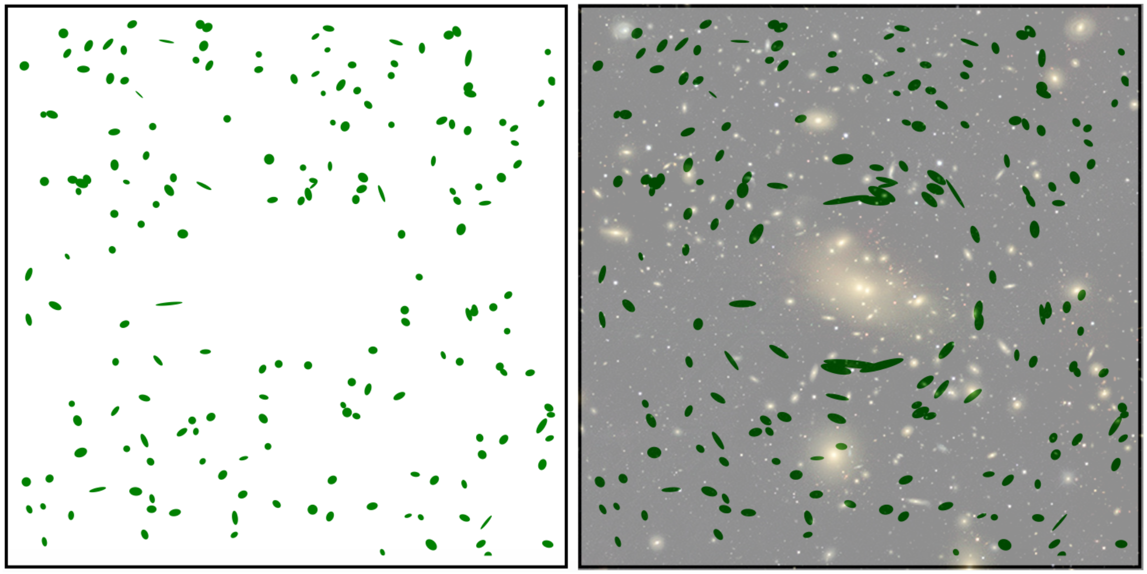

Figure 1.6 The (exaggerated) weak lensing effect of a lens on observations of a field of background galaxies. On the left are the galaxies without a lens, randomly oriented across the sky. On the right we add a cluster and the resulting shear. Image modified from Wikipedia.

the Earth's atmosphere, skewing and possibly reversing the effects of shear. While trying to measure shear around a particular cluster, nearby structure, such as another cluster close to the line of sight, can further distort the images of background galaxies in unexpected ways. Because the signal is weak, we also require observations of a great number of background galaxies, which usually requires detection of very faint and faraway objects.

More details and mathematical background on this topic follow in Section 3.1. For a review on cluster weak lensing, see Hoekstra et al. (2013).

X-ray Hydrostatic Mass

This method of mass measurement assumes clusters are in hydrostatic equilibrium—at any radius within a cluster, the pressure of the intracluster gas balances out the inward gravitational pull, giving the cluster a stable structure:

$$\frac{dP_g}{dr} = \frac{-GM(r)\rho_g}{r^2} \tag{1.6}$$

Here, P_g and ρ_g are the gas pressure and density, respectively, G is the universal gravitational constant, and $M(r)$ is the mass of a cluster contained within radius r. By measuring the temperature and density of the intracluster gas (through X-ray observations, as described in 1.3.4) and expressing the gas pressure in terms of these quantities, we can calculate the mass necessary to achieve this equilibrium:

$$M(r) = -\frac{k_b T_g}{\mu m_p G}\left(\frac{d(\ln \rho_g(r))}{d(\ln r)} + \frac{d(\ln T_g)}{d(\ln r)}\right) r \tag{1.7}$$

where k_b is Boltzmann's constant, μm_p is the mean mass of the gas particles, and T_g is the gas temperature. See Section 5.5 of Sarazin (1988) for a review on hydrostatic masses.

Unfortunately, this method is complicated by the possibility of clusters not exhibiting hydrostatic equilibrium - for example, merging clusters and clusters accreting mass experience far more agitated gas flows. Cooling of the gas at cluster cores can also cause disturbances to this equilibrium. In fact, existing measurements of the mass-temperature scaling relation, using both hydrostatic and other types of mass measurements, indicate that hydrostatic masses may be biased low, especially in the low-mass regime (Kettula et al. (2013), Mahdavi et al. (2013)). We explore the possibility of this further in Chapter IV.

Dynamical Mass

Dynamical mass measurements also capitalize on a cluster's gravitational potential. Instead of looking behind clusters, they make use of observations of the velocity dispersions of cluster member galaxies. Assuming galaxies in a cluster are bound to each other through gravity, otions of member galaxies are directly related to the strength of the gravitational potential - in the most simplified model, a greater mass will cause higher galaxy orbital velocities. This fundamental concept is tempered by complications such as unrelaxed clusters, mergers, infalling mass, etc.

This dissertation is based on weak lensing mass measurements, and explores questions related to hydrostatic masses. However, we do not explore dynamical masses further in this work. For further details and a comparison of dynamical mass measurement methods, see Old et al. (2014) and Old et al. (2015).

1.3.4 Cluster Finding and Mass Proxies

Clusters can be detected through a number of electromagnetic methods, spanning the optical, microwave, and X-ray wavelengths. Observables from these methods can serve as proxies for cluster mass (Weinberg et al. (2013)). These observables are relatively easier to measure than direct cluster masses, making them ideal candidates for conducting large-scale mass measurements.

The use of these proxies is limited by the precision to which we understand the mass-observable scaling relationship, $p(O|M, z)$. Constraining this relation requires a set of clusters for which both observations of the proxy and reliable direct mass measurements are independently available.

Optical and Near-Infrared Observations of Clusters

Optical and near-infrared surveys find clusters by searching for bunches of galaxies of similar redshifts that are spatially close to each other. For example, the redMaPPer algorithm finds clusters by searching for red sequences in galaxy catalogs (Rykoff et al. (2014)). redMaPPer also measures the most common optical observable of a cluster - the count of its galaxies, known as its richness. Though only $\sim 1\%$ of a cluster's mass resides in its galaxies, richness grows with cluster mass, and serves as a relatively easily-measurable proxy. A second observable matches a cluster's mass to the combined stellar mass of its members, $\mu_{\star}$. Figure 1.7a shows recent constraints on the richness-mass relation from the Dark Energy Survey collaboration (Melchior et al. (2017)), and Figure 1.7b shows a scaling relation between stellar mass and cluster mass using data from the Sloan Digital Sky Survey (Pereira et al. (2017)).

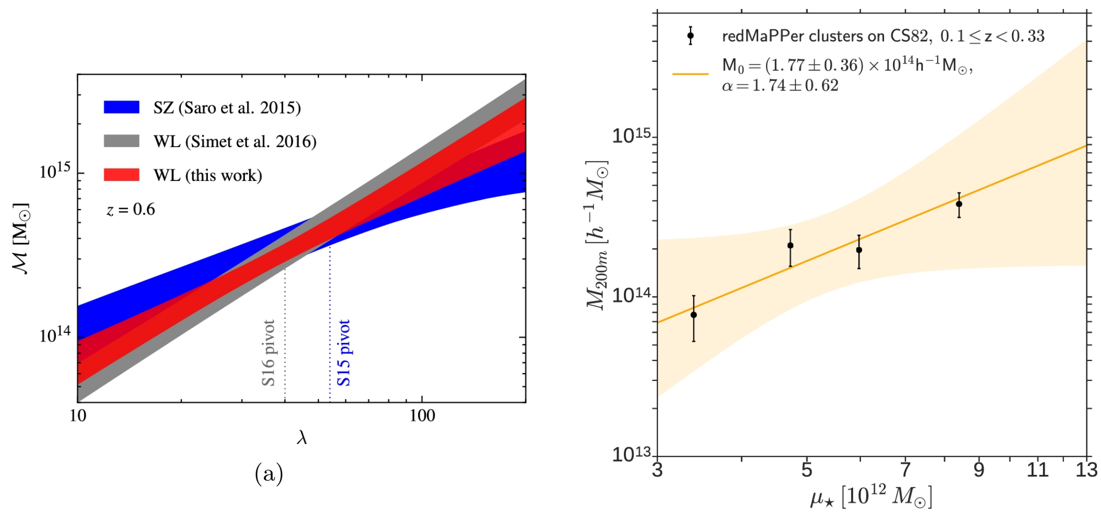

(a) (b)

Figure 1.7 Scaling relations between optical observables and cluster mass. (a) Comparison of recent scaling relations between cluster richness and mass, showing $1-\sigma$ intervals. Figure taken from (Melchior et al. 2017) - labeled "this work" - presenting results from the Dark Energy Survey's Science Verification data. (b) Scaling relation between total stellar mass and cluster mass, showing a $2-\sigma$ interval. Figure taken from (Pereira et al. 2017) presenting results from the Sloan Digital Sky Survey's Stripe 82 data.

CMB Observations of Clusters

The cosmic microwave background (CMB) provides us with another way of detecting and characterizing clusters. Radiation from the CMB passing through a cluster is inverse-Compton scattered by the intra-cluster medium (ICM) in a process known as the Sunyaev-Zel'dovich effect (Sunyaev & Zeldovich (1972)). Measuring these aberrations in the CMB not only help us detect clusters, but also provide us with an observable which scales with cluster mass. Recent scaling relations between mass and the strength of the SZ signal have been derived using CMB data from Planck (Ade et al. (2011)) and the South Pole Telescope (SPT) (Stern et al. (submitted)), and are shown in Figure 1.8.

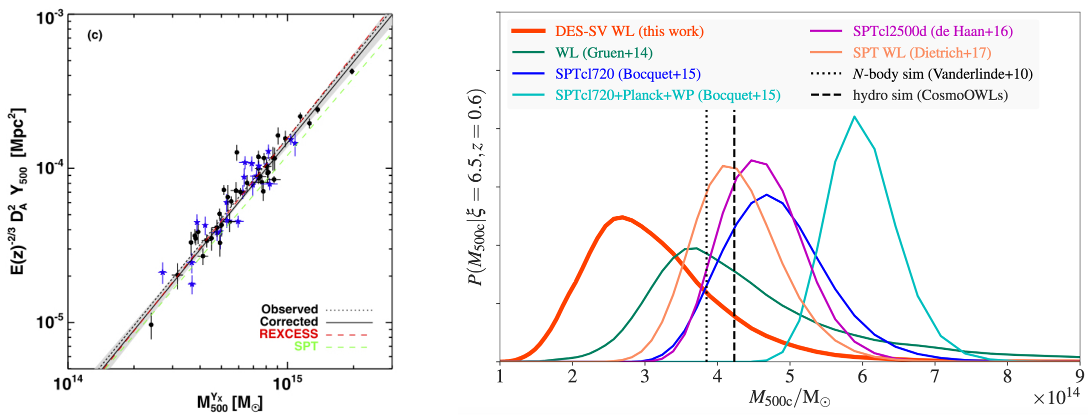

(a) (b)

Figure 1.8 Scaling relations between CMB observables and cluster mass. (a) Scaling relation between SZ observable and cluster mass, showing results using Planck data with a 1σ interval, and comparing to previous works. Figure taken from (Ade et al. (2011)). (b) Comparison of recent works on the SZ observable and mass, showing mass probability distributions for a single SZ cluster using various recent scaling relations. Figure taken from (Stern et al. (submitted))—denoted by the red curve and labeled “this work”—presenting results from the Dark Energy Survey's Science Verification data.

X-ray Observations of Clusters

The superheated gas of the intracluster medium emits bremsstrahlung radiation in the X-ray spectrum. This allows the detection of galaxy clusters by searching for extended sources in data from X-ray telescopes. The extended, or spread-out, nature of the ICM helps discern clusters from other strong X-ray sources, such as active galactic nuclei. Spectral data of clusters in the X-ray range provides information about the energy of the observed radiation, and allows measurement of the temperature of the ICM. This temperature, as well as the cluster luminosity - a measure of the strength of the X-ray radiation - can be used as proxies for cluster mass. The brightness of the radiation over the extended area also allows calculation of the cluster gas mass, which when multiplied with temperature gives the thermal energy of the ICM, a quantity that has been observed to scale with cluster mass with relatively low scatter. Figure 1.9 shows a few recent scaling relations between cluster mass and X-ray observables.

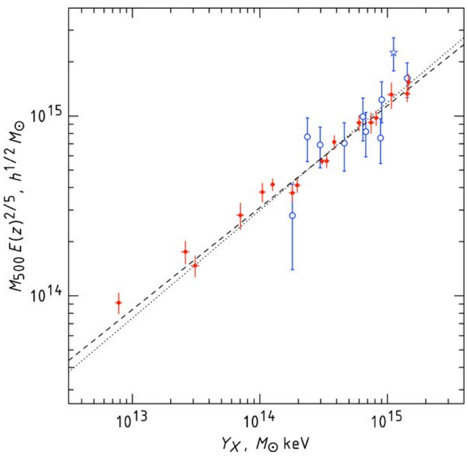

(a)

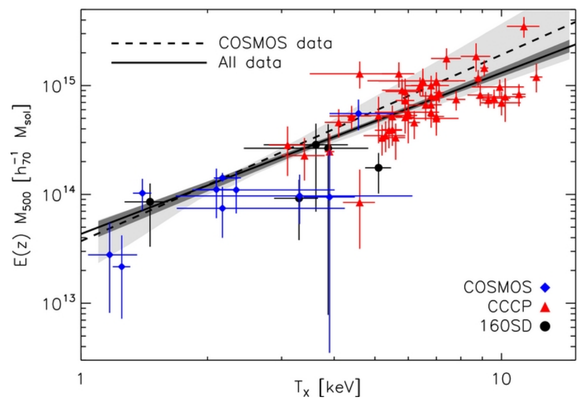

(b)

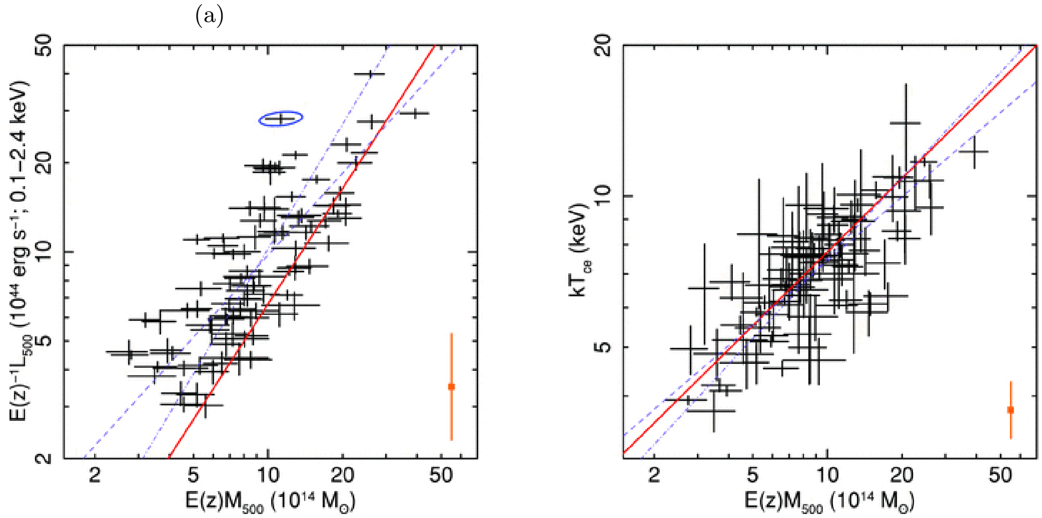

(c)

Figure 1.9 Scaling relations between X-ray observables and cluster mass. (a) Scaling relation between thermal energy of ICM and cluster mass, showing results using Chandra data (Vikhlinin et al. (2009a)). (b) Scaling relation between cluster temperature and mass, using Chandra and XMM data (Kettula et al. (2013). (c) Scaling relations between cluster mass and luminosity (left) and temperature (right), using data from Chandra and ROSAT (Mantz et al. (2010)).

The extended X-ray data is also used to measure each cluster's X-ray barycenter. The X-ray emission is a direct indicator of the presence of the intracluster medium—barring any interference from extraneous point sources such as active galactic nuclei, which are subtracted from the signal—and the ICM is assumed to trace the dark matter distribution, making this an ideal measure of the cluster center for lensing studies.

See Sarazin (1988) for a review of the X-ray properties of clusters.

1.4 The Dark Energy Survey (DES)

Modern observational cosmology capitalizes on large-scale surveys—explorations of gargantuan swathes of the night sky, aiming to gather information on as-yet undiscovered cosmic objects. These surveys provide the large statistical datasets necessary for most probes of cosmology.

The Dark Energy Survey (DES) is a multi-band optical survey of an eighth of the sky, aiming to constrain $w(z)$ through the use of several probes, including the study of the evolution of galaxy clusters over time. The survey consists of two parts - wide field imaging of 5000 sq. deg. in the $grizY$ bands, and recurring deep field imaging of 30 sq. deg. in the $griz$ bands, both through the Dark Energy Camera (DECam) (Flaugher et al. (2015)) mounted on the 4m Blanco telescope at the Cerro Tololo Inter-American Obseratory in Chile. Over the course of this extensive survey, DES expects to find $\sim 100,000$ galaxy clusters and ~ 300 million galaxies. Objects as dim as the 24th magnitude and as far away as $z6$ have been observed and analyzed, with more to be found as the survey progresses. This unique data set provides us with a sufficient statistical sample and large enough redshift range for a cluster-WL analysis that is significantly improved over previous surveys (such as the Sloan Digital Sky

Survey, where the limiting magnitude is ~ 22[1]).

The data used in this work is from the DES Science Verification (SV) run, a four-month testing period that followed first light in 2012. As this was a testing run, it brought about many improvements to the instrumentation, honing it for subsequent runs. As such, data from this run is of a lower quality than can be expected of the entire survey. However, in this work, we show that even SV data is sufficient to place meaningful constraints on the cluster $M - T_x$ scaling relation.

Data from the SV run is distilled into the DES SVA1-Gold catalog, a list of observed sources passing numerous quality cuts. All objects were observed at least once in each of the $griz$ bands, with the possibility of multiple measurements in each band. The individual measurements are combined to determine positions and magnitudes, among other properties. Further details, including calibrations and quality cuts, can be found in the documentation for the official DES-SVA1 data release[2].

1.4.1 Star-Galaxy Separation

Lensing studies only use galaxies—stars are, of course, in the foreground of any object of interest. The SVA1-Gold catalog sorts objects using the DES-developed "Modest Star-Galaxy Separation," which finds galaxies by looking at how point-like objects are, through the use of the SPREAD_MODEL output from object-finder Source Extractor. This estimator catches $\gtrsim 98\%$ of galaxies, with a false contamination rate $\lesssim 3\%$. Further details can be found in the DES-SVA1 data release documentation[2].

[1] http://www.sdss.org/dr13/scope/
[2] https://des.ncsa.illinois.edu/releases/sva1

1.4.2 Photometric Redshifts

Object redshifts, from which we infer object distances, are imperative to lensing studies—they let us measure of how far behind a cluster a source is observed. However, galaxy spectra take great amounts of telescope time to observe—for example, the Dark Energy Spectroscopic Instrument (DESI), currently being built and expected to provide at least an order of magnitude increase in the number of observed galaxies over current surveys, will only measure spectra from $\sim$ 30 million galaxies over five years[3], an order of magnitude less than DES's expected galaxy count over the same time period. This makes it unrealistic to attempt to measure true spectroscopic redshifts for the entire DES ensemble of galaxies.

Instead, photometric redshift (photo-z) measurements are found through the use of several independent machine-learning pipelines. These algorithms estimate the probability density function $p(z)$ of the redshift of an object, using its magnitudes through various filters, calibrating their estimates on results from a representative subsample of galaxies for which both photometric and spectroscopic redshifts are available (Sánchez et al. (2014)). This work primarily uses mean photo-z measurements from the DES TPZ pipeline, with some use of the DESDM Neural Network results for testing purposes.

1.5 The DES-SV-XCS Cluster Sample

The clusters used in this dissertation are detected by the XMM-Newton Cluster Survey (XCS) (Lloyd-Davies et al. (2011), Mehrtens et al. (2012), Viana et al. (2013)) and followed-up by DES. Optical data from DES SV confirm the X-ray detections and provide photometric data for measurement of cluster redshifts, which are then

[3]See DESI final design report: http://desi.lbl.gov/tdr/

combined with XCS data to measure X-ray temperatures for each cluster.

The XMM-Newton Cluster Survey (XCS) conducts a serendipitous search of archival XMM-Newton data for galaxy clusters and groups, looking for extended X-ray sources using the XAPA pipeline Manolopoulou et al. (in prep.). Once detected, candidates are confirmed through visual follow-up using data from overlapping optical surveys—in our case, DES. During this follow-up, we remove false detections and clusters that have been detected twice (with different centers). We also mark clusters which have been mis-centered, possibly due to the presence of point X-ray sources that were missed by the automatic pipeline. This last set is then rerun through the pipeline to obtain better measurements of the center.

Once clusters are confirmed, the next step is to assemble redshifts. Spectroscopic redshifts are used where available from previous literature. For the rest, photometric redshifts are measured using multi-band DES data to examine the cluster red sequences, as described in Appendix B of Das et al. (in prep.).

1.5.1 Cluster X-Ray Temperatures

Cluster temperatures, T_x, are measured from X-ray spectra, as described in Section 1.3.4. XCS measures both core-excised and non-core-excised temperatures for each cluster. The non-core-excised temperature makes use of spectra from an elliptical aperture with semi-major axis equal to each cluster's R_{500}, centered on the cluster detection region. For more details on aperture selection and T_x measurements, see Manolopoulou et al. (in prep.).

Core-excised temperatures were measured using the same apertures as above, but with a central area of radius $0.15R_{500}$ removed. In order to avoid biased temperature measurements due to cool cluster cores, we use these T_x values through most of this work.

1.6 DES Simulated Sample

To validate the analysis presented in this work, we test our pipeline on data from the Buzzard v1.1 simulations. Buzzard covers 10313 sq. deg. and contains 971 million galaxies "observed" in the DES filter bands, and out to DES depth. The simulation provides a halo catalog, from which we choose halos to match our cluster sample. For each cluster in the DES-XCS sample, we choose a halo of similar mass and redshift, creating our simulated halo sample (for more details, see section 3.7.1). The galaxy catalog provides redshifts, magnitudes, and positions, comparable to the DES object catalog, and shears for each object are measured using ray-tracing. For further details, see DeRose et al. (in prep.) and Wechsler et al. (in prep.).

CHAPTER II

Galaxy Shape Measurements

Weak gravitational lensing is the most direct method of measuring masses of galaxy clusters, and is the method used throughout this work. It is also one of the most difficult methods, due to the intricacies of measuring galaxy shapes, which form the backbone of weak lensing measurements. Measuring shapes requires extremely high-resolution data - multiple pixels on the image for each faraway galaxy - and is complicated by the fact that light passing through our atmosphere is refracted by environmental factors such as wind and water vapor, distorting images of objects by the time they reach the telescope. Adding in the fact that weak lensing is only measurable as an averaged effect over an ensemble of hundreds to thousands of galaxies, we also require large amounts of data and computing time in order to make meaningful measurements.

This work uses galaxy shapes from the Dark Energy Survey Science Verification (DES-SV) data. The official DES-SV shape catalog contains measurements spanning a 139 sq. deg. patch of sky. However, the DES-SV observations cover an additional ~ 110 sq. deg. of sky, for which photometric and astrometric object data is available. As a majority of the clusters in our sample lie in these extra regions, we run the DES-SV shape measurement pipeline on areas of sky surrounding these clusters, test our results, and present them for public use. In this effort, we make available shapes for an additional 590,000 galaxies, $\sim 27\%$ the size of the official DES-SV release.

This chapter presents the galaxy shape catalogs used throughout this work. We briefly describe the DES-SV shape measurement pipeline in Section 2.1. In Section 2.2, we present the data from our additional runs of the pipeline, including various quality checks. Section 2.2.2 details how to access this data. Related to this chapter, Appendix B provides a short set of instructions on how to run the shape measurement pipeline.

2.1 Galaxy Shapes from the Dark Energy Survey

The DES-SV shape measurement pipeline and associated data products are documented by Jarvis et al. (2016) in the DES-SV Weak Lensing Shear Catalogues paper, from which we present some pertinent details below. This pipeline takes data from the SVA1-Gold catalog and processes it through several steps:

1. MEDS file creation: Multi-Epoch Data Structures (MEDS) are created to collate all available relevant information for a given object into one easily-accessible file, using the MEDS[1] and DESWL_SHAPELETS[2] libraries. Each MEDS file organizes data for all observations of all objects in a given DES tile. For each object, the file includes cutout images of all instances of observation in all filters, after initial calibrations (sky-background subtraction, magnitude calibration, etc.). It also includes segmentation and weight maps from Source Extractor (SExtractor), the program used to identify objects in DES images. These maps contain pixel-by-pixel information about image detection and quality (for further details about SExtractor outputs, see Bertin & Arnouts (1996) and

[1]https://github.com/esheldon/meds
[2]https://github.com/rmjarvis/deswl_shapelets

additional documentation[3]). Finally, MEDS files flag any observations whose quality is compromised, such as images that have airplanes flying through. For further details on the creation and use of MEDS files, see Section 5 and Appendix A of Jarvis et al. (2016).

2. PSF measurement and inclusion: The point-spread-function (PSF) informs how much an object's shape is distorted due to atmospheric (and sometimes instrumental) effects. By examining stars - which should ideally look like points - in a given image, we can calculate and reverse this effect on other nearby objects. This step calculates the estimated PSF at the position of each galaxy for each observation of that galaxy, and creates a list of images whose PSFs are too large to pass data quality checks (PSF blacklist). To do this, the PSF is first measured at the positions of stars in the CCD where the galaxy is observed, using the PSF EXTRACTOR (PSFEX) package (Bertin (2011)). These individual measurements are then interpolated to measure the PSF at any other location on the CCD. For further details, see Section 4 of Jarvis et al. (2016).

3. Shape measurement pipeline: DES uses two different shape measurement pipelines, IM3SHAPE and NGMIX, which work with the outputs of the previous steps. Further details on both pipelines can be found in Section 7 of Jarvis et al. (2016). In this work, we use results from the IM3SHAPE pipeline, as it covers a larger section of sky than NGMIX (and thus includes more of our clusters). We describe this pipeline further in the following section.

[3]https://www.astromatic.net/software/sextractor

2.1.1 Im3shape

A galaxy's observed shape and orientation can be quantified by two components of ellipticity, e_1 and e_2:

$$e = e_1 + ie_2 = |e| \exp(2i\phi) \tag{2.1}$$

where ϕ represents the galaxy's orientation angle. The ellipticities used in this work are measured from optical DES r-band data using the Im3shape v9 shape measurement pipeline, described in depth in Section 7.3 of Jarvis et al. (2016). This pipeline fits both a bulge and disc model to each galaxy, retaining the result with greater likelihood, and translates the fit into e_1 and e_2 values. It also provides a weight for each galaxy, based on both shape noise and the measurement uncertainty for that particular galaxy (details in section 7.3.4 of Jarvis et al. (2016)).

As Im3shape is a maximum-likelihood model-fitting program, its estimated ellipticities are affected by noise bias. To correct for this, as well as small selection effects and a low model bias, the pipeline includes a noise bias correction (NBC), providing multiplicative and additive correctors for each galaxy. The multiplicative term, m, is applied collectively to an ensemble of ellipticities, while the additive terms, c_1 and c_2, are applied individually to each galaxy's e_1 and e_2, respectively (see Section 3.1.3 for details on applying these corrections). These correctors are measured using simulated data from the GreatDES suite, which matches well with DES data quality (see Section 2.2.1 for details).

To ensure unbiased scientific results, Im3shape ellipticities are blinded. Each e_1 and e_2 is multiplied by an unknown α between .9 and 1, preventing us from subconsciously skewing our analysis to match results from previous literature. Only after all analysis methods and corrections are finalized is the data unblinded, keeping final results free from experimenter's bias.

Further details on Im3shape and corrections can be found in the DES SV Weak Lensing Shear Catalogues paper (Jarvis et al. (2016)). We also outline the steps necessary to measure shapes using Im3shape in Section ??)

Im3shape Data Quality Cuts

Once shapes have been measured, they undergo several quality cuts, based on runs of Im3shape on simulations, to weed out unreliable results. These include the following conditions, where each parameter below is an output of the pipeline:

- ERROR_FLAG == 0: ensures that the pipeline ran and converged properly; weeds out objects that are too large or faint
- INFO_FLAG == 0: more conservative - removes objects that are: too small; flagged by the object detection software SExtractor; in parts of the sky for which we cannot measure photometry properly; etc.
- $(S/N)_w > 15$: removes objects with low signal-to-noise ratio (SNR); $(S/N)_w$ measures a galaxy's SNR by taking a weighted average of the SNR values of all pixels in the galaxy (see Section 7.2 of Jarvis et al. (2016) for details)
- $R_{gp}/R_p > 1.2$: removes objects that are not sufficiently well-defined beyond the PSF (R_{gp} is the size of the object convolved with the PSF, while R_p is the PSF size)

2.2 Shapes for the DES-SV-XCS Cluster Sample

The official DES-SV Im3shape catalog contains shear measurements spanning a 139 sq. deg. patch of sky known as the SPT-E region (Jarvis et al. (2016)). However, the DES-SV observations cover an additional $\sim$ 110 sq. deg. of sky, and the official object catalog—DES-SVA1 gold[4]—provides vetted astrometric and photometric data in these extra regions. These extra regions contain 104 of the 133 clusters in our sample (see Figure 2.1). In order to use as many clusters as possible, we run the IM3SHAPE and noise bias calibration pipelines on 80arcmin x 80arcmin areas of sky surrounding these clusters.

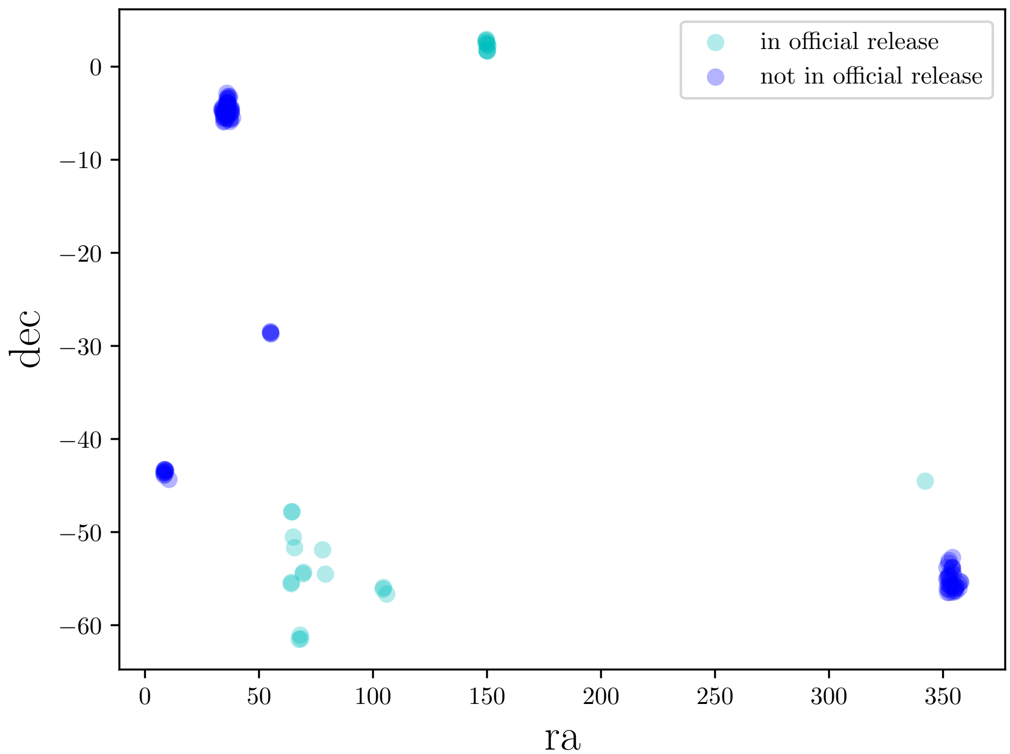

Figure 2.1 Positions of clusters in our sample. Cyan shows clusters for which shape measurements are available through the official DES-SV IM3SHAPE catalog. Blue shows clusters for which we run the pipeline ourselves.

In this effort, we generate shapes for approximately 590,000 galaxies in the DES-SV sky outside the SPT-E region, adding to the 2.12 million galaxies in the official catalog. These shape measurements were run before the cluster list was finalized—thus, these additional catalogs include areas around clusters in our final sample, as

[4]https://des.ncsa.illinois.edu/releases/sva1

well as areas of sky containing potential clusters that were later dropped.

2.2.1 Validating Additional Catalogs

As mentioned in Section 2.1.1, noise bias corrections and shape quality cuts depend on the physical properties of the ensemble of objects to be calibrated. The corrections and cuts for the official catalog were calculated using the Great-DES simulation suite, and multiple tests were conducted to ensure that the simulations were an accurate representation of the dataset (Jarvis et al. (2016)). In order to use the same cuts and NBC calcuations for our measurements, we must show that the additional regions of sky are comparable to the regions in the official catalog, making them also representable by Great-DES. For reference, the tests between the DES official catalog and Great-DES are shown in Figure 2.2 and listed here:

- the ensemble's distribution of the magnitude of ellipticity, $|e| = \sqrt{e_1^2 + e_2^2}$ (top left panel)
- the ensemble's distribution of R_{gp}/R_p, defined in Section 2.1.1 (top middle panel)
- the ensemble's distribution of $(S/N)_w$ (signal-to-noise ratios), defined in Section 2.1.1 (top right panel)
- comparison of galaxy sizes to signal-to-noise ratios (bottom left panel)
- comparison of R_{gp}/R_p values to signal-to-noise ratios (bottom middle panel)
- bulge fraction: portion of the ensemble for which the bulge model is deemed to fit best, as varies with signal-to-noise ratio (bottom right panel)

NBC measurements particularly depend on the distribution of an ensemble's $|e|$, and on the relationship between object size and $(S/N)_w$ (the two leftmost panels in Figure 2.2). Figure 2.3 shows these properties for both the official catalog and the ensemble of additional areas. We find that these properties are similar for both sets, allowing us to use the same noise bias calibration for the extra regions of sky.

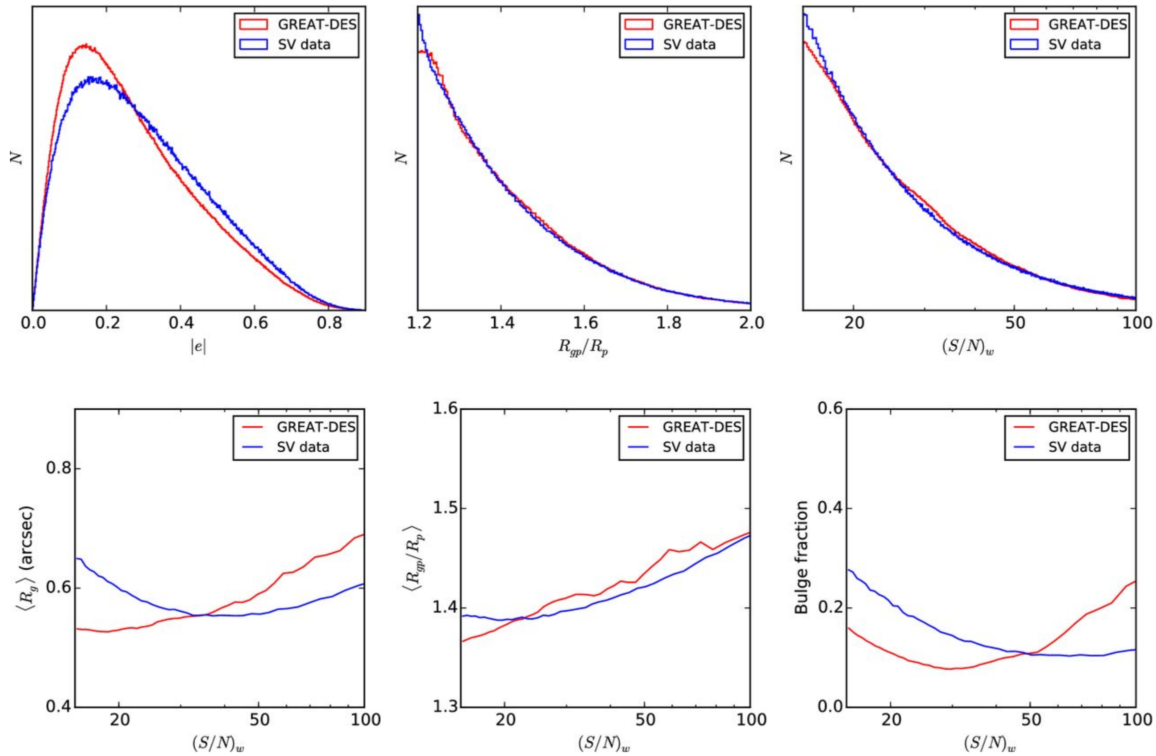

Figure 2.2 Comparison of official DES-SV Im3shape catalog to Great-DES simulations, from Jarvis et al. (2016). See bulleted list in Section 2.2.1 for details about each panel.

To further ensure catalog quality, we follow Jarvis et al. (2016) and run all the other comparisons shown in Figure 2.2. Our results, shown in Figure 2.4, assure us that the additional regions of sky are comparable to the regions in the official release, and thus also comparable to Great-DES. We conclude that both the quality cuts and the noise bias calibrations for the official catalogs are applicable to our entire sample.

2.2.2 Accessing Additional Catalogs

The official DES-SV shape catalog has already been released to the public (see details in Jarvis et al. (2016)). In the interests of promoting open science and research

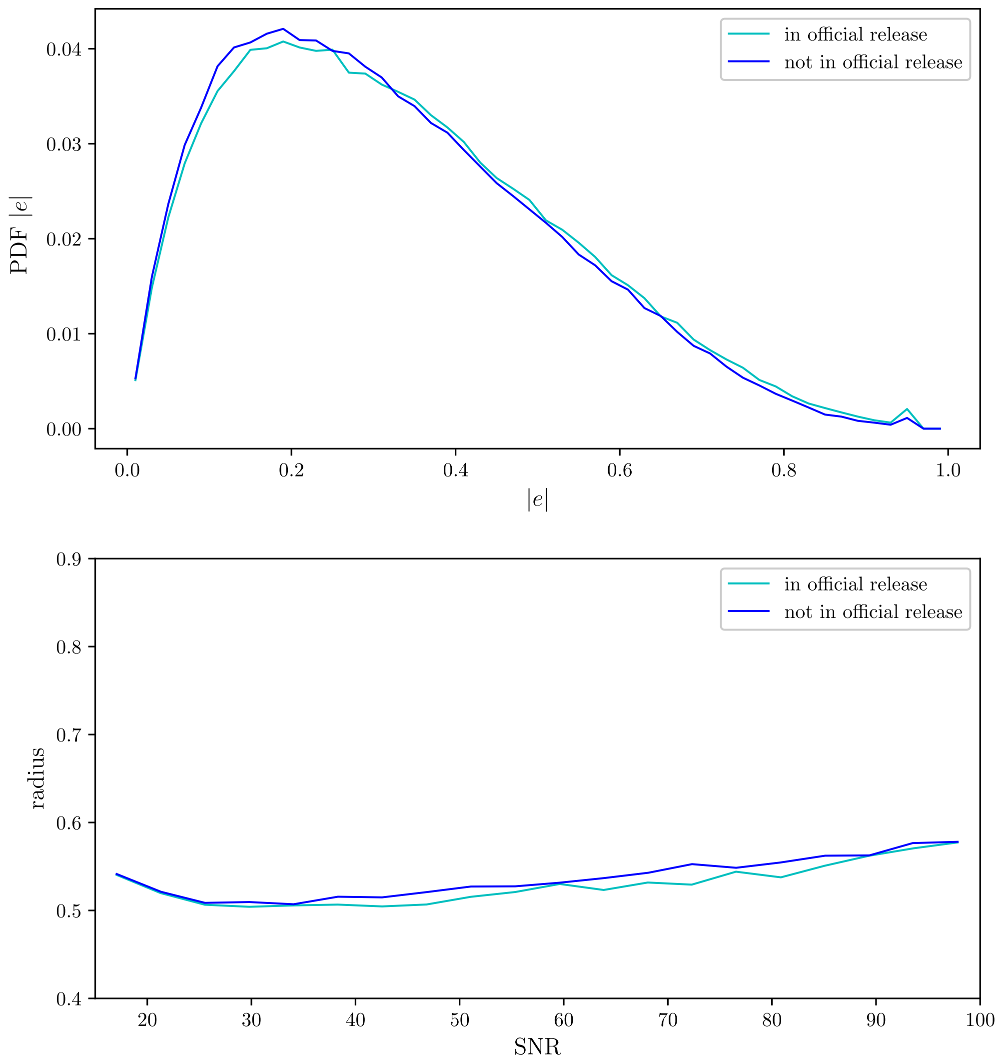

Figure 2.3 Comparison of official DES-SV IM3SHAPE catalog to runs of IM3SHAPE on additional areas of sky. Top shows histograms of $|e|$, and bottom shows the dependence of object size on signal-to-noise ratio, denoted $(S/N)_w$. See bulleted list in Section 2.2.1 for definitions of each quantity.

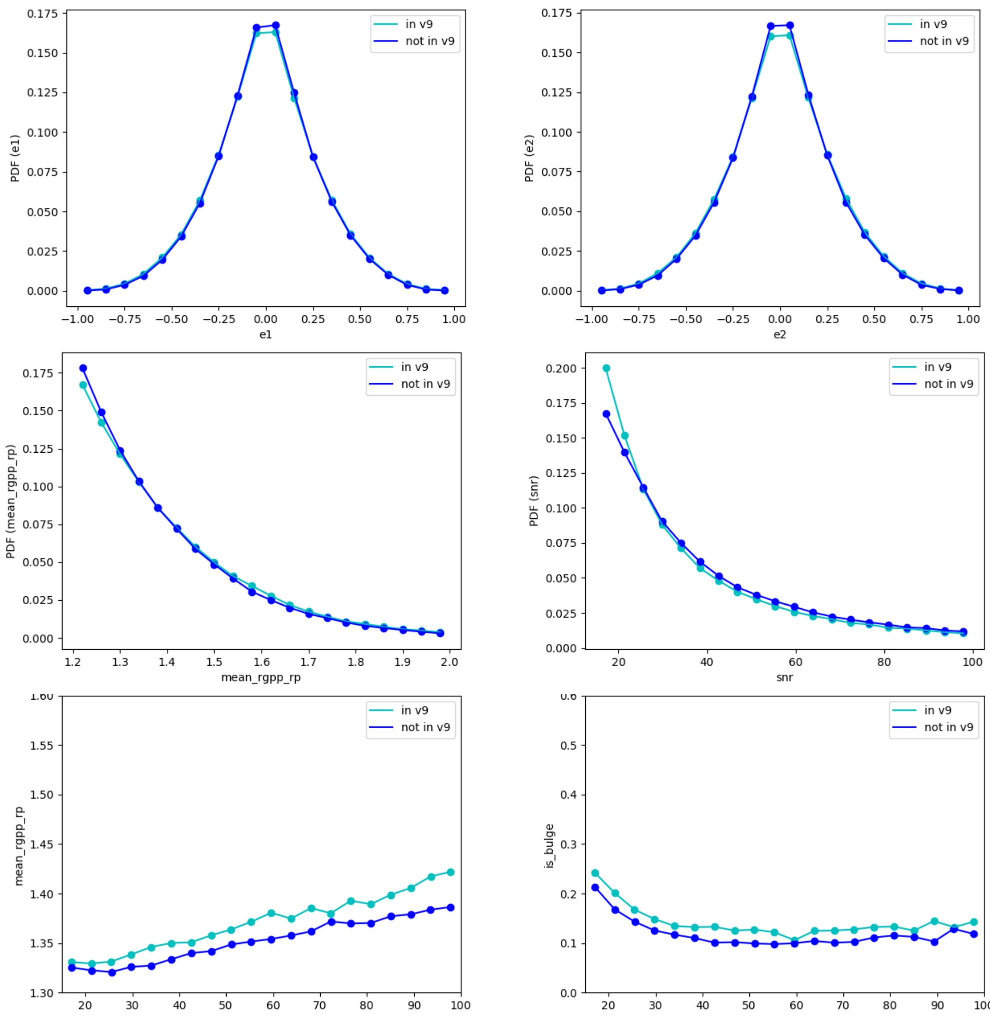

Figure 2.4 More comparisons of official DES-SV IM3SHAPE catalog to runs of IM3SHAPE on additional areas of sky. Top shows histograms of e_1 and e_2, middle shows histograms of R_{gp}/R_p and $(S/N)_w$, bottom shows the dependences of R_{gp}/R_p and bulge fraction on $(S/N)_w$. See bulleted list in Section 2.2.1 for definitions of each quantity.

repeatability, we make these additional catalogs also available. Currently, they can be found in the University of Michigan Deep Blue repository, at:

http://dx.doi.org/10.7302/Z2F769SJ

In the near future, we expect to also make these available at the same location as the official DES SVA1 release[5].

As with the official release, these catalogs are unblinded. Unlike the official release, however, which presents a single list of galaxies over its entire footprint, this data is arranged by cluster (for ease of use with our analysis). Each catalog contains information for galaxies in a $80' \times 80'$ cutout centered at a given cluster, and is named by both the cluster name and the DES tile in which the cluster is found: "[des tile]_[cluster name].fits". Note that these catalogs are not entirely analogous to the official SV catalog. For one, we only measure shapes for galaxies, as stars and other objects are not needed for this analysis. Our catalogs also only extend to a magnitude of 24 in r-band, whereas a small fraction of the objects in the official IM3SHAPE catalog are dimmer (see Figure 29 of Jarvis et al. (2016)). This does not affect our analysis as we use objects with a magnitude of 23 and lower for our main analysis, and only use objects up to a magnitude of 24 for checking the robustness of our results (see Sections 3.4.1 and 3.7.2).

We also include other information necessary for weak lensing studies. Aside from all fields from IM3SHAPE and noise bias calibration (listed and described in Jarvis et al. (2016)), these catalogs contain columns for object positions ("RA_GOLD", "DEC_GOLD") and magnitudes ("MAG_DETMODEL_G", "MAG_DETMODEL_R", "MAG_DETMODEL_I", "MAG_DETMODEL_Z") from the SVA1-GOLD catalog. Additionally, we include mean redshift measurements from two DES photo-z measurement

[5]https://des.ncsa.illinois.edu/releases/sva1

pipelines, TPZ and DESDM Neural Network ("z_TPZ", "z_DESDMnn") (Sánchez et al. (2014)).

For completeness associated with this work, we present catalogs for all the clusters in our analysis, including the ones that are present in the official release. This makes this work more easily reproducible, as all the data is in one place. We also include the extra catalogs around possible clusters that were later dropped from our sample, in order to maximize the part of DES-SV footprint for which shapes are available. The area covered by all catalogs in our repository is shown in Figure 2.5.

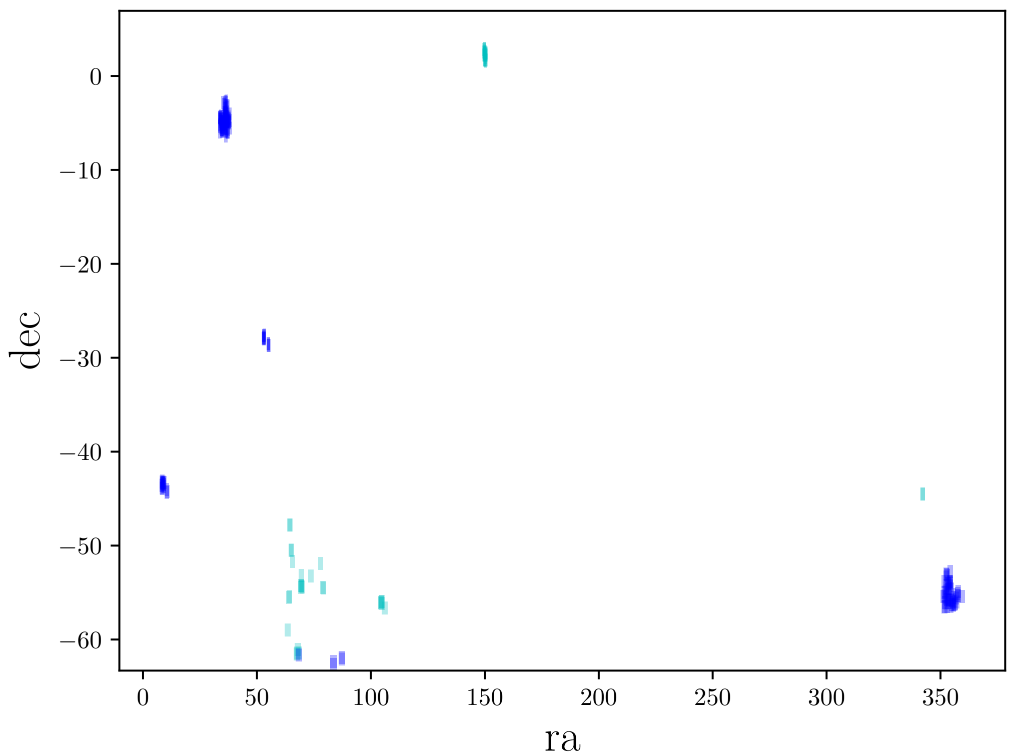

Figure 2.5 Area covered by catalogs provided (arranged by cutouts around clusters). Cyan shows areas for which shape measurements are available through the official DES-SV Im3shape catalog. Blue shows areas for which we run the pipeline ourselves.

2.3 Summary

In this chapter, we discuss the optical data—namely, the galaxy shape catalogs in areas of sky surrounding the DES-SV-XCS cluster sample—that are used through the rest of this dissertation. All shapes are calculated using the IM3SHAPE V9 pipeline and associated noise bias calibrations. Our final optical sample can be divided into two areas of sky:

- areas covered by the official DES SV shape catalogs, for which we use the official data
- areas observed during the DES SV run and for which we have photometric data, but which were excluded from official shape measurements in order to expedite work on the included regions

For the latter areas of sky, we run the IM3SHAPE pipeline ourselves, and conduct quality checks on these additional measurements by comparing ensemble properties with those of the official catalog. We present this data, shapes for an additional $\sim 590,000$ galaxies in the DES-SV sky, for public use. We conclude with additional material in Appendix B—a brief description of how to measure shapes with IM3SHAPE, documenting for use in any future such ventures.

CHAPTER III

Stacked Cluster Weak Lensing Masses

The first step of cluster cosmology is measuring cluster masses. The most direct way of measuring cluster mass uses weak gravitational lensing (WL), quantifying the distortion of background galaxies by large masses in the foreground. Light traveling to the instrument from distant (background) galaxies is bent by the gravitational potential of nearby (foreground) massive objects, such as galaxy clusters. By measuring this distortion in the shapes of the background galaxies, we can calculate the amount of mass necessary in the foreground to create the signal observed. Unfortunately, these measurements are highly susceptible to systematic bias, making it difficult to simultaneously characterize both the data and the errors.

A number of observables, such as X-ray temperature, can serve as proxies for cluster mass (Weinberg et al. (2013)). These observables are relatively easier to measure, making them ideal candidates for conducting large-scale mass measurements. The use of these proxies is limited by the precision to which we understand the mass-observable scaling relationship, $p(O|M, z)$. Further discussion of scaling relationships can be found in Chapter IV. Constraining this relation requires a set of clusters for which both observations of the proxy and reliable direct mass measurements are independently available. In this chapter, we probe such a set of clusters, measuring masses using weak lensing with the aim of comparing to observations of X-ray temperatures.

Using weak lensing to measure cluster mass requires measuring a lensing signal with relatively low noise, which in turn requires measurements of a large number of background galaxies. In order to strengthen the cluster lensing signal—especially for less massive clusters, where the effect is weaker—we bin clusters by temperature and stack the clusters of each bin to measure a combined lensing signal. Stacking is a common method used by several studies to measure cluster mass-observable relationships—see Sheldon et al. (2001), Johnston et al. (2007b), Okabe et al. (2010), Melchior et al. (2017), and Pereira et al. (2017) for a few examples.

These previous studies assume homogeneity of data throughout the cluster sample, allowing them to model stacked cluster lensing signals using a single theoretical signal calculated using a model cluster mass. However, our data is highly patchy, meaning we cannot assume uniform data quality across our cluster sample, or even across the field of a single cluster. For this reason, we develop a way of modeling stacked cluster lensing profiles that takes into account data inhomogeneity, both between clusters and within individual cluster fields. This method gives us the ability to measure cluster masses using any dataset, without needing to exclude clusters for low data quality. This is a great advantage for weak lensing studies, where the signal is only as strong as the abundance of background galaxies, as it allows us to make use of every bit of data available.

This chapter is organized as follows: first, we review the math behind cluster weak lensing, and draw a path from observations to a measured lensing signal. Section 3.2 describes and characterizes the datasets used, followed by our measurement of the lensing signal and errors in Section 3.3. Section 3.5 focuses on our methodology for modeling the lensing signal while taking into account the wide range of cluster redshifts as well as inhomogeneities in our data, and Section 3.6 shows our results. In Section 3.7, we perform various tests to validate our new analysis method, as well as our results. We name our analysis pipeline LensStack, and make it available for public use—Appendix A describes where to find it and how to run it.

3.1 Clusters and Weak Lensing

3.1.1 Halo Mass Profile

The radial mass distribution of a dark matter halo, $\rho(r)$, can be modeled by the Navarro-Frenk-White (NFW) density profile:

$$\rho(r) = \frac{\rho_0}{(r/r_s)(1+r/r_s)^2} \tag{3.1}$$

where ρ_0 and r_s - known as the scale radius - are free parameters (Navarro et al. (1996)).

The halo at redshift z is considered bounded by its virial radius, r_{200}, the radius within which the mass density equals 200 times the critical density of the universe, $\rho_{crit} = \frac{3H^2(z)}{8\pi G}$. The corresponding mass is then:

$$M_{200} = 200\rho_{crit}\frac{4}{3}\pi r_{200}^3 = 100\frac{H^2(z)}{G}r_{200}^3 \tag{3.2}$$

The mass distribution can also be defined by r_{200} - and thus by M_{200} - and a parameter known as concentration, $c = r_{200}/r_s$:

$$\rho(r) = \frac{\delta_c \rho_{crit}}{(rc/r_{200})(1+rc/r_{200})^2} \tag{3.3}$$

where δ_c, known as the halo's characteristic overdensity, is

$$\delta_c = \frac{200}{3}\frac{c^3}{\ln(1+c) - c/(1+c)} \tag{3.4}$$

3.1.2 Shear and Surface Mass Density Contrast

The weak lensing effect a halo has on its surroundings can be distilled into two components, convergence κ and shear γ. Convergence changes the observed size of objects behind the halo, while shear distorts their shapes. The strength of these effects at a distance r from the halo center can be quantified with respect to the halo's surface mass density, $\Sigma(r)$, and the critical surface mass density between the halo and the distorted object, Σ_{crit} (Wright & Brainerd (2000)):

$$\Sigma_{crit} = \frac{C^2}{4\pi G}\frac{D_s}{D_l D_{ls}} \tag{3.5}$$

C is the speed of light, and D_s, D_l, and $D_l s$ denote angular diameter distances - to the source, to the lens, and between the lens and source, respectively (Miralda-Escude (1991)).

The surface mass density of an NFW halo is given as a function of a dimensionless radius $x = r/r_s$ by

$$\Sigma(x) = \begin{cases} \frac{2r_s\delta_c\rho_{crit}}{x^2-1}\left[1 - \frac{2}{\sqrt{1-x^2}}\text{arctanh}\sqrt{\frac{1-x}{1+x}}\right] & x < 1 \\ \frac{2r_s\delta_c\rho_{crit}}{3} & x = 1 \\ \frac{2r_s\delta_c\rho_{crit}}{x^2-1}\left[1 - \frac{2}{\sqrt{x^2-1}}\arctan\sqrt{\frac{x-1}{1+x}}\right] & x > 1 \end{cases} \tag{3.6}$$

Convergence can be expressed simply as

$$\kappa(x) = \frac{\Sigma}{\Sigma_{crit}} \tag{3.7}$$

but shear depends on both the surface mass density at a given radius and the mean surface mass density within that radius, $\overline{\Sigma}(x)$, given by

$$\overline{\Sigma}(x) = \frac{2}{x^2}\int_0^x x'\Sigma(x')dx' \tag{3.8}$$

Shear is then given by

$$\gamma(x) = \frac{\overline{\Sigma}(x) - \Sigma(x)}{\Sigma_{crit}} = \frac{\Delta\Sigma(x)}{\Sigma_{crit}} \tag{3.9}$$

(Wright & Brainerd (2000)).

$\Delta\Sigma$ is known as the surface mass density contrast, and is the lensing observable that we measure and model in this work in order to measure cluster masses.

3.1.3 From Shapes to $\Delta\Sigma$

In a sky free of lenses, galaxies are oriented randomly. Foreground masses (i.e. lenses) distort the shapes of background galaxies, resulting in an observed net tangential orientation of galaxy images. This tangential component of ellipticity is our estimator for shear, and can be calculated for each galaxy in our shape catalog as

$$e_t = -(e_1 - c_1)cos(2\phi) + (e_2 - c_2)sin(2\phi) \tag{3.10}$$

where ellipticities e_1 and e_2, from the IM3SHAPE catalogs [1], are corrected respectively by c_1 and c_2 from the NBC calibrations, and

$$\phi = \arctan\left(\frac{\Delta dec}{\Delta RA}\right) \tag{3.11}$$

where ΔRA and Δdec give the position of the galaxy on the sky with respect to the lens. For each individual galaxy, this distortion is much smaller than the galaxy's intrinsic ellipticity. It is only by combining the signals from thousands of background galaxies that we can measure a visible lensing signal:

$$g_t = \frac{\sum_i w^j e_t^j}{\sum_j w^j(1+m^j)} \tag{3.12}$$

Here, g_t is the net tangential ellipticity, e_t^j is the individual tangential ellipticity of each galaxy j, w^j is the weight for each galaxy, and m^j is the multiplicative correction for each galaxy from the noise bias calibrations.

One thing to note is that e_t is an estimator for shear, but $e_t \neq \gamma$. From the ellipticities we observe in the sky, we measure shear modified by convergence, called

[1] Note that the signs on the terms in Eqn. 3.10 are dependent on the conventions used by the shape catalogs—our first term is negative and the second positive because e_1 and e_2 are defined as such by IM3SHAPE.

"reduced shear" and quantified for each galaxy as:

$$e_t^j = \frac{\gamma^j}{1-\kappa^j} \tag{3.13}$$

From this, we measure a modified surface mass density contrast for each galaxy:

$$\Delta\Sigma^j = \Sigma_{crit}^j e_t^j \tag{3.14}$$

For simplicity, we will henceforth use $\Delta\Sigma$ to refer to the modified surface mass density contrast, both in our observations and our theoretical modeling.

From the ensemble of background galaxies, we measure a net lensing signal:

$$\Delta\Sigma = \frac{\sum_i \Sigma_{crit}^j w^j e_t^j}{\sum_j w^j (1+m^j)} \tag{3.15}$$

However, for galaxies with redshift z only slightly greater than z_{lens}, D_{ls} is small, making Σ_{crit} extremely large.To prevent these galaxies from disproportionately skewing the net $\Delta\Sigma$, we scale galaxy weights by Σ_{crit}^{-2}, giving us a final $\Delta\Sigma$ of

$$\Delta\Sigma = \frac{\sum_i \Sigma_{crit}^i \frac{w^i}{{\Sigma_{crit}^i}^2} e_t^i}{\sum_i \frac{w^i}{{\Sigma_{crit}^i}^2}(1+m^i)} \tag{3.16}$$

3.2 Data

In this work, we analyze a set of 133 clusters spanning a wide range in both T_X and z. All optical data for lensing measurements are taken from the Dark Energy Survey Science Verification data, and all X-ray data and temperature calculations are provided by the XMM Cluster Survey (XCS). More about the surveys and initial data reductions can be found in Sections 1.4 and 1.5. Figure 3.1 shows optical data for a single cluster superimposed on X-ray contours.

We work with the set of clusters in the XCS DR2 dataset for which we have corresponding galaxy shapes from DES SV. While some of these shape catalogs are

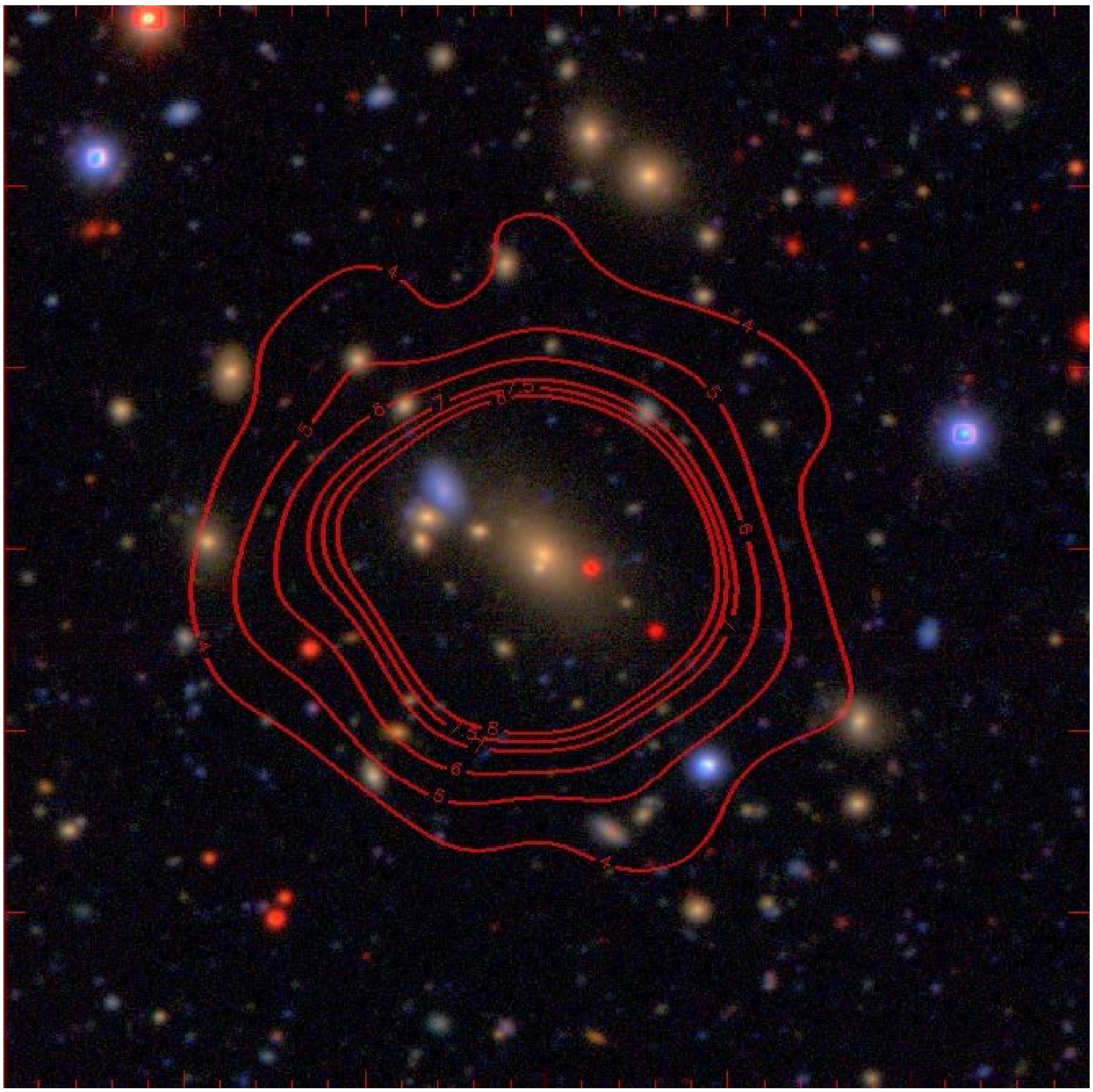

Figure 3.1 Image of cluster with overlaid optical and X-ray data—coadded optical image from DES, X-ray flux contours from XCS.

part of the official DES SV data release, a number of clusters reside in areas of sky observed during the SV runs, but not processed as part of the official release. For these, we run the DES shape-measurement pipelines separately, and validate the catalogs before use. Further details of these measurements are in Chapter II.

Our analysis assumes that the lensing signal around any given cluster is solely a result of the presence of that cluster. However, several members of our sample sit very close on the sky to other clusters, leading to contamination of our measured signal by lensing from these nearby structures—for example, see Figure 3.2. To avoid this effect, we inspect each cluster in this set by eye, and remove those which are too close to other clusters. Table 3.1 lists the clusters we removed with the reasons for exclusion. The final sample used in this work is described in Tables 3.2-3.5.

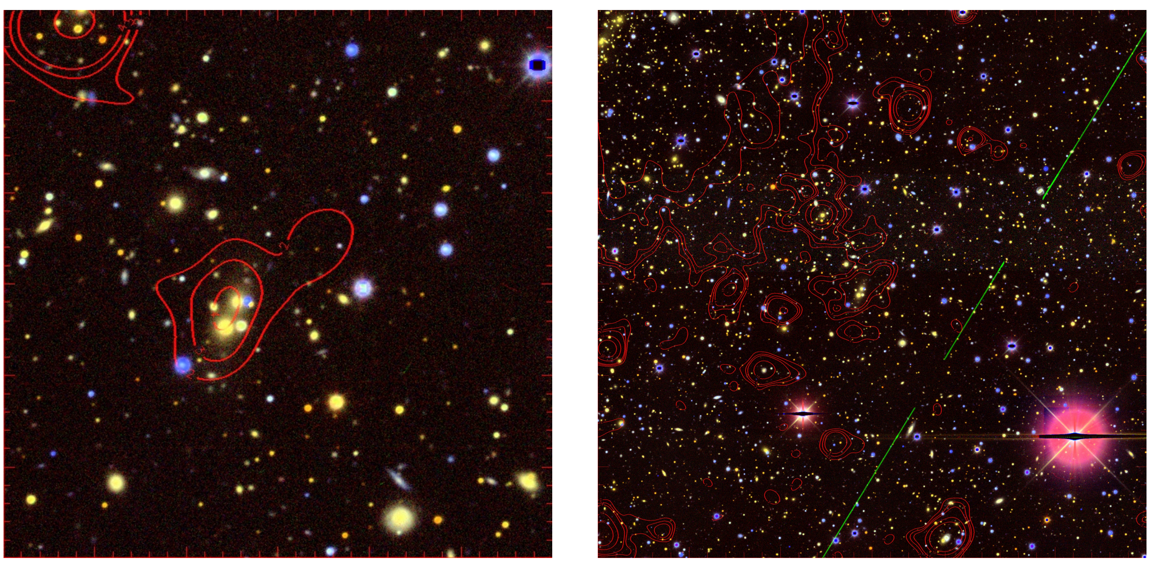

(a) (b)

Figure 3.2 Cluster to be excluded due to nearby structure. (a) Close-up cutout of this cluster, where all seems well. (b) Zooming out, we see a massive cluster nearby (upper left corner). Most of the lensing signal attributed to the original cluster (see (a)) is in actuality an effect of the nearby cluster. For this reason, the cluster in (a) is excluded from our lensing analysis.

Table 3.1. List of clusters excluded from weak lensing analysis due to nearby structure.

Cluster Name from XCS	Reason for Exclusion
J003659.3-431826.9	large X-ray structure nearby
J065755.8-560244.3	massive cluster nearby
J100141.7+022538.0	low-z cluster in line of sight
J043750.2-541940.8	massive cluster nearby
J022530.8-041421.1	another cluster very close by
J003407.6-432236.2	two massive clusters nearby
J022156.8-054521.9	low-z cluster in line of sight
J041328.7-585844.3	massive cluster nearby
J022912.4-060122.5	massive clusters nearby
J021612.5-041426.2	low-z cluster in line of sight
J022512.2-062305.1	low-z cluster in line of sight
J065900.5-560927.5	low-z cluster in line of sight

3.3 Cluster Stacking

Weak lensing measurements require a large sample of background galaxies. The low numbers of background galaxies behind individual clusters are not sufficient to detect a significant lensing signal, especially for low-mass clusters, where the lensing effect is weaker. We stack multiple clusters and combine their background galaxies in an effort to raise the shear signal-to-noise ratio. Stacking clusters also helps average out any non-spherical structure of individual clusters, as we expect these extraneous structures to be oriented randomly over a large sample set. Stacking is a common method used by several studies to measure cluster mass-observable relationships—see Sheldon et al. (2001), Johnston et al. (2007b), Okabe et al. (2010), Melchior et al. (2017), and Pereira et al. (2017) for a few examples.

We bin the cluster sample by X-ray temperature in order to constrain the $M - T_x$ scaling relation. Our sample is divided into four temperature bins such that the stacked bin temperatures are fairly evenly distributed in temperature logspace. The large temperature range of the sample allows us to examine masses for both low- and high-temperature clusters. Details of each bin are given in Table 3.6. Temperature (k_bT in units of keV) and redshift distributions of each bin are shown in Figure 3.3.

Table 3.2. The set of clusters used in this work - the DES-SV-XCS cluster sample, excluding clusters with large structures nearby. Column 1 is the cluster name given by XCS, and column 2 gives the DES tiling in which it is observed. Columns 3 and 4 give the position of the cluster's X-ray barycenter. Column 5 is the cluster redshift. Columns 6-8 give the X-ray temperature, along with upper and lower bounds on uncertainties. Columns 9-13 give the cluster color through various combinations of filters.

XCS Name	DES Tile	RA	Dec	z	k_bT_x $[keV]$	$k_bT_x lower$ $[keV]$	$k_bT_x upper$ [keV]	$g-r$	$g-i$	$r-i$	$i-z$	$r-z$
J021757.3-045140.8	DES0218-0458	34.48875	-4.86133333	0.5124	0.23517	0.180649	0.374945	1.79695	2.39086	0.396548	0.32772	0.812198
J021653.2-041723.7	DES0218-0416	34.22166667	-4.28991667	0.1527	0.256319	0.192879	0.49693	1.07568	1.51309	0.419088	0.28262	0.676063
J021648.4-043321.3	DES0218-0416	34.20166667	-4.55591667	0.4211	0.339173	0.0	0.611885	1.01313	1.40858	0.540167	0.360324	0.877171
J021755.3-052708.0	DES0219-0541	34.48041667	-5.45222222	0.2495	0.342073	0.297728	0.413773	1.20745	1.71587	0.476861	0.326444	0.812541
J233403.8-554903.9	DES2333-5540	353.5158333	-55.81775	0.33	0.595134	0.462371	0.760975	1.42099	2.02267	0.497991	0.317196	0.848616
J232940.9-544715.3	DES2328-5457	352.4204167	-54.78758333	0.145	0.606448	0.537242	0.671771	1.01894	1.39219	0.460308	0.371864	0.832172
J022456.1-050802.0	DES0224-0458	36.23375	-5.13388889	0.0842	0.6191	0.59328	0.644432	0.895158	1.33113	0.411109	0.332273	0.743382
J003429.6-434715.7	DES0034-4331	8.62333333	-43.78769444	0.2042	0.650408	0.604296	0.696994	1.2321	1.69086	0.456946	0.337124	0.773715
J234054.4-554256.6	DES2338-5540	355.2266667	-55.71572222	0.17	0.674556	0.533798	0.865319	1.07615	1.51787	0.421598	0.315363	0.721835
J070411.4-563929.1	DES0703-5622	106.0475	-56.65808333	0.375	0.728678	0.453689	1.197	1.54552	2.12831	0.567081	0.308768	0.905169
J021547.3-045030.6	DES0215-0458	33.9481	-4.8375	0.9225	0.73741	0.553912	1.04452	1.76784	2.60221	1.01361	0.797637	1.90578
J021843.7-053257.6	DES0219-0541	34.68208333	-5.54933333	0.38	0.775081	0.679998	0.927261	1.62275	2.15785	0.523614	0.35488	0.878494
J232645.9-534839.3	DES2327-5331	351.69125	-53.81091667	0.19	0.866581	0.789444	0.959474	1.14317	1.61234	0.469167	0.316184	0.780831
J021741.6-045148.0	DES0218-0458	34.42333333	-4.86333333	0.5187	0.925108	0.729506	1.20761	1.53064	2.18584	0.700861	0.369553	1.08846
J022318.6-052708.2	DES0222-0541	35.8275	-5.45227778	0.2106	0.953531	0.895091	1.01451	1.20816	1.70441	0.463412	0.306031	0.802287
J233204.9-551242.9	DES2333-5457	353.0204167	-55.21191667	0.32	1.04931	0.914511	1.24556	1.45085	1.9452	0.508205	0.329881	0.838044
J022246.3-035151.2	DES0223-0333	35.69291667	-3.86422222	0.12	1.11861	0.888381	5.14505	0.92718	1.34455	0.423787	0.272454	0.719254
J233133.8-562804.6	DES2329-5622	352.8908333	-56.46794444	0.185	1.122	0.926874	1.54072	1.12211	1.58149	0.459383	0.353484	0.812868
J234120.8-560358.3	DES2339-5622	355.3366667	-56.06619444	0.38	1.15369	0.763955	2.04919	1.73725	2.15644	0.512229	0.368537	0.90081
J043706.9-542919.0	DES0435-5414	69.27875	-54.48861111	0.56	1.15974	0.962535	1.45717	1.89013	2.76319	0.822674	0.403802	1.25665
J023052.9-042050.7	DES0229-0416	37.72041667	-4.34741667	0.105	1.25558	1.19326	1.3251	1.02525	1.22165	0.364692	0.261673	0.590105
J234311.1-555249.8	DES2344-5540	355.79625	-55.8805	0.225	1.29433	1.14344	1.48213	1.28319	1.62887	0.466553	0.332012	0.798565
J095924.7+014614.1	DES0959+0126	149.8529167	1.77058333	0.1243	1.29764	1.18519	1.41924	0.943542	1.38673	0.443188	0.337582	0.78077
J022349.7-053643.5	DES0224-0541	35.962	-5.612194	0.49	1.31395	1.04757	1.85403	1.79302	2.46325	0.694256	0.392442	1.08374
J022726.5-043207.1	DES0226-0416	36.86041667	-4.53530556	0.3085	1.31658	1.2222	1.42734	1.43126	1.9499	0.499084	0.315662	0.814746
J233706.9-541909.8	DES2337-5414	354.27875	-54.31938889	0.52	1.3225	1.05266	1.75577	1.62224	2.39258	0.756497	0.400809	1.15731
J022454.1-032846.3	DES0223-0333	36.22541667	-3.47952778	0.22	1.34859	1.03484	1.88463	1.25449	1.66434	0.355102	0.349962	0.690789
J022401.9-050528.4	DES0224-0458	36.00791667	-5.09122222	0.3265	1.35068	1.14641	1.67069	1.5451	2.10549	0.56039	0.299109	0.867254
J022347.6-025127.1	DES0223-0250	35.94833333	-2.85752778	0.175	1.35508	1.21223	1.56132	1.11237	1.5527	0.440325	0.335468	0.775793
J021940.8-055043.7	DES0219-0541	34.919917	-5.845472	0.729	1.36081	1.12005	1.91082	1.81445	2.81939	0.98587	0.472127	1.458
J022433.9-041432.7	DES0223-0416	36.14125	-4.24241667	0.2619	1.41376	1.3264	1.51493	1.34852	1.80676	0.499005	0.299499	0.810402
J100023.1+022358.0	DES1000+0209	150.0909	2.3912	0.215	1.42181	1.28034	1.6143	1.24417	1.71588	0.471713	0.335582	0.807295
J021945.5-044834.3	DES0218-0458	34.93958333	-4.80952778	0.9173	1.42625	1.09382	2.41272	2.22418	2.97587	1.17328	0.803614	1.94279
J004157.8-442026.5	DES0042-4414	10.49083333	-44.34069444	0.35	1.47265	1.1986	6.80398	1.54136	2.08545	0.54409	0.314084	0.858174
J022808.6-053543.6	DES0227-0541	37.03583333	-5.59544444	0.2	1.48318	1.27338	1.83874	1.15976	1.66466	0.516912	0.344301	0.850328
J233637.8-524409.4	DES2336-5248	354.1575	-52.73594444	0.555	1.52956	1.31903	1.90467	1.2963	2.21378	0.836835	0.391301	1.20254
J022318.3-051209.8	DES0224-0458	35.82625	-5.20272	0.332267	1.58621	1.12652	4.05797	1.37378	1.98053	0.510078	0.336751	0.865541

Table 3.3. Table 3.2, contd. The set of clusters used in this work - the DES-SV-XCS cluster sample, excluding clusters with large structures nearby. Column 1 is the cluster name given by XCS, and column 2 gives the DES tiling in which it is observed. Columns 3 and 4 give the position of the cluster's X-ray barycenter. Column 5 is the cluster redshift. Columns 6-8 give the X-ray temperature, along with upper and lower bounds on uncertainties. Columns 9-13 give the cluster color through various combinations of filters.

XCS Name	DES Tile	RA	Dec	z	k_bT_x $[keV]$	$k_bT_x lower$ $[keV]$	$k_bT_x upper$ [keV]	$g-r$	$g-i$	$r-i$	$i-z$	$r-z$
J022307.9-041257.2	DES0223-0416	35.78291667	-4.21588889	0.63	1.6135	1.25913	3.13495	1.69784	2.78367	0.92724	0.432703	1.40667
J022303.2-043620.3	DES0221-0458	35.76333333	-4.60563889	1.219	1.6225	1.31176	2.26561	1.62432	2.6269	0.903844	1.03144	2.13894
J003321.0-433737.1	DES0034-4331	8.3375	-43.62697222	0.3809	1.6497	1.35909	2.18443	1.66812	2.19449	0.558507	0.344792	0.903299
J100027.1+022131.7	DES1000+0209	150.1129167	2.35880556	0.2207	1.65084	1.31396	2.25364	1.19647	1.66291	0.466437	0.333833	0.80892
J022405.8-035505.5	DES0223-0333	36.02416667	-3.91819444	0.44	1.65112	1.16401	3.03758	1.61329	2.37878	0.637787	0.352684	0.935589
J023052.4-045123.5	DES0230-0458	37.71833333	-4.85652778	0.3	1.65765	1.32269	2.54678	1.41164	2.00803	0.546858	0.29081	0.850641
J095901.2+024740.4	DES0957+0252	149.755	2.79455556	0.49	1.66163	1.39325	2.18372	1.79744	2.5287	0.731264	0.399382	1.13065
J022103.2-050612.0	DES0221-0458	35.26333333	-5.10333333	0.2765	1.66678	1.10726	2.65435	1.3623	2.0008	0.513187	0.299122	0.806776
J022204.5-043239.4	DES0221-0416	35.51875	-4.54427778	0.315	1.68655	1.43939	2.09332	1.53668	2.06157	0.524896	0.306389	0.833642
J021943.8-045314.1	DES0218-0458	34.9325	-4.88725	0.3323	1.70321	1.44634	2.1419	1.52271	2.10447	0.547059	0.326075	0.873134
J003518.1-433402.4	DES0034-4331	8.82541667	-43.56733333	0.44	1.70535	1.6307	1.7875	1.45128	1.99727	0.475631	0.321639	0.817694
J022532.0-035509.5	DES0223-0416	36.38333333	-3.91930556	0.7712	1.71997	1.34262	2.30656	1.99052	3.28614	1.28826	0.362371	1.7687
J022357.5-043520.7	DES0223-0416	35.98958333	-4.58908333	0.4974	1.7876	1.49906	2.21237	1.70297	2.4931	0.759066	0.352984	1.11881
J022342.3-050200.9	DES0224-0458	35.92625	-5.03358333	0.8568	1.80665	1.43772	2.52818	1.97651	3.09719	1.18828	0.688583	1.8979
J023037.2-045929.5	DES0230-0458	37.655	-4.99152778	0.3	1.84803	1.62556	2.17681	1.46417	1.979	0.496979	0.291445	0.817843
J233835.2-543729.5	DES2338-5457	354.6466667	-54.62486111	0.365	1.85557	1.5382	2.40552	1.66635	2.17502	0.464312	0.36557	0.849744
J022042.7-052550.0	DES0222-0541	35.17791667	-5.43055556	0.5477	1.93471	1.5444	2.52561	1.74758	2.43993	0.751865	0.41517	1.20766
J232804.7-563004.5	DES2329-5622	352.0195833	-56.50125	0.185	1.94646	1.65068	2.3638	1.13112	1.59268	0.456401	0.344552	0.806105
J232952.7-532105.2	DES2327-5331	352.4695833	-53.35144444	0.525	1.97668	1.49779	2.98688	1.63801	2.35862	0.756987	0.366103	1.17655
J003545.5-431756.0	DES0034-4331	8.93958333	-43.29888889	0.4109	1.99521	1.44678	2.75588	1.72114	2.12009	0.569434	0.387328	0.930278
J095902.7+025544.9	DES0957+0252	149.76125	2.92913889	0.3487	2.02349	1.75137	2.38555	1.64124	2.23148	0.561112	0.336058	0.88522
J235058.9-552208.4	DES2349-5540	357.747917	-55.368361	0.14	2.03796	1.70634	2.55327	1.00594	1.44719	0.441259	0.344298	0.801006
J233546.6-535039.3	DES2337-5331	353.9441667	-53.84425	0.54	2.04402	1.67195	2.57088	1.84131	2.56331	0.789152	0.412592	1.21113
J233037.2-554340.2	DES2328-5540	352.655	-55.72783333	0.325	2.06867	1.56648	3.04236	1.49289	2.00782	0.514928	0.314392	0.821523
J043021.9-613158.8	DES0428-6122	67.59125	-61.533	0.075	2.08008	1.37525	6.99705	0.877642	1.30566	0.382332	0.312471	0.681488
J022524.8-044043.4	DES0224-0458	36.35333333	-4.67872222	0.2647	2.08725	1.30789	4.46585	1.41825	1.91924	0.500995	0.315375	0.816369
J042017.5-503153.9	DES0419-5040	65.07291667	-50.53163889	0.445	2.11122	1.95557	2.29472	1.79634	2.40126	0.569001	0.383088	0.964055
J041644.8-552506.6	DES0417-5540	64.18666667	-55.4185	0.415	2.16923	1.82157	2.71095	1.68698	2.26623	0.593921	0.308045	0.91265
J021734.7-051327.6	DES0218-0458	34.39458333	-5.22433333	0.6467	2.1785	1.74224	3.01444	1.71649	2.75637	1.01444	0.364539	1.3783
J235009.3-551957.9	DES2349-5540	357.539583	-55.33275	0.42	2.17856	1.83411	2.66587	1.73996	2.3604	0.585364	0.320954	0.861151
J233216.0-544205.5	DES2333-5457	353.0666667	-54.70152778	0.315	2.18402	1.80567	2.77462	1.45461	1.94473	0.489203	0.356097	0.82984
J065744.2-560817.0	DES0658-5622	104.4341667	-56.13805556	0.34	2.2019	2.00394	2.42992	1.45942	1.9911	0.531683	0.337655	0.873194
J022722.4-032142.8	DES0226-0333	36.84333333	-3.36188889	0.33	2.24681	2.0882	2.43619	1.66733	2.09698	0.497304	0.398674	0.895206
J023009.8-054039.3	DES0230-0541	37.54083333	-5.67758333	0.49	2.29182	1.26567	4.25778	1.76457	2.49111	0.726533	0.337942	1.03615
J233000.5-543706.3	DES2328-5457	352.5020833	-54.61841667	0.1763	2.30973	2.13561	2.51156	1.13044	1.55662	0.443968	0.351273	0.795241
J022509.7-040137.9	DES0223-0416	36.29041667	-4.02719444	0.1732	2.31896	1.72342	3.67876	1.02991	1.45744	0.427529	0.323182	0.755298
J095951.2+014045.8	DES0959+0126	149.9633333	1.67938889	0.3702	2.35732	2.15382	2.6094	1.68242	2.23286	0.537213	0.343657	0.89422

Table 3.4. Table 3.2, contd. The set of clusters used in this work - the DES-SV-XCS cluster sample, excluding clusters with large structures nearby. Column 1 is the cluster name given by XCS, and column 2 gives the DES tiling in which it is observed. Columns 3 and 4 give the position of the cluster's X-ray barycenter. Column 5 is the cluster redshift. Columns 6-8 give the X-ray temperature, along with upper and lower bounds on uncertainties. Columns 9-13 give the cluster color through various combinations of filters.

XCS Name	DES Tile	RA	Dec	z	k_bT_x $[keV]$	$k_bT_x lower$ $[keV]$	$k_bT_x upper$ [keV]	$g-r$	$g-i$	$r-i$	$i-z$	$r-z$
J023026.7-043444.5	DES0229-0416	37.61125	-4.57902778	0.33	2.36937	1.81555	3.52659	1.47784	2.06939	0.527824	0.249001	0.776825
J234142.9-555748.9	DES2344-5540	355.42875	-55.96358333	0.195	2.37922	2.05101	2.83087	1.17444	1.65703	0.476544	0.335763	0.806356
J233955.1-561519.6	DES2339-5622	354.9795833	-56.25544444	0.4	2.44045	1.60948	4.04356	1.75289	2.26709	0.555377	0.326132	0.861146
J041629.2-553254.9	DES0417-5540	64.12166667	-55.54858333	0.505	2.45203	1.79293	4.22874	1.53502	2.52659	0.777283	0.349056	1.05834
J232713.8-560333.5	DES2329-5622	351.8075	-56.05930556	0.965	2.46776	2.0058	3.12617	1.25902	2.7606	1.18568	0.656445	1.91084
J003306.4-433340.0	DES0034-4331	8.27666667	-43.56111111	0.3798	2.47798	1.54221	5.75969	1.67626	2.24353	0.567261	0.348971	0.916232
J022829.7-031256.6	DES0228-0250	37.12375	-3.21572222	0.325	2.48747	2.04088	3.08723	1.65836	2.06409	0.424595	0.373097	0.813737
J022917.7-055345.9	DES0227-0541	37.32375	-5.89608333	0.32	2.48861	1.96206	3.29452	1.47617	2.00564	0.536754	0.288944	0.79598
J003346.3-431729.7	DES0034-4331	8.44291667	-43.29158333	0.2199	2.50623	2.35327	2.67049	1.2515	1.71764	0.466142	0.332206	0.798348
J022417.1-050314.8	DES0224-0458	36.07125	-5.05411111	0.1515	2.50831	1.75951	4.08258	1.08186	1.37362	0.407096	0.354315	0.746199
J233644.6-534806.9	DES2337-5331	354.1916	-53.7949	0.35	2.54074	1.67795	4.64263	1.55095	2.08819	0.526855	0.353593	0.880448
J233345.8-553826.9	DES2333-5540	353.4408333	-55.64080556	0.78	2.55753	1.75264	4.1716	1.88277	3.11169	1.20035	0.481649	1.69809
J100043.0+014559.2	DES0959+0126	150.1791667	1.76644444	0.3464	2.58357	2.17911	3.15885	1.58854	2.14123	0.532038	0.310607	0.87062
J022024.7-050232.0	DES0221-0458	35.10291667	-5.04222222	0.125	2.5947	2.31125	2.94407	0.942593	1.35799	0.400329	0.362151	0.801966
J234231.5-562105.9	DES2344-5622	355.63125	-56.35163889	0.38	2.68328	2.3208	3.14821	1.7961	2.37175	0.57043	0.349074	0.872163
J021529.0-044052.8	DES0215-0458	33.87083333	-4.68133333	0.355	2.68598	2.25595	3.33397	1.59431	2.15377	0.532644	0.324425	0.826601
J233745.5-562757.7	DES2339-5622	354.4395833	-56.46602778	0.39	2.7336	2.11926	3.65245	1.25101	2.27499	0.535697	0.32577	0.861468
J021832.5-050053.3	DES0218-0458	34.63541667	-5.01480556	0.5262	2.77872	2.3373	3.35064	1.51863	2.27943	0.6323	0.346755	1.03994
J003548.1-432232.8	DES0034-4331	8.95041667	-43.37577778	0.628	2.86782	2.43418	3.44477	1.7807	2.71726	1.01151	0.377247	1.41702
J233043.1-530321.7	DES2331-5248	352.6795833	-53.05602778	0.81	2.93258	2.05814	4.48744	1.78035	2.78511	1.12945	0.579349	1.71781
J233607.6-535232.4	DES2337-5331	354.0316667	-53.87566667	0.525	2.94754	2.34066	3.90463	1.79353	2.56205	0.760494	0.406365	1.14855
J003627.6-432830.3	DES0038-4331	9.115	-43.47508333	0.42	2.98548	1.7816	5.18471	1.65622	2.24282	0.586607	0.325032	0.920946
J021803.4-055526.5	DES0219-0541	34.51416667	-5.92402778	0.3893	3.03237	1.73798	12.454	1.81011	2.42229	0.568949	0.356108	0.914849
J034025.8-284031.3	DES0339-2832	55.108125	-28.673722	0.067	3.06766	2.87918	3.27405	0.844974	1.31657	0.471599	0.31493	0.742816
J003428.0-431854.2	DES0034-4331	8.61666667	-43.31505556	0.3977	3.07993	2.92718	3.24303	1.73641	2.32922	0.592812	0.329626	0.930458
J034106.0-284132.2	DES0342-2832	55.275	-28.69227778	0.505	3.13824	2.28628	4.92239	1.79644	2.49096	0.674768	0.356646	1.10937
J234806.2-560121.1	DES2349-5540	357.0258333	-56.02252778	0.475	3.14762	2.54428	4.03638	1.83592	2.42511	0.567484	0.385837	0.953321
J234730.6-553322.9	DES2349-5540	356.8775	-55.55636111	0.405	3.188	2.53698	4.1592	1.78314	2.3549	0.577354	0.337046	0.897384
J022457.9-034849.4	DES0223-0333	36.24125	-3.81372222	0.6189	3.21416	2.7727	3.76913	1.72091	2.65407	0.933955	0.46456	1.40732
J042226.4-514025.8	DES0423-5123	65.61	-51.67383333	0.58	3.22887	2.96279	3.53116	1.76685	2.65889	0.903221	0.392495	1.31282
J100047.3+013927.8	DES0959+0126	150.1970833	1.65772222	0.22	3.23242	3.08027	3.42052	1.23524	1.78913	0.469988	0.364558	0.841095
J232956.6-560808.0	DES2329-5622	352.4858333	-56.13555556	0.44	3.31132	2.77724	4.03831	1.78114	2.37921	0.5906	0.351589	0.954457
J043218.6-610351.9	DES0431-6039	68.0775	-61.06441667	0.45	3.31441	2.6053	4.49172	1.75384	2.36784	0.631486	0.349513	0.95039
J043327.2-612717.6	DES0433-6122	68.36333333	-61.45488889	0.72	3.33872	2.57596	4.49711	1.92094	3.02648	1.1559	0.436911	1.62551
J022709.9-041800.5	DES0226-0416	36.79125	-4.30013889	1.0308	3.38586	2.57342	4.80427	1.70735	2.67976	1.08509	0.77355	1.90824
J022403.8-041332.8	DES0223-0416	36.01583333	-4.22577778	1.0524	3.50943	3.25569	3.79799	2.34417	2.64646	1.12053	1.00107	2.07412
J003339.4-435422.6	DES0034-4414	8.41416667	-43.90627778	0.2088	3.61297	2.34937	6.75705	1.16876	1.55215	0.454461	0.307383	0.734768

Table 3.5. Table 3.2, contd. The set of clusters used in this work - the DES-SV-XCS cluster sample, excluding clusters with large structures nearby. Column 1 is the cluster name given by XCS, and column 2 gives the DES tiling in which it is observed. Columns 3 and 4 give the position of the cluster's X-ray barycenter. Column 5 is the cluster redshift. Columns 6-8 give the X-ray temperature, along with upper and lower bounds on uncertainties. Columns 9-13 give the cluster color through various combinations of filters.

XCS Name	DES Tile	RA	Dec	z	k_bT_x $[keV]$	$k_bT_x lower$ $[keV]$	$k_bT_x upper$ [keV]	$g-r$	$g-i$	$r-i$	$i-z$	$r-z$
J051141.2-515420.8	DES0510-5205	77.92166667	-51.90577778	0.665	3.82909	3.45697	4.28096	1.66474	2.71433	1.01692	0.465019	1.45264
J022400.3-032520.5	DES0223-0333	36.00125	-3.42236111	0.895	3.96039	2.25182	9.6884	2.28162	2.89822	1.04111	0.620849	1.83259
J232633.3-550116.3	DES2328-5457	351.63875	-55.02119444	0.43	3.96843	3.32605	4.78923	1.80558	2.34403	0.596227	0.362162	0.958389
J034004.2-283159.2	DES0339-2832	55.0175	-28.53311111	0.27	4.02992	2.06039	7.39042	1.38731	1.88655	0.49213	0.320491	0.803619
J023138.4-043439.1	DES0232-0416	37.91	-4.57752778	0.9749	4.12793	1.49112	12.2527	2.07521	2.81079	0.916528	0.862417	1.8537
J095823.4+024850.9	DES0957+0252	149.5963	2.8189	0.38	4.4599	3.78328	5.3204	1.63382	2.20371	0.565363	0.322432	0.887795
J232801.9-545550.1	DES2328-5457	352.0079167	-54.93058333	1.225	4.47352	2.26773	9.74588	1.37589	2.39352	1.12039	0.924643	2.11529
J095737.1+023428.9	DES0957+0252	149.4045833	2.57469444	0.3733	4.48033	3.79843	5.36205	1.75012	2.36238	0.575888	0.344683	0.914171
J021441.2-043313.8	DES0215-0416	33.67166667	-4.55383333	0.1416	4.49236	4.35318	4.64711	1.01643	1.43143	0.397992	0.340846	0.746667
J041805.0-474941.8	DES0419-4748	64.52083333	-47.82827778	0.545	4.78799	3.72724	6.30757	1.8686	2.81017	0.934855	0.372505	1.31144
J023337.7-053026.5	DES0233-0541	38.407083	-5.507361	0.441	4.88583	4.14034	5.82911	1.73532	2.33776	0.531508	0.324094	0.721081
J100201.4+021334.2	DES1003+0209	150.505917	2.226167	0.838	4.88741	4.322	5.59096	1.78804	2.97196	1.26011	0.543732	1.71125
J095940.7+023110.8	DES1000+0209	149.9195833	2.51966667	0.7297	4.97681	4.40607	5.69434	1.86364	2.99536	1.14184	0.464832	1.56582
J022543.9-031147.1	DES0226-0250	36.43291667	-3.19641667	0.165	5.01447	4.44121	5.74944	1.09031	1.49031	0.387738	0.352628	0.719408
J034025.8-282830.6	DES0339-2832	55.1075	-28.47516667	0.38	5.02908	3.2456	9.56934	1.53932	2.12494	0.572284	0.326762	0.90886
J232842.9-553357.4	DES2328-5540	352.17875	-55.56594444	0.805	5.17507	3.7352	7.28742	1.44318	2.36629	1.14611	0.524169	1.90444
J023142.2-045253.1	DES0233-0458	37.92583333	-4.88141667	0.195	5.42064	5.2736	5.57406	1.17916	1.6364	0.457235	0.367788	0.770128
J051636.6-543120.8	DES0514-5414	79.1525	-54.52244444	0.355	6.25923	6.14724	6.37558	1.57618	2.10592	0.529744	0.335357	0.865101
J041722.7-474847.1	DES0415-4748	64.34458333	-47.81308333	0.55	6.7404	6.34136	7.18995	1.85596	2.82065	0.921972	0.384345	1.33594
J043818.3-541916.5	DES0440-5414	69.57625	-54.32125	0.42	7.98878	7.67708	8.31925	1.8226	2.42209	0.590727	0.361938	0.940805
J065828.8-555640.8	DES0659-5540	104.62125	-55.944861	0.297	9.38927	9.22382	9.56305	1.53882	2.06713	0.550003	0.333285	0.896175
J224844.9-443141.7	DES2247-4414	342.1870833	-44.52825	0.405	11.0916	10.8634	11.3294	1.67024	2.24872	0.567528	0.321582	0.871572

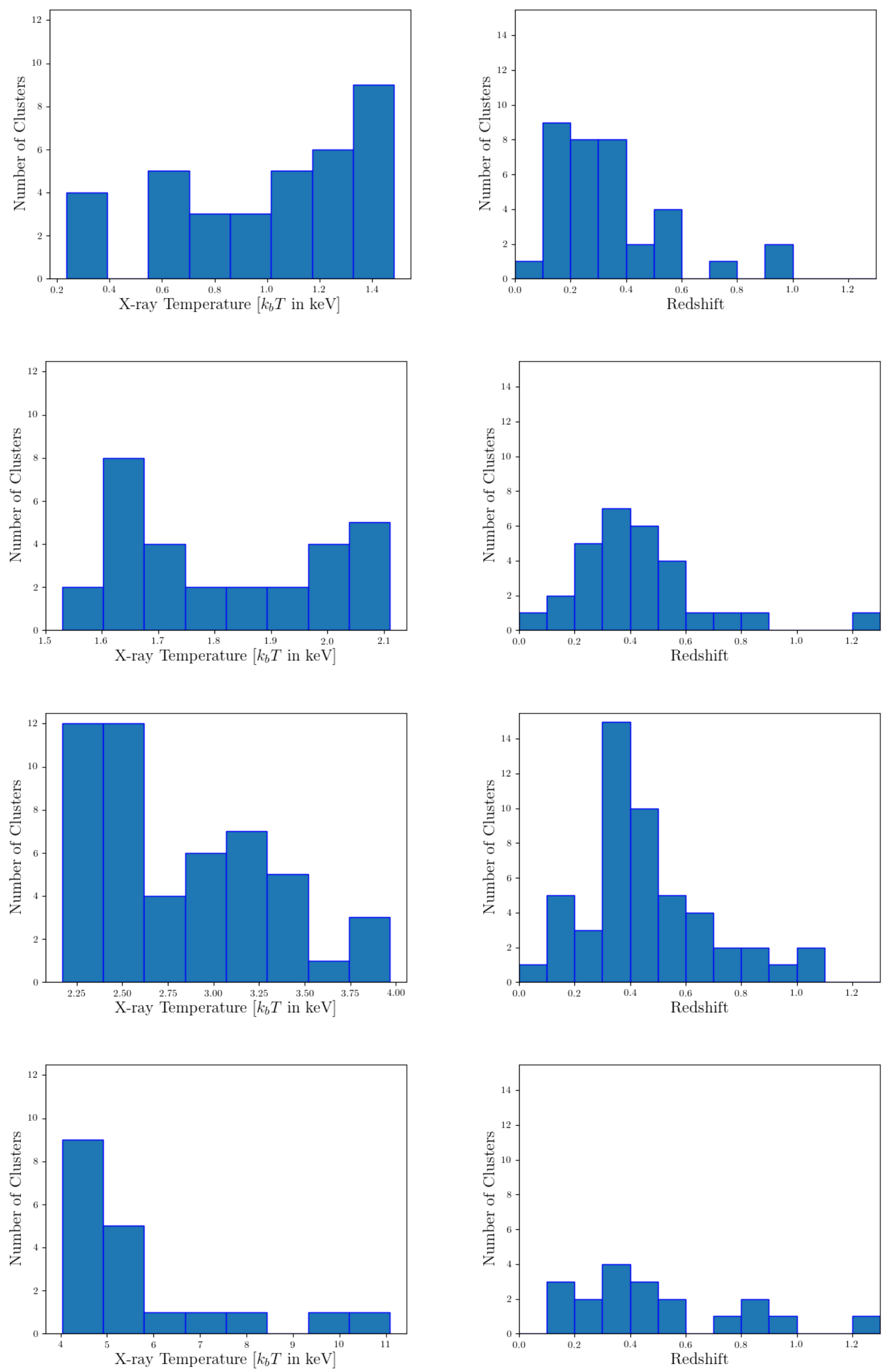

Figure 3.3 Temperature and redshift distributions of our four cluster bins, in order of increasing temperature from top to bottom.

Table 3.6. Properties of the stacked T_x bins. Column 1 names each bin, for ease of referral henceforth. Column 2 gives the size of each bin, and columns 3 and 4 give the lowest and highest temperatures in each bin.

Bin Name	Number of Clusters	Lowest $T_x[keV]$	Highest $T_x[keV]$
bin0	35	.235	1.48
bin1	29	1.53	2.11
bin2	50	2.17	3.97
bin3	19	4.03	11.1

Many recent cluster mass-observable-relation studies have stacked their halo samples not only by the observable, but also by redshift. However, these studies usually use thousands of clusters, allowing them to divide the samples into finer bins (eg. Melchior et al. (2017), Pereira et al. (2017)). This makes it simpler to model the expected $\Delta\Sigma$, as one need not worry about the effects of lensing over a variety of redshifts.

Our sample consists of only 133 clusters, which is barely enough to divide into four bins. Lower numbers of clusters per bin would lead to an inability to distinguish the WL signal from noise. Due to this, we only bin the clusters by X-ray temperature. As shown in Figure 3.3, each bin spans a wide range of redshifts—we must account for this, both when measuring the stacked $\Delta\Sigma$ signal (see Section 3.4) and when theoretically modeling it (see Section 3.5).

3.4 Measuring the Stacked Lensing Signal

We measure the stacked lensing signal, given by Eqn. 3.16, in radial bins (Rs) centered at the X-ray barycenter of the clusters:

$$\Delta\Sigma(R) = \frac{\sum_{i\in R} \Sigma^i_{crit} \dfrac{w^i}{{\Sigma^i_{crit}}^2} e^i_t}{\sum_{i\in R} \dfrac{w^i}{{\Sigma^i_{crit}}^2}(1+m^i)} \tag{3.17}$$

As we are stacking clusters only by T_x, we need to account for the wide range

Table 3.7. Details of radial bins for each stack. Column 1 is the stack id, and column 2 gives the width of each radial bin in that stack. Column 3 gives the center of the first radial bin (if this is shorter than half the bin width, then the first bin stretches from 0 to half the bin width beyond this value), and column 4 gives the number of radial bins used.

Temperature Bin Name	Stepsize [Mpc]	Center of First Radial Bin [Mpc]	Number of Radial Bins
bin0	.15	.05	8
bin1	.25	.1875	6
bin2	.3	.075	7
bin3	.4	.6	7

of redshifts in each temperature bin. A cluster at higher z covers a smaller part of the sky, making it seem as if the amplitude of its $\Delta\Sigma(R)$ drops off more sharply in celestial coordinates. To correct for this, we convert the separation between each background galaxy and its corresponding lens from sky coordinates into megaparsecs (Mpc).

We measure the signal for each stack out to a high enough radius R_{max} such that $R_{max} > R_{200max}$, where R_{200max} is the boundary of the cluster in the stack with the largest R_{200} (in Mpc). This ascertains that we capture data from the full range of each cluster's mass profile. To this end, we measure R_{200} for each cluster using a $R_{200} - T_x$ relation provided by Table 2 of Arnaud et al. (2005). The size of the radial bins varies for each temperature bin, as higher-T_x clusters will span a much larger area. We attempt various radial bin widths for each stack, and settle on the narrowest bins that still smooth out the lensing signals enough to be prominent relative to noise. This maximizes the number of data points we can fit to, while maintaining a usable signal to noise ratio. Table 3.7 shows details of the radial binning for each stack.

At one point in our analysis, we attempted to scale the radial bins by R_{200} in an effort to account for the wide range of temperatures in each T_x bin. A cluster of lower T_x covers a smaller part of the sky, making the amplitude of its $g_t(r)$ drop off more sharply in celestial coordinates. To correct for this, we scaled the position of each background galaxy by its corresponding cluster's R_{200}. However, this correction depends greatly on the accuracy of the $R_{200} - T_x$ scaling relation used, which can directly affect the spread of the resulting $\Delta\Sigma$ profiles and the corresponding measured masses. For instance, overestimating R_{200} "squeezes" the x-axis (radius, in terms of R_{200}), causing individual data points of the lensing signal to be located closer to the y-axis than they should be. This makes it seem as though the $\Delta\Sigma$ signal relative to radius, especially near the cluster center, is higher than it actually is. We eventually found that this method was indeed biasing our results, causing us to measure cluster masses that were much higher than known cluster populations, and decided to avoid the issue by only scaling galaxy positions to account for different redshifts, as detailed above.

3.4.1 Galaxy Selection

Of the galaxies that fall within each radial bin, we must choose which ones to include in our lensing signal. This consists of two types of cuts: removing galaxies that do not fulfill the shape catalog quality requirements, and choosing only galaxies that are behind the cluster.

Shape Catalog Cuts

We use galaxy shapes from the Im3shape r-band galaxy catalogs described in Chapter II, and so must apply the quality cuts recommended for this pipeline in order to avoid questionable objects or ellipticities. More details and reasoning behind these selection criteria can be found in Section 9.1 of Jarvis et al. (2016).

We first require that both error_flag == 0 and info_flag == 0. error_flag tags objects for reasons such as: the shape pipeline failed to converge; the object is too large; the object is too faint; etc. info_flag is more conservative, and removes objects that are: too small; flagged by the object detection software SExtractor; in parts of the sky for which we cannot measure photometry properly; etc. Further details about these flags can be found in Appendix B of Jarvis et al. (2016). We also remove any galaxies for which noise-bias calibrations were inconclusive (returned NAN).

Im3shape also recommends the following cuts, which we use:

- $(S/N)_w > 15$
- $R_{gp}/R_p > 1.2$

$(S/N)_w$ is the galaxy's signal-to-noise ratio, and R_{gp}/R_p is the ratio of a galaxy's observed size to the size of the observed point spread function (see Section 2.1.1 for more details). We also require that the magnitude of the galaxy through the r-filter be less than 23, removing dim objects for which we may not have reliable photometry. We test the robustness of our choices by varying galaxy selection cuts, detailed in Section 3.7.2.

Background Galaxy Selection

From the list of remaining galaxies, we use color-cuts to determine which sources are in the background of the cluster. "Color," denoted as C_{ab} is defined as the difference between the source's magnitudes in filters a and b. Though images of each object are available in four different filters, we choose to use only the r, i, and z filters:

$$\begin{aligned} C_{ri} &= \mathrm{mag}_r - \mathrm{mag}_i \\ C_{iz} &= \mathrm{mag}_i - \mathrm{mag}_z \end{aligned} \tag{3.18}$$

Galaxies in the background are further from us than the cluster, and thus will be "redder" than the cluster. The color of a cluster, as mentioned in Section 1.3.1, is taken to be the mean of the colors of the five brightest objects in its color-magnitude diagram. As the slope of the color-magnitude relation is negative, this ensures that anything redder than the cluster is almost definitely in the cluster's background. We require the color of a source galaxy, C^s, to be redder than the color of its corresponding lens, C^l:

$$\begin{aligned} C^s_{ri} &> C^l_{ri} + .05 \\ C^s_{iz} &> C^l_{iz} + .05 \end{aligned} \tag{3.19}$$

where the .05 serves as a buffer to further prevent contamination of the lensing signal by cluster galaxies. While this buffer does remove a number of definite background galaxies from our sample, our aim is purity rather than completion. Missing background galaxies may cause the final lensing profile to have a lower signal-to-noise ratio, but cluster galaxy contamination would dampen the lensing profile itself. Our ri colorcut is visually represented in Figure 3.4. Additionally, we require that back-

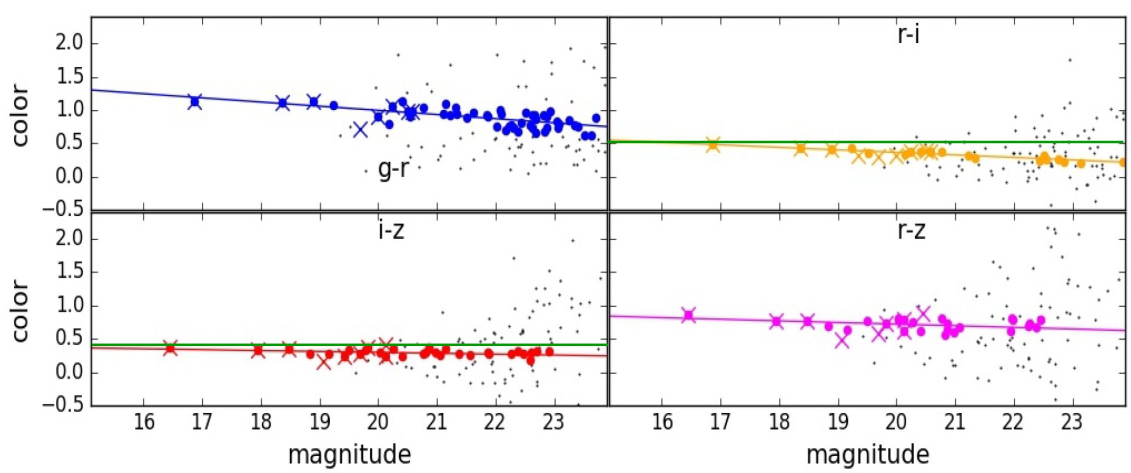

Figure 3.4 Color-magnitude diagrams of a cluster, overlaid with colorcuts. Colored points are cluster member galaxies, while black points are all other galaxies in a 3 arcmin × 3 arcmin cutout around the cluster center. The green lines show our cutoffs for background galaxies. Only galaxies above (redder than) the green lines in both $r - i$ and $i - z$ are included in our $\Delta\Sigma$ calculations.

ground galaxy redshifts be greater—"redder"—than the lens redshifts. This is a requirement of the mathematics of lensing: D_{ls} is undefined for sources with lower redshifts than their lenses, making us unable to measure Σ_{crit} (and thus $\Delta\Sigma$) for such objects. Of course, mathematical concerns aside, it would be unwise to include sources with lower redshifts anyways, as they are supposed to be in front of the cluster.

3.4.2 $\Delta\Sigma$ Errors

Using the above cuts, we finalize the set of background galaxies and measure the stacked $\Delta\Sigma$ in each radial bin R in accordance with Equation 3.17. The next step is to measure the uncertainties on the measured signal.

Statistical errors are found using non-parametric bootstrap sampling with replacement, as described by Efron (1982). From a radial bin with N background galaxies, we randomly choose a galaxy N times, allowing individual galaxies to be chosen multiple times or not at all, and compute the $\Delta\Sigma$ for this chosen set. We repeat this process 100 times and take the standard deviation of the resulting $\Delta\Sigma$ values as the error for each bin, $\sigma_{\Delta\Sigma}(R)$.

We test a few variations of this bootstrap sampling. In one method, we choose clusters rather than galaxies - that is, for a temperature bin with X clusters, for each radial bin, we randomly choose X clusters with replacement and calculate $\Delta\Sigma$ using only the background galaxies of the chosen clusters, and repeat the process for each radial bin 100 times. This shows no discernible difference from the original (galaxy) method. In other variations, we repeat the galaxy- and cluster-replacement methods 500 times for each radial bin. These show no discernible differences from the calculations with 100 runs, showing us that 100 repetitions is enough to sample the set of background galaxies in each radial bin. The results of these error estimations on the lensing profile of a subsample of our clusters is shown in Figure 3.5. We choose the initial method (replacing galaxies, repeating 100 times) to estimate the errors that we use in the rest of our analysis.

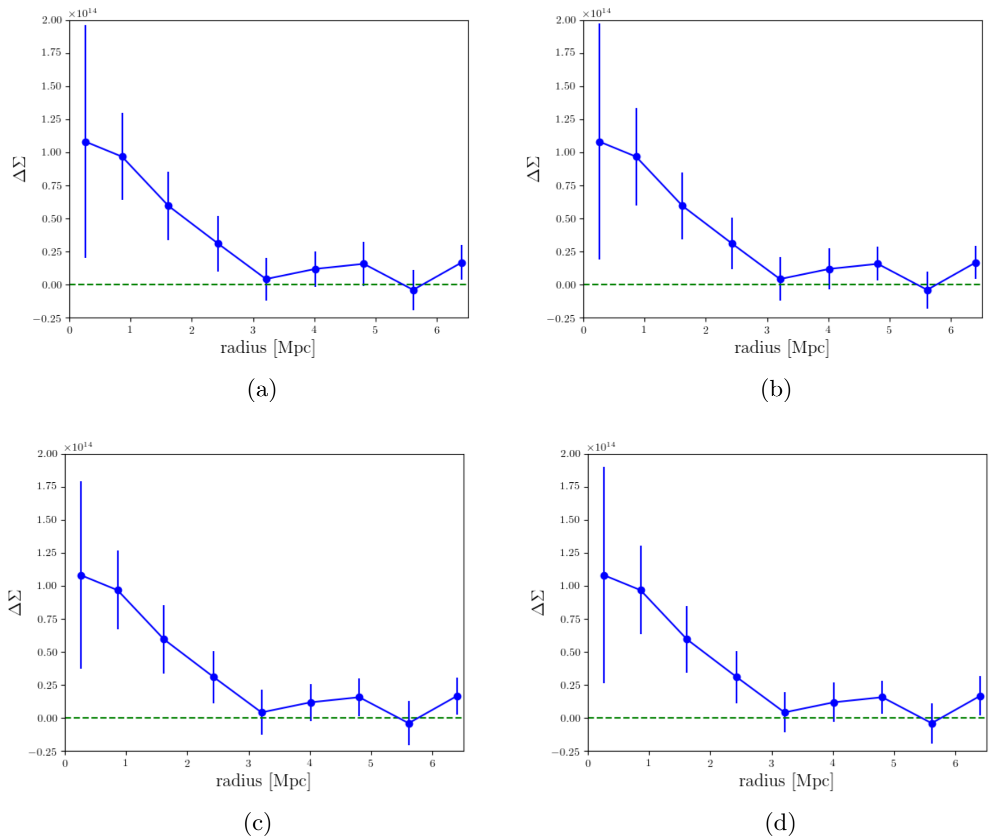

Figure 3.5 Comparison between variations in non-parametric bootstrap sampling for errors. These plots show the lensing signal and errors on a subsample of our dataset. This subsample is further described in Section 3.7.2 (a),(b) Errors by choosing galaxies from each bin with replacement, repeated 100 and 500 times, respectively. (c),(d) Errors by choosing clusters from each bin with replacement, repeated 100 and 500 times, respectively.

3.5 Modeling the Stacked Lensing Profile

Once we have measured the stacked lensing signals and associated errors, the next step is to generate model $\Delta\Sigma$ profiles. As described in Section 3.1, the radial mass distribution of a galaxy cluster can be modeled by the Navarro-Frenk-White (NFW) density profile, which can be parametrized by mass M_{200} and concentration c. The lensing signal around an NFW halo can then be calculated analytically in terms of these parameters.

We calculate the $\Delta\Sigma$ we expect to see for various models, and use a maximum likelihood method to match our observed $\Delta\Sigma$ to a best-fit mass for each T_x bin. Ideally, each model would consist of an independent M_{200} and c, but in practice, the data is not sufficient to simultaneously fit for both mass and concentration. For this work, we only fit to find an optimum M_{200} for each bin. c for each model NFW halo is calculated using the $M_{200} - c$ relation given by Merten et al. (2015).

To generate theoretical $\Delta\Sigma$ profiles, we use the GalSim 1.3.0 suite, which simulates NFW halos for given values of M_{200}, z_{lens}, and c, and can calculate the reduced shear for an object with redshift z_{source} at a radius r from the cluster center (see Rowe et al. (2015) for more details about GalSim).

3.5.1 Modeling $\Delta\Sigma$ for a Cluster Stack with a Wide z Range and Uneven Data

As shear is not redshift-independent, using it as a lensing estimator is complicated when working with a stack of clusters with a wide redshift range. Clusters with the same mass but varying zs will generate varying shear, making it hard to fit them to any one model profile. For this reason, $\Delta\Sigma$, which is redshift-independent, is traditionally used to model stacked weak lensing signals (eg. Melchior et al. (2017), Pereira et al. (2017)). Usually, a single $\Delta\Sigma$ profile is generated for each model M_{200}, and the model that best fits the observed stacked profile is chosen. However, this assumes a uniform dataset, where each cluster contributes evenly to the stacked lensing signal - i.e., each cluster contributes about the same number of background galaxies.

Unfortunately, DES SV data quality is highly patchy. Equipment malfunctions in the early days of DES caused data quality issues in several of our images, in some cases resulting in unusable PSFs across whole tilings. Many galaxies in these areas of sky were removed by lensing quality cuts. The resulting effect is that several clusters contribute very few background galaxies to the stacked lensing signal, whereas others

- in areas of sky with better data quality - sit in front of dense high-quality galaxy fields. Figures 3.6 and 3.7 show the effect of this on our effective temperature and redshift distributions. Figure 3.6 is a copy of Figure 3.3, showing the T_x and z distribution of each cluster stack. Figure 3.7 shows the same distributions, but weights each cluster by the number of background galaxies it contributes. This effectively gives us the total number of background galaxies in each temperature or redshift range for each stack. From these figures, we can clearly see that clusters contribute background galaxies inhomogenously.

To account for these inhomogeneities, we develop a $\Delta\Sigma$ modeling method that recreates our observations by using multiple $\Delta\Sigma$ profiles for each model $M_{200,model}$, rather than relying on one sole theoretical lensing signal. For each $M_{200,model}$, we use GalSim to generate several shear profiles, each calculating the effect of some part of our observed source and lens z distributions. We convert these shears to $\Delta\Sigma$ profiles, weighting by Σ_{crit}^{-2} to mimic data. These weighted model $\Delta\Sigma$ signals are then combined to generate our final $\Delta\Sigma_{model}$ for each mass. We do this using two different methods, and show that results for both are consistent with each other.

This method gives us the ability to measure cluster masses using any dataset, without needing to exclude clusters for low data quality. This is a great advantage for weak lensing studies, where the signal is only as strong as the abundance of background galaxies, as it allows us to make use of every bit of data available.

Modeling with Background z Distributions Per Cluster

The first method builds up the $\Delta\Sigma_{model}$ profile for each T_x bin using the separate z distribution of background galaxies for each cluster in that bin. For every $M_{200,model}$, we generate as many NFW profiles as there are clusters i in the bin, each with z equal to the redshift of one of the real clusters and denoted as $M_{200,model,i}$. Then,

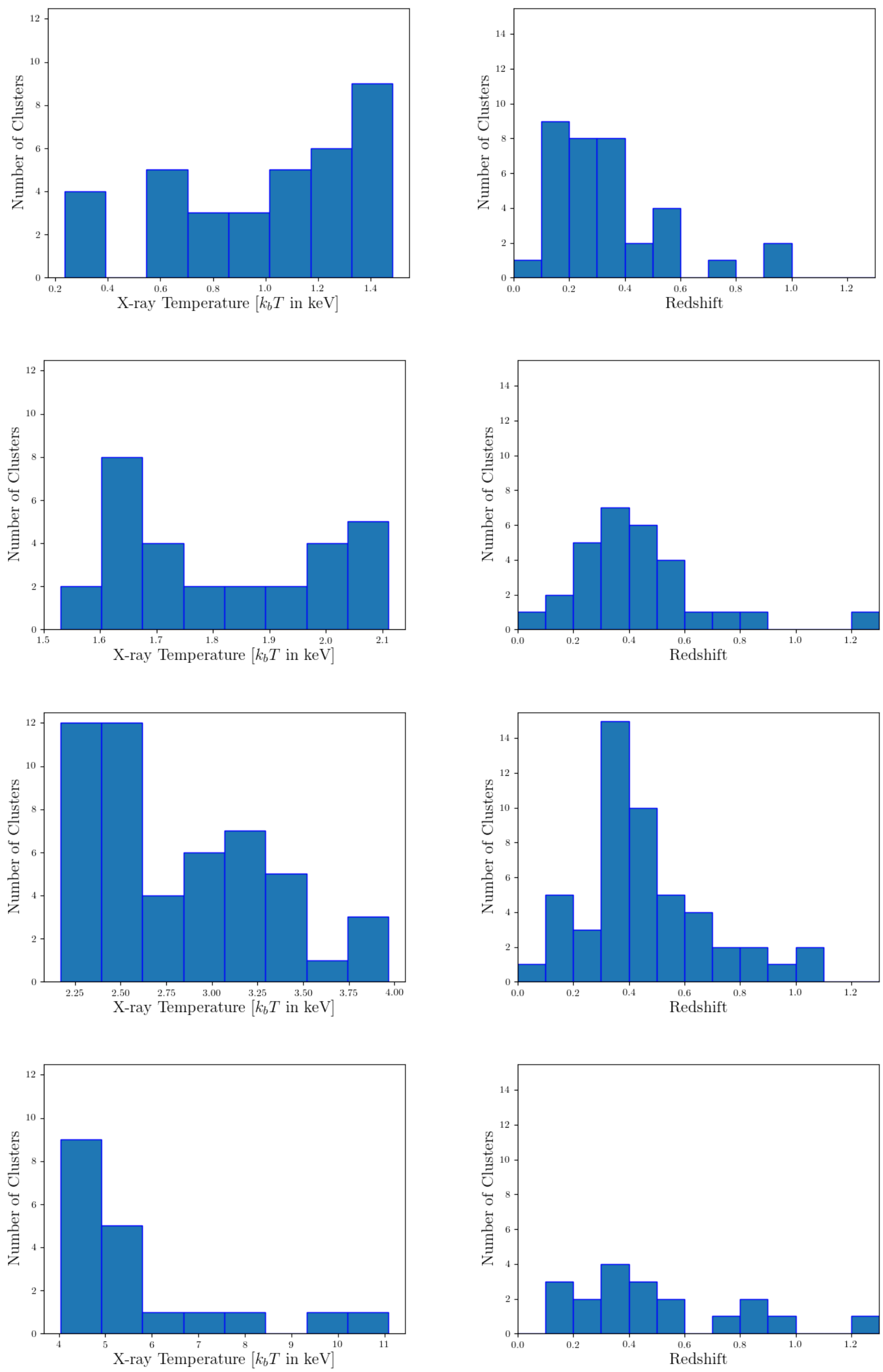

Figure 3.6 Temperature and redshift distributions of our four cluster bins, unweighted, in order of increasing temperature from top to bottom, with each cluster counted once. Same as Figure **??**, reproduced here to allow easy comparison with Figure 3.7.

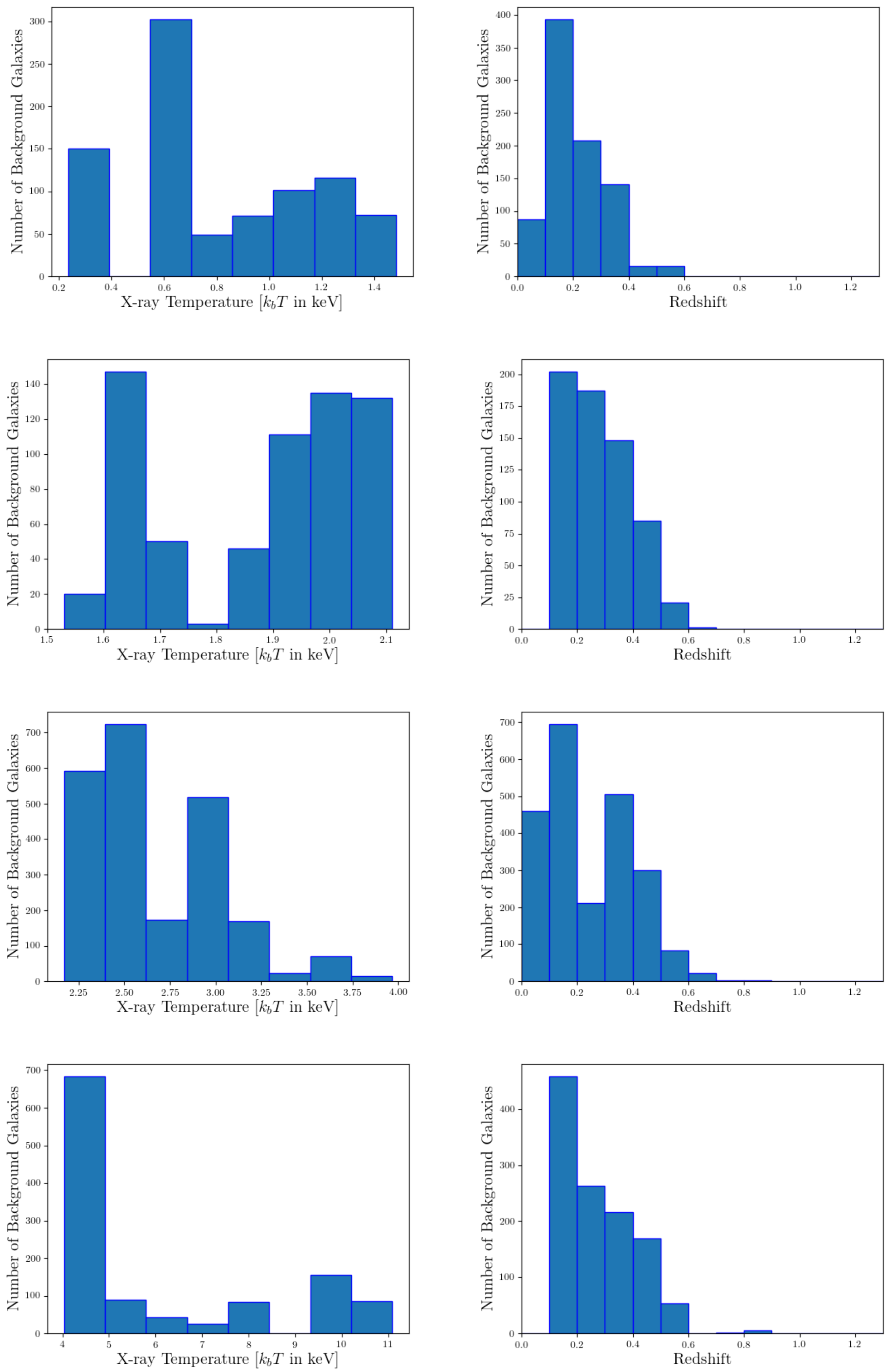

Figure 3.7 Temperature and redshift distributions of our four cluster bins, weighted, in order of increasing temperature from top to bottom, with each cluster counted once for each of its background galaxies - effectively gives the number of background galaxies in each T_x-bin for each range in lens properties.

we bin the redshifts of background sources for each cluster separately into 10 z_{source} bins per cluster. The mean z of each of these bins is used to calculate the reduced shear $g_{t,model,i,z}$ around the corresponding $M_{200,model,i}$. After converting these shears to $\Delta\Sigma_{model,i,z}$ profiles, we take the average of all profiles - that is, the profiles for each z-bin for each cluster i - weighted by the number of sources in each z-bin, $N(i,z)$, to get

$$\Delta\Sigma_{model} = \frac{\sum_{i,z} \Sigma_{crit,i,z} g_{t,model,i,z} \left(\frac{N(i,z)}{\Sigma^2_{crit,i,z}} \right)}{\sum_{i,z} \frac{N(i,z)}{\Sigma^2_{crit,i,z}}} \tag{3.20}$$

Modeling with Individual Source-Lens Pairs

As discussed above, the DES SV dataset is not complete, excluding a large fraction of sources due to quality issues. This not only varies the number of background galaxies per cluster, but also causes the number density of background galaxies, $n(i,r)$, to fluctuate across radial bins for any given cluster.

While the above method should model the observed $\Delta\Sigma$ well given ideal conditions, it depends on a source redshift distribution for each cluster that is independent of radial bin. Given the homogenous and isotropic nature of the universe, this should not be a concern as long as there is ample data. However, with a dataset where $n(i,r)$ varies to such a degree, where some bins contain only a handful of background galaxies, the source-z distribution may vary with radial bin. This means that a cluster's presence can potentially be felt differently in each radial bin of the observed lensing signal, and choosing a single source-z distribution per cluster can lead to incorrect modeling of each cluster's contribution to each $\Delta\Sigma(r)$.

To ensure this is not the case, we build up the model $\Delta\Sigma$ piece-by-piece, recreating the signal for each individual observed source-lens pair. For each model of mass

$M_{200,model}$, we again generate separate NFW profiles for each cluster in our dataset, assigning the respective cluster's redshift to its corresponding model profile. For each radial bin, we average the $\Delta\Sigma$ signals between every cluster and each of its background galaxies j in that bin to get

$$\Delta\Sigma_{model}(r) = \frac{\sum_{i,j\in r} \Sigma_{crit,i,j}\, g_{t,model,i,j} \left(\frac{1}{\Sigma^2_{crit,i,j}}\right)}{\sum_{i,j\in r} \frac{1}{\Sigma^2_{crit,i,j}}} \tag{3.21}$$

Figure 3.8 shows the best-fit stacked $\Delta\Sigma$ profile for a subset of our clusters, found using both methods. Note that this is not one of the T_x bins used in our final analysis. As testing between these modeling methods was conducted before the cluster sample was finalized, we show this comparison using an older sample on which we tested. Also due to the early nature of these tests, they were conducted while we were still scaling the radial bins by each cluster's R_{200} (see Section 3.4 for details). As both methods are scaled the same way, their results are comparable.

We find, to our surprise, that both methods give us extremely close results. This suggests that the spatial spread of our background galaxies is more even than we had anticipated. This also provides a robustness check for our methods - varying the method of modeling does not change the measured mass.

We choose the second method - modeling with individual source-lens pairs - for the rest of our analysis, as it has the ability to account for potential inhomogeneities in our background galaxy sample that may have arisen from the extra cluster fields added later.

3.6 Stacked Weak Lensing Masses

We find the best-fit stacked $M_{200,fit}$ of each T_x bin by maximizing the likelihood

$$L = e^{-\chi^2/2} \tag{3.22}$$

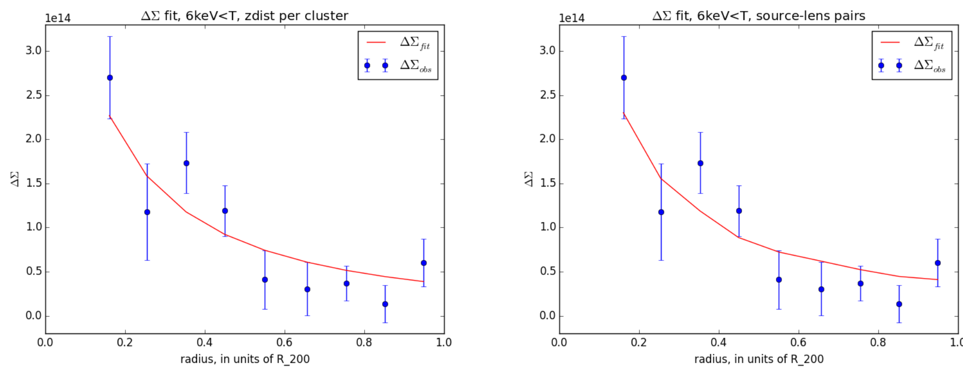

(a) (b)

Figure 3.8 Comparison between two types of modeling of theoretical $\Delta\Sigma$ profiles. (a) Best-fit $\Delta\Sigma$ profile measured using background-z distributions per cluster, overlaid with observed stacked $\Delta\Sigma$. (b) Best-fit $\Delta\Sigma$ profile measured using individual source-lens pairs, overlaid with observed stacked $\Delta\Sigma$.

$$\chi^2 = \sum_r \left(\frac{\Delta\Sigma_{model}(r) - \Delta\Sigma_{obs}(r)}{\sigma_{\Delta\Sigma}(r)} \right)^2 \tag{3.23}$$

and take the 1σ bounds of the likelihood curve to define the $M_{200,fit}$ uncertainties.

As noted in Section 3.4.2, our measurements of $\Delta\Sigma$ uncertainties through the bootstrap method are purely statistical. Possible systematic biases, which would come into play given a larger statistical dataset, can include

- halo modeling effects: our choice to model halos as NFW profiles, and to ignore the effects of the 2-halo term—small percent-level effects (Melchior et al. (2017))
- projection effects: possible nearby large structure interfering with lensing measurements—about a 2% effect (Melchior et al. (2017))
- $M-c$ relation effects: any biases resulting from our choice of mass-concentration relation—about $5-15\%$, but smaller when extending lensing signals out to at least cluster R_{200} (as we do) (Kettula et al. (2013))

We ignore systematic uncertainties as they are well overshadowed by our statistical uncertainties, courtesy of a relatively low number of background galaxies.

Cluster mass scaling relations are conventionally written in terms of M_{500}. We

Table 3.8. Best-fit M_{500} for each stack. Column 1 is the stack id, column 2 gives the best-fit mass, and columns 3 and 4 give the lower and upper bounds respectively on 1σ uncertainties.

Temperature Bin Name	Best-fit M_{500} $[10^{14}\mathrm{M}_\odot]$
bin0	$0.250^{+0.453}_{-0.211}$
bin1	$0.681^{+1.059}_{-0.569}$
bin2	$1.90^{+1.16}_{-0.92}$
bin3	$5.20^{+3.64}_{-2.70}$

convert $M_{200,fit}$ to $M_{500,fit}$ following the method outlined in Appendix C of Hu & Kravtsov (2003). We use the same method to convert the bounds of our $M_{200,fit}$ uncertainties. Table 3.8 shows our results.

Figure 3.9 shows the best-fit $\Delta\Sigma_{model}$, overlaid on $\Delta\Sigma_{obs}$, for each temperature bin, as well as the likelihood curves, with 1σ bounds marked.

3.7 Testing the Stacked WL Masses

In this section, we discuss several checks on the robustness of our measured masses. We first validate our analysis method and code by running on simulations and comparing to results from existing code. We then ascertain that our signals are truly due to lensing, and that they do not depend on our fiducial choices and background galaxy selection. Finally, we check for any contamination of the signal by cluster galaxies.

3.7.1 Analysis Pipeline Validation

Simulation Tests

To check the accuracy of our method of building up the model $\Delta\Sigma$ profiles using individual source-lens pairs, we run the same analysis on simulated data from the Buzzard v1.1 suite. Buzzard covers 10313 sq. deg. and contains 971 million galaxies "observed" in the DES filter bands, and out to DES depth. The simulation provides

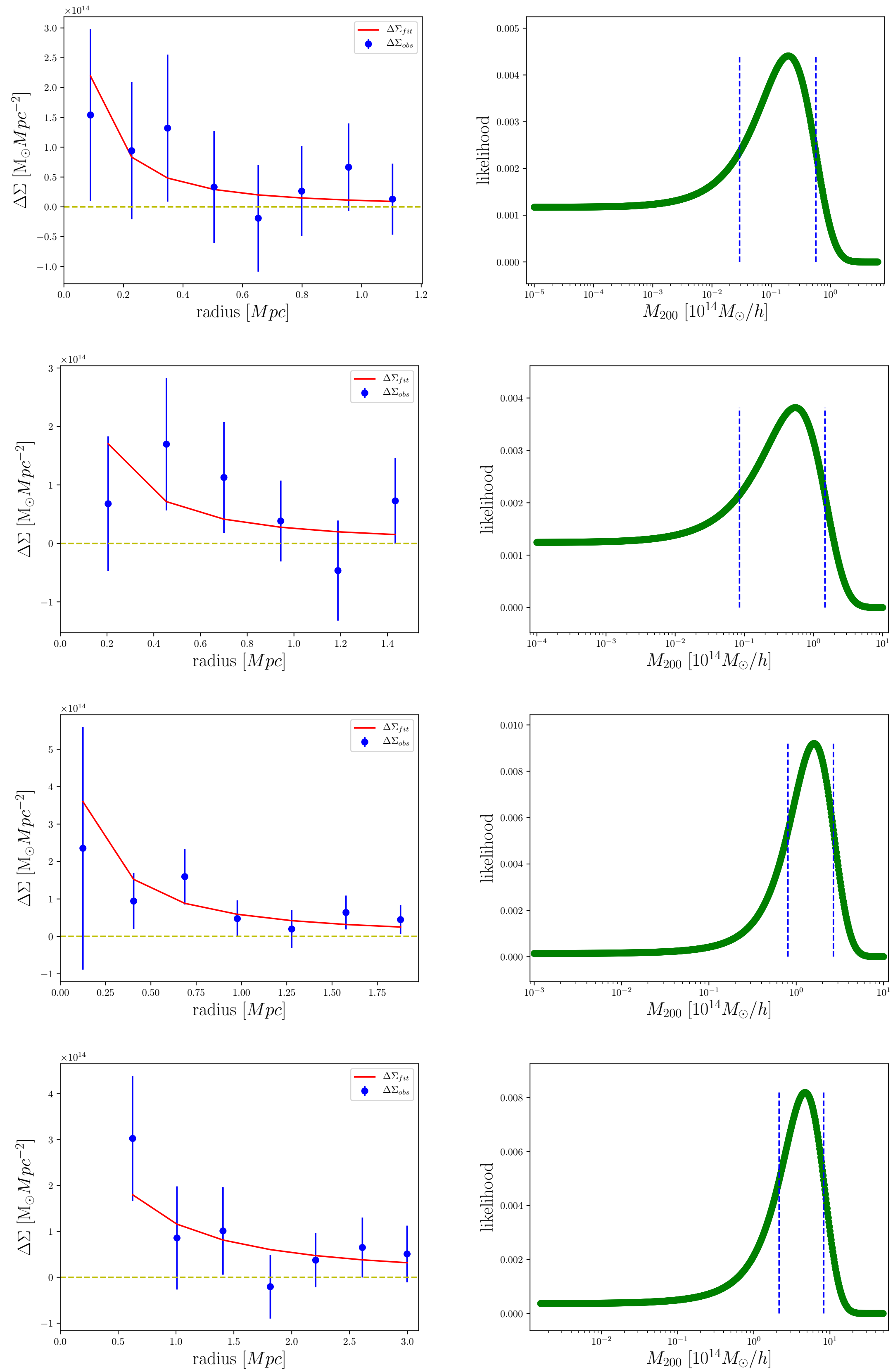

Figure 3.9 (left) Best-fit $\Delta\Sigma$ profiles, overlaid on the measured $\Delta\Sigma$ values, for each of our four T_x bins of data. (right) Likelihoods for our model masses for each bin, with 1σ uncertainties marked. Bins go from low to high T_x, from top to bottom.

a halo catalog with positions, redshifts, masses, and concentrations, among other properties. The galaxy catalog provides redshifts, magnitudes, and positions, comparable to the DES object catalog, and shears for each object are measured using ray-tracing. For further details about the Buzzard suite, see DeRose et al. (in prep.) and Wechsler et al. (in prep.).

We compile a simulated sample from the Buzzard halo catalog, choosing halos to match our real cluster sample. For each cluster in the DES-SV-XCS sample, we choose a halo of similar mass and redshift from Buzzard. To do this, we first need estimates of masses for each DES-SV-XCS cluster, for which we only have measurements of redshift and temperature. We use the $M_{500} - T_x$ relation from Vikhlinin et al. (2009a) to measure M_{500} masses for each cluster. As Buzzard provides M_{200} masses, we convert our estimated M_{500} values to M_{200} masses following the procedure in Appendix C of Hu & Kravtsov (2003), assuming cluster concentrations to be 4. For each cluster, we then pick a random halo from Buzzard whose M_{200} lies within 10% of our estimated cluster mass, and whose redshift lies within .05 of our cluster's observed redshift, compiling our simulated sample set.

We run the $\Delta\Sigma$ and mass measurement pipeline on a subset of the simulated halo sample. Note that this set does not correspond directly to one of the T_x bins used in our final analysis. As testing was conducted before the cluster sample was finalized, we show this comparison using a sample whose properties match one of our older T_x bins. We find the best-fit $\Delta\Sigma$ profile to be consistent with the theoretical profile calculated using "true" halo masses, as shown in Figure 3.10, validating our $\Delta\Sigma$ modeling methodology.

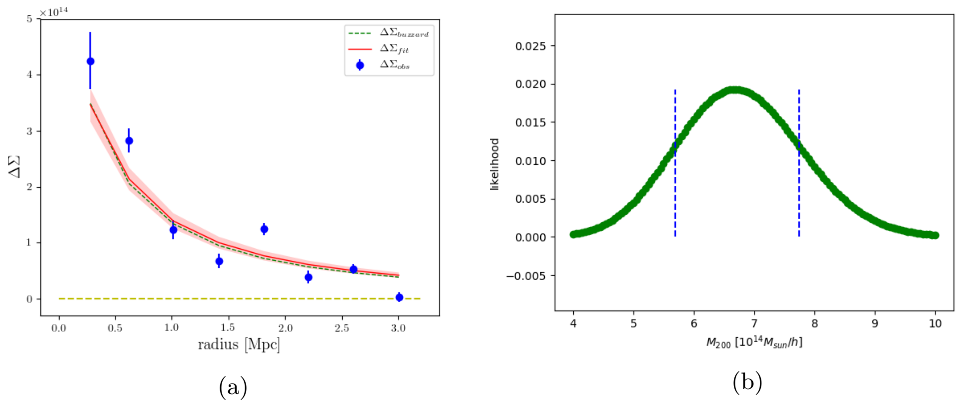

Figure 3.10 Analysis tested on simulated sample from Buzzard v1.1. (left) Best-fit $\Delta\Sigma$ with 1σ uncertainties around a set of simulated halos, overlaid on the "true" profile. (right) Likelihood for our model masses for the simulated sample, with 1σ uncertainties marked. Recovering the true stacked mass validates our $\Delta\Sigma$ modeling methodology.

Comparison to xshear

There exist several publicly-available libraries of code that measure the lensing signal around a given point on the sky. Given lists of lenses (positions, redshifts) and sources (positions, redshifts, ellipticities), these codes output the final shear or $\Delta\Sigma$ in chosen radial bins. However, they do not store information on individual source-lens pairs. As this information is crucial to our $\Delta\Sigma$ modeling technique, we write our own code to measure the lensing signal rather than using a ready-made suite.

In order to validate our code and weed out any possible bugs or miscalculations, we test it against an established library. One such existing shear-measurement repository is XSHEAR[2], which has been used in several DES analyses. We use both our code and XSHEAR to measure $\Delta\Sigma$ profiles around a set of simulated clusters from the Buzzard v1.1 suite. Note that, due to the early nature of this test, it was conducted while we were still scaling the radial bins by each cluster's R_{200} (see Section 3.4 for details). As runs with both codes are scaled the same way, their results are comparable.

[2]https://github.com/esheldon/xshear

Figure 3.11 shows the results - as expected, both codes match perfectly.

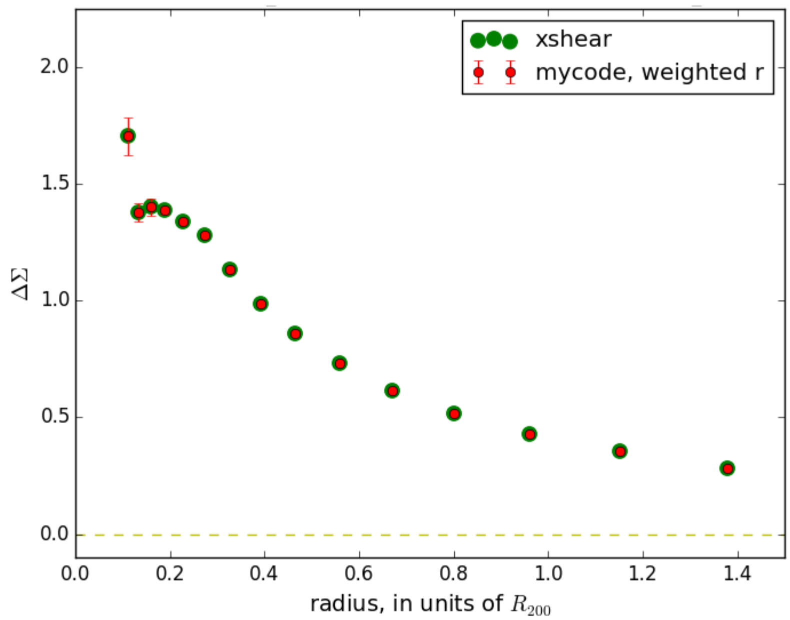

Figure 3.11 Code check with XSHEAR. $\Delta\Sigma$ around a set of simulated halos from Buzzard v1.1, measured by both our code and the XSHEAR suite, used to validate our code.

3.7.2 Shear Profile Tests

We perform several checks to ascertain the robustness of the measured $\Delta\Sigma$ profiles. These checks test shape measurements, background galaxy selection, and cluster selection.

These checks look at the lensing profile of the ensemble of clusters under varying conditions, extending out to $6Mpc$. Our shape catalogs for each cluster extend out to $40'$, which does not necessarily cover the $6Mpc$ range. Furthermore, due to inhomogeneities in SV data quality, several portions of the footprint have been masked out and excluded from our catalogs. While we take these inhomogeneities into account for our primary analysis during modeling for mass calibration (see Section 3.5.1), these checks only run on the observed lensing signal, which has not been corrected for this. Thus, these checks are only relevant for clusters where the number density of sources is uniform throughout the area used.

We run these checks on the subset of 67 clusters whose source catalogs contain a uniform distribution of galaxies within the area bounded by $6Mpc$ from the cluster center. As discussed in Section 2.2, the quality of used shapes is consistent across our various areas of sky, allowing us to extrapolate the results from this subset to the whole sample.

All checks, described below, are shown in Figure 3.12.

Shape Measurement Checks

We test our measured ellipticities to ensure that the observed $\Delta\Sigma$ is truly a result of lensing. Lensing affects the tangential component of the ellipticities of background galaxies. It does not, however, affect the perpendicular component, given by

$$e_\times = (e_1 - c_1)sin(2\phi) + (e_2 - c_2)cos(2\phi) \tag{3.24}$$

As this perpendicular ellipticity is independent of lensing, the corresponding net $g_\times$ and $\Delta\Sigma_\times$ should be consistent with zero. The upper left plot shows $\Delta\Sigma_\times$, with the tangential signal $\Delta\Sigma_t$ for comparison.

As has been the case through this paper, in the following sections, we will continue to use $\Delta\Sigma$ to represent the tangential background lensing signal, $\Delta\Sigma_t$.

Photo-z Pipeline Check

We ensure that our results are not biased by our choice of source redshift measurement techniques. Our analysis uses photo-z measurements from the DES TPZ pipeline, assigning each source galaxy the mean photo-z from its redshift probability distribution. The upper right plot shows that our measurements are consistent with results using photo-zs from the DESDM Neural Network pipeline instead.

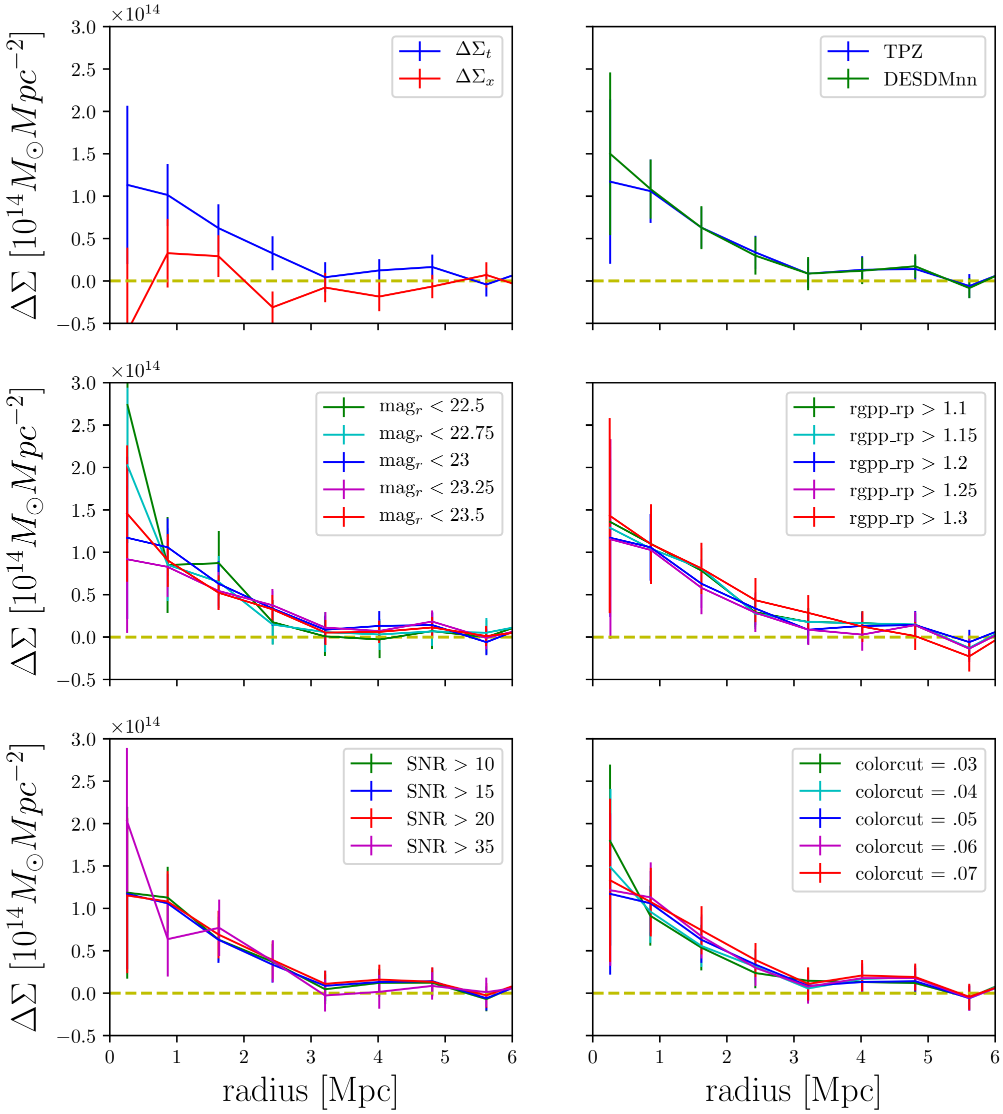

Figure 3.12 Robustness checks on our lensing signal, performed on a subset of 67 clusters. The upper left shows the perpendicular $\Delta\Sigma$ check. Upper right shows comparisons using two photo-z catalogs. Middle left varies the magnitude cut through the r filter, middle right varies the cut on *mean_rgpp_rp*, lower left varies the SNR cut, and lower right varies the colorcut for background galaxy selection.

Background Galaxy Selection Checks

We perform several checks to ensure that our results are not dependent on the quality cuts involved in our selection of background galaxies.

The middle plots show $\Delta\Sigma$ measured with varying magnitude and rgpp_rp cuts, each consistent with the signal from our chosen cuts, $mag\_r < 23$ and $rgpp\_rp > 1.2$. The lower left plot shows the results for cuts by signal-to-noise ratio, for which our chosen cut is $(S/N)_w > 15$.

To ensure that our color-cuts are not allowing contamination of the background sample by cluster galaxies, we measure $\Delta\Sigma$ while varying the buffer between lens and background source colors. The lower right plot shows these $\Delta\Sigma$ profiles to be consistent with each other.

3.7.3 Cluster Contamination Check

Cluster galaxies sneaking into our "background" sample, lacking any overall tangential alignment, would dampen the lensing signal. This is often a concern in cluster lensing studies, especially ones that use redshift cuts to choose background galaxies, and must be corrected (eg. Melchior et al. (2017)).

However, when using colorcuts, the background galaxy selection is usually conservative enough to avoid including cluster galaxies. As discussed in Section 3.4.1 and shown in Figure 3.4, our cuts look to be well behind the clusters. Additionally, Medezinski et al. (2018) recently show that using colorcuts leads to lensing measurements unaffected by cluster contamination.

Regardless, we still check to ascertain that the measured $\Delta\Sigma$ profiles are not affected by cluster contamination. We compare the redshift distributions of sources near and far from the cluster centers. Cluster members have lower redshifts than background galaxies, and would cause the background z distribution to be skewed towards lower redshifts near the cluster centers. Assuming there is no cluster member contamination, the redshift distributions should be about the same.

As the potential for contamination primarily exists near the cluster center, and fades away as we reach cluster boundaries, we must check clusters of different sizes for contamination at different radii. In order to simplify this, we scale the radial bins for each cluster by its R_{200} (as described in Section 3.4), and stack the resulting bins. Figure 3.13 shows the background z distributions for four radial bins to be consistent with each other.

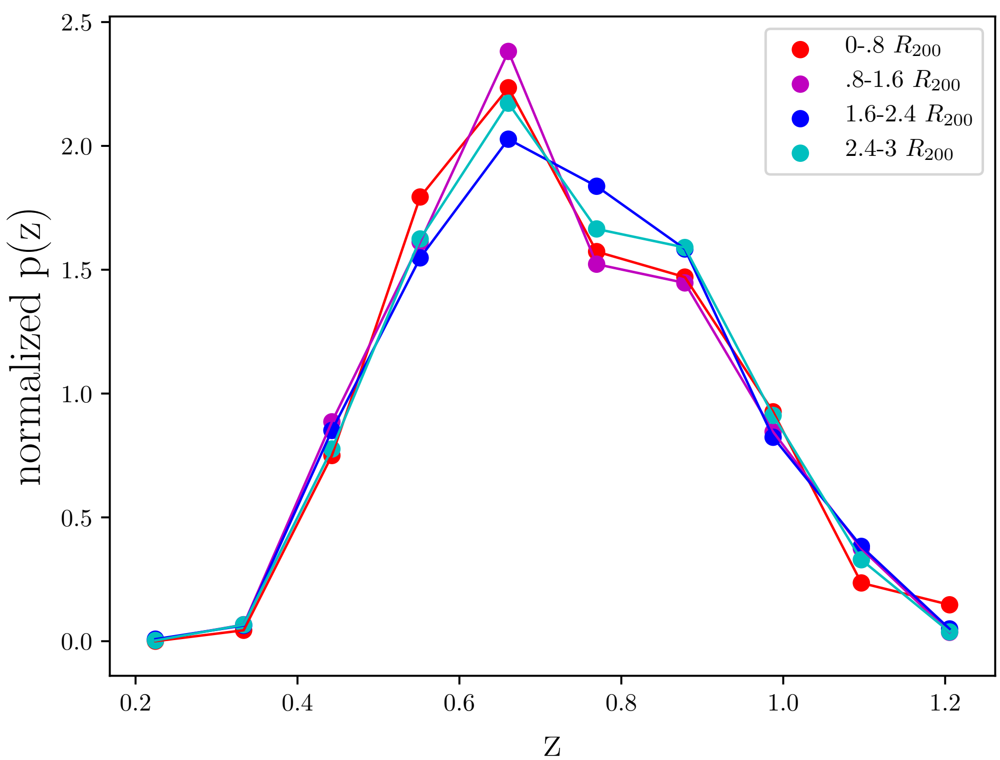

Figure 3.13 Testing for contamination of the $\Delta\Sigma$ signal by cluster members. Figure shows background galaxy redshift distributions in four radial bins. The agreement between the distributions rules out concern over cluster contamination of the $\Delta\Sigma$ signal.

3.8 Discussion and Summary

In this chapter, we measure stacked weak-lensing masses for 133 clusters in the DES-SV-XCS cluster sample. We sort the clusters into four temperature bins, described in Table 3.6 and measure $\Delta\Sigma$ around each stack.

We then model theoretical $\Delta\Sigma$ profiles for an array of masses, using two techniques to account for inhomogeneities in our data, and find best-fit masses for each stack. Our technique using individual source-lens pairs to build up theoretical $\Delta\Sigma$ profiles allows us to measure masses for clusters with extremely varied sets of available background galaxies. To facilitate further studies, we make the code for our analysis, which we have named LensStack, available for public use (see Appendix A for details).

To ensure the validity of our measurements, we test both our analysis methodology and our code, run checks on our optical measurements, and conduct several tests to ensure that our selection of background galaxies has not biased our results. Final masses for each cluster stack are given in Table 3.8.

There are several avenues for this work to follow in the future. Possibilities arise both from hopes of more data and from the ability we now have to probe imperfect datasets.

First, the uncertainties in our resulting masses are quite high, due in part to the low number of background galaxies in each bin, which lead to noisy $\Delta\Sigma$ profiles. This issue can be attributed to the fact that several of our clusters contribute very few background galaxies (some contribute hundreds, some dozens, others only a handful, and others none at all) due to issues with SV data quality. The areas around two clusters are shown in Figure 3.8, where each point is a galaxy (including foreground, cluster, and background galaxies). For one cluster, we see a dense field, representative of good DES data. For the other, we see only a few galaxies—the other objects in the field were likely left out due to SV data quality cuts. We eagerly anticipate

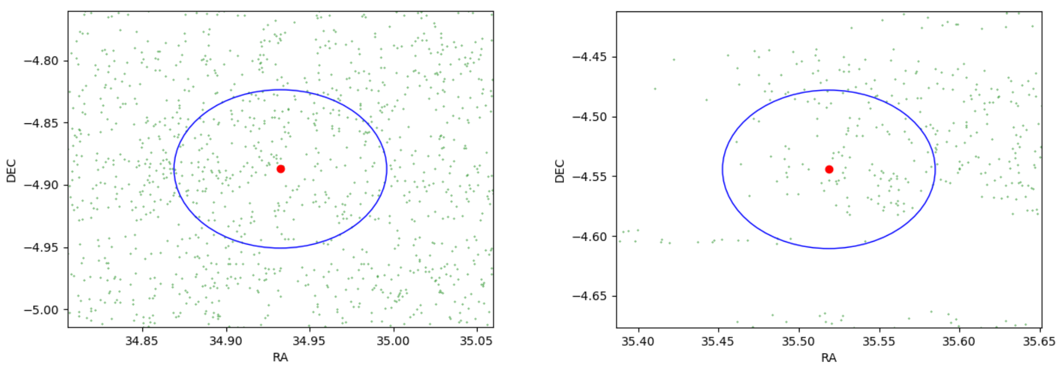

(a) (b)

Figure 3.14 Sparse and dense galaxy fields—galaxy catalogs around two clusters at comparable redshifts and temperatures. Blue circles mark R_{200}. (a) lies in a field with a dense, mostly uniform galaxy catalog, while (b), just the next tiling over, lies in a much less homogeneously observed field due to SV data quality cuts.

upcoming DES Year 3 (Y3) data, where it is likely that most fields will resemble the denser area of Figure 3.8, providing far more background galaxies to work with and allowing narrower constraints on masses. Y3 shape catalogs will also undergo far stronger calibrations—Year 1 catalogs showed a $> 50\%$ decrease in shear calibration-related errors over SV (see Section 8 of Mcclintock et al. (submitted)), and Y3 is expected to improve upon that. Aside from IM3SHAPE, Y3 will also provide the DES METACALIBRATION shape catalog (Zuntz et al. (submitted)), allowing tests of mass-measurement robustness with different methods of shape measurement. With greater amounts of higher-quality shape data, Y3 looks promising for the measurement of stacked cluster masses with tighter uncertainties.

On the other hand, this work provides us with a method for analyzing datasets without regard for data uniformity. We can use the method presented to examine both types of fields shown in Figure 3.8. With this, we can examine clusters that reside in fields where optical data quality is extremely poor, or clusters that lie at the edges of our fields of view, without hindrance from asymmetries or inhomogeneities, either in any given cluster's background galaxy catalog or in the sample as a whole. We can also incorporate whatever data is available for high-z clusters, which are usually left out of analyses due to low background galaxy counts. For example, in their work on using weak lensing to constrain the scaling relation between mass and a CMB observable, Stern et al. (submitted) mention that they exclude high-z clusters due to low numbers of background galaxies—with this method, we would be able to incorporate information from those clusters into a stacked weak lensing analysis. This gives us an extremely powerful tool for weak lensing studies, where the signal is only as strong as the abundance of background galaxies, as it allows us to make use of every bit of data available.

CHAPTER IV

The Galaxy Cluster Mass-X-ray Temperature Scaling Relation

The scaling relation between galaxy cluster mass and X-ray temperature is instrumental both for cosmology studies using cluster abundances and for studying the properties of clusters themselves. The use of T_x as a mass proxy is limited by the precision to which we understand the scaling relation and associated errors.

Existing measurements of the $M - T_x$ relation indicate that hydrostatic bias may be affecting the accuracy of X-ray inferred cluster masses, especially in the low-mass regime (Kettula et al. (2013), Mahdavi et al. (2013)). Currently, the best datasets that have been used to measure this are based on heterogeneous X-ray and optical data, using 65 clusters (Kettula et al. (2013)). In this chapter, we probe the $M - T_x$ relation using a homogenous sample of 133 clusters, spanning a wide range of temperatures, giving us greater ability to explore this tension. While we do stack the cluster sample, effectively resulting in 4 data points—compared to Kettula's 65—we still incorporate information from a far larger sample with a wider temperature range, allowing us to probe further into the low-mass regime.

Figure 4.1, taken from Zhang et al. (2016), summarizes the current state of cluster mass-temperature scaling relations across a range of masses. This figure compares masses calculated using the $M - T_x$ relation from Kettula et al. (2013) with masses using several other scaling relations from literature. In each panel, masses using the Kettula relation are plotted along the x-axis, and masses using other relations are shown on the y-axis. The blue dotted lines mark y=x, and red marks the best-fit lines through the data points.

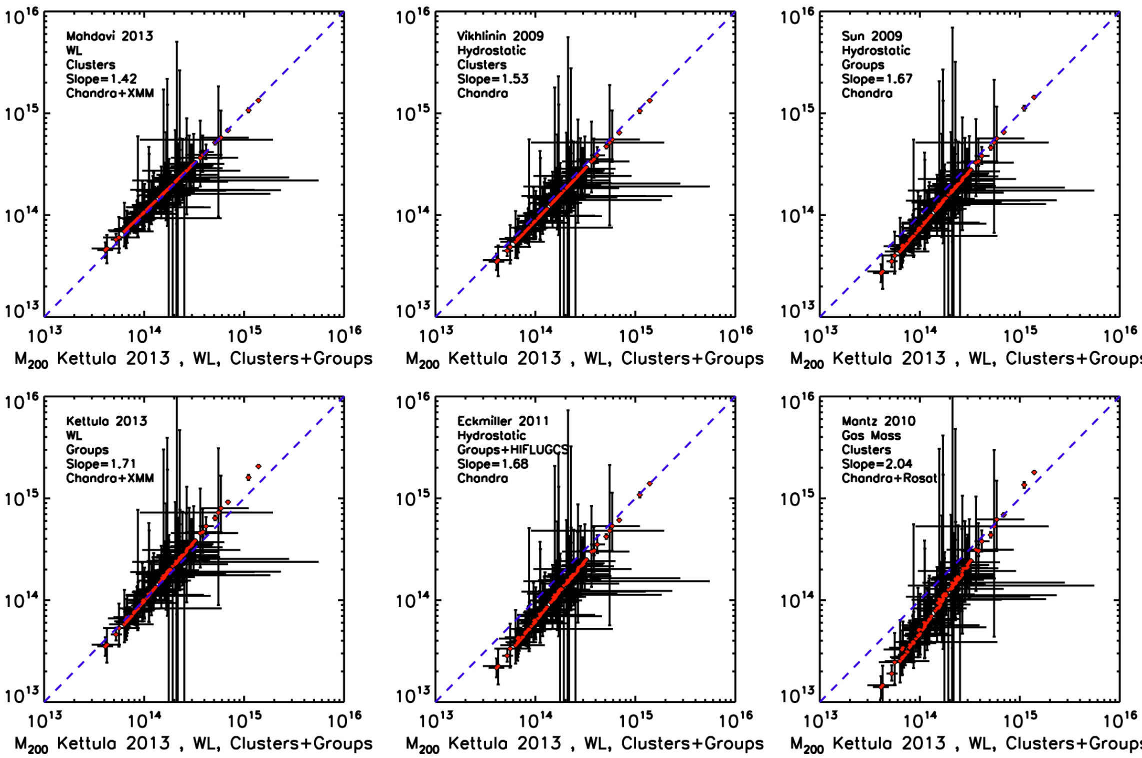

Figure 4.1 Comparison of cluster mass-temperature scaling relations from various existing studies. Masses for a given set of temperatures are calculated using each scaling relation (y-axes) and then compared to masses calculated using results from Kettula et al. (2013) (x-axes). The blue dotted lines mark y=x, and red marks the best-fit lines through the data points. $M - T_x$ relations from Kettula et al. (2013), Mahdavi et al. (2013), Vikhlinin et al. (2009a), Sun et al. (2009), Eckmiller et al. (2011), Mantz et al. (2010). Figure compiled by Zhang et al. (2016).

4.1 Scaling Relation Model

The cluster mass-temperature scaling relation can be written as

$$ME(z) \propto T_x^{\alpha} \tag{4.1}$$

for some growth rate α, where $E(z) \equiv H(z)/H_0$ accounts for self-similar evolution of clusters over time (Kaiser (1986), Bryan & Norman (1998)). Assuming virial equilibrium, where T_x scales with the depth of the gravitational potential, we would get $\alpha = 3/2$ (Kaiser (1986), Bryan & Norman (1998)).

For this work, we use M_{500} - the amount of mass contained within a radius R_{500}, within which the matter density is 500 times the critical density of the universe. Taking this into account, normalizing units, and linearizing Eqn. 4.1 for easier fitting, we get

$$\ln \frac{M_{500}E(z)}{2 \times 10^{14}\mathrm{M}_{\odot}} = \alpha \times \ln \frac{k_b T_x}{keV} + M_0 \tag{4.2}$$

where M_0 is a normalization factor. As scaling relations are often represented in linear form, α is traditionally called the "slope" of the relation.

For the course of this work, we assume a flat ΛCDM universe, with $\Omega_M \approx .29$ and $\Omega_{DE} \approx .71$. We discuss possibilities of cosmology-independent studies in Section 4.6.1.

4.2 Bayesian Framework and Likelihood Model

We use a Bayesian framework to measure the maximum-likelihood scaling relation parameters, slope α and normalization M_0. Unlike the simple minimal-χ^2 fit used to measure masses in the previous chapter, this method allows us to take into account various sources of information—and the uncertainties of these sources—when calculating the likelihood of a model. Here, we are effectively asking: given our set of individual observed temperature measurements and some values for the scaling relation parameters, what is the probability of observing the stacked masses that we measure. We then optimize for the values of the scaling relation parameters that give us the highest probability. Throughout this analysis, we assume that observed cluster properties are independent of each other.

As we assume log-normal uncertainties for both temperature and mass measurements, we work in log-space (as given in Eqn. 4.2), defining $\ln(M_{500}E(z)) = \mu_t$ and $\ln T = \tau_t$, both of which exhibit Gaussian uncertainties. μ and τ_t represent the true masses and temperatures of the system.

Assuming that the probability density function (PDF) of mass at any particular T_x is lognormal, a cluster's chances of having mass μ given temperature τ_t is

$$P(\mu|\tau_t,\theta) = \frac{1}{(2\pi)^{1/2}\sigma} \exp\left\{-\frac{(\mu - \alpha\tau_t - M_0)^2}{2\sigma^2}\right\} \tag{4.3}$$

where $\theta = (\alpha, M_0, \sigma)$ and σ is the scatter in the $M - T_x$ relation.

We incorporate the observed temperatures, τ_o, by examining the probability of a cluster having a certain true temperature, given our observed values. We assume this probability, $P(\tau_t|\tau_o)$, to also be Gaussian:

$$P(\tau_t|\tau_o) = \frac{1}{\sqrt{2\pi\sigma_{err}^2}} \exp\left\{-\frac{(\tau_o - \tau_t)^2}{2\sigma_{err}^2}\right\} \tag{4.4}$$

Here, σ_{err} is the observed T_x uncertainty. We can combine the two above equations to find the probability of measuring a mass, given scaling relation parameters and an observed temperature:

$$P(\mu|\tau_o,\theta) = \int \mathrm{d}\tau_t \; P(\mu|\tau_t,\theta)P(\tau_t|\tau_o) \tag{4.5}$$

and, integrating, take the true temperature out of the equation:

$$P(\mu|\tau_o,\theta) = \frac{1}{(2\pi\sigma_N^2)^{1/2}} \exp\left\{-\frac{(\mu - \alpha\tau_o - M_0)^2}{2\sigma_N^2}\right\} \tag{4.6}$$

where $\sigma_N^2 = \sigma^2 + \alpha^2\sigma_{err}^2$.

Taking this a step further, we look at the likelihood for a stack of clusters, rather than individual ones. Assuming the stacked mass can be represented as

$\mu_s = \sum_i w_i \times \mu_i$, where w_i is the weight of each cluster i (in our case, the number of background galaxies contributed), we get a joint PDF:

$$P(\mu_s = \sum w_i \mu_i | \tau_{o,i}, \theta) = \int \prod \mathrm{d}\mu_i \; P(w_i \mu_i | \tau_{o,i}, \theta) \delta_D(\mu_s - \sum w_i \mu_i) \tag{4.7}$$

Here, $\delta_D(\mu_s - \sum w_i \mu_i)$ represents the Dirac delta function. Integrating, we find

$$P(\mu_s = \sum w_i \mu_i | \tau_{o,i}, \theta) = \frac{1}{(2\pi\sigma_{s,N}^2)^{1/2}} \exp\left\{ -\frac{(\langle\mu\rangle - \alpha\langle\tau_o\rangle - M_0)^2}{2\langle\sigma_N^2\rangle} \right\} \tag{4.8}$$

where $\langle\sigma_N^2\rangle = \sum w_i^2 \sigma_{i,N}^2$ and $\langle\tau_o\rangle = \sum w_i \tau_{o,i}$, and $\langle\mu\rangle$ is the expected true stacked mass.

Finally, we move from true to observed masses, as we did earlier with temperatures, and incorporate our results from Chapter III along with mass-measurement uncertainties. Assuming these uncertainties to take log-normal form, we integrate out the true mass to calculate our final likelihood for each bin j:

$$P(\mu_{j,o} | \tau_{o,i}, \theta) = \frac{1}{(2\pi\sigma_{j,N}^2)^{1/2}} \exp\left\{ -\frac{(\mu_{j,o} - \alpha\langle\tau_o\rangle - M_0)^2}{2\langle\sigma_N^2 + \sigma_{j,err}^2\rangle} \right\} \tag{4.9}$$

where $\mu_{j,o}$ and $\sigma_{j,err}^2$ are the observed stacked mass and corresponding fractional mass error for cluster stack j.

Further details of these calculations can be found in the appendix of Das et al. (in prep.).

4.3 Cluster Mass and Temperature Data

Constraining the cluster mass-temperature relation requires a homogenous sample of clusters for which both X-ray observations and reliable direct mass measurements are independently available. The combination of DES-SV optical data and XCS X-ray observations provide such a sample, described in Section 3.2. This is the largest such sample for which homogeneous datasets are available for both X-ray and optical observations, removing the need to worry about discrepancies in systematics between several different sources of data. Furthermore, this sample spans a large range in both T_x ($\sim .2 - 11keV$) and z ($\sim .07 - 1.2$), allowing us to examine a larger variety of clusters. The large z range requires us to rethink usual analysis procedures, and leads us to develop a pipeline for simultaneously analyzing clusters at varying zs, as described in Chapter III. The large T_x range, in particular the inclusion of many low-T_x clusters, allows us to probe the low-mass regime of the $M - T_x$ relation further than previous studies (Kettula et al. (2013), Mantz et al. (2010), Vikhlinin et al. (2009a)), giving us deeper insight into the question of hydrostatic bias.

We bin 133 clusters of the DES-SV-XCS sample into four T_x bins, and measure stacked weak lensing masses for each bin. This process is described in detail in Chapter III; binning information is provided in Table 3.6, and the resulting masses are given in Table 3.8.

The self-similar scaling model examines the relation between $M_{500}E(z)$ and T_x. For each bin, we calculate $E(z_{bin})$ where z_{bin} is the average z of all clusters, weighted by their number of background galaxies in order to account for inhomogeneities in data.

Our likelihood model assumes log-normal uncertainties for both bin mass and individual cluster temperature. We take the fractional uncertainty for each mass bin to be

$$\sigma_{M,bin} = \sqrt{\frac{M_{500,upper}}{M_{500,lower}}}. \tag{4.10}$$

and similarly, for each cluster i,

$$\sigma_{T,i} = \sqrt{\frac{T_{x,upper}}{T_{x,lower}}}, \tag{4.11}$$

For the one cluster in the lowest T_x-bin with $T_{x,lower} = 0$, we take $\sigma_{T,i} = T_{x,upper}/T_x$.

We combine individual T_x values to calculate stacked quantities:

$$\langle \tau_o \rangle = \frac{\sum w_i \tau_{o,i}}{\sum w_i} \tag{4.12}$$

Here, $\tau_{o,i}$ is the log of the observed temperature for a binned cluster i, w_i is the number of galaxies that cluster contributes to the lensing signal for that bin, and $\langle \tau_o \rangle$ is the log of the stacked temperature of the bin.

To calculate uncertainties on $\langle \tau_o \rangle$, we take the root-mean-square combination of the observed fractional errors for all temperatures in a bin:

$$\langle \sigma_{err} \rangle = \sqrt{\frac{\sum w_i \sigma_{err,i}^2}{\sum w_i}} \tag{4.13}$$

where $\sigma_{err,i}$ is the observed fractional uncertainty for the cluster i, and $\langle \sigma_{err} \rangle$ is the uncertainty on the stacked bin temperature.

4.4 The Measured Scaling Relation

We run the above data through the Bayesian analysis described in Section 4.2, measuring the maximum-likelihood scaling relation slope and normalization. Given that we only have four T_x bins, we do not attempt to measure the scatter in the relation, but assume a scatter of 28%, as measured by Kettula et al. (2013). For slope α and normalization M_0, we use uniform priors:

$$\alpha \in [-5, 5] \quad , \quad M_0 \in [-10, 10] \; . \tag{4.14}$$

We evaluate the likelihood using the PYMC module's implementation of the Markov Chain Monte Carlo method, running 10 sets of 3,000,000 iterations each, discarding the first 50,000 iterations each time. We then average the posterior results to obtain our maximum-likelihood scaling relation parameters. Results are presented in Table 4.1, and Figure 4.2 shows our resulting $M - T_x$ relation.

Table 4.1. Results of Bayesian analysis of cluster mass-temperature scaling relation. We present our primary results, using core-excised temperatures and assuming the X-ray barycenter to be the true cluster center. In addition, we present results of variations in our data: using non-core-excised temperatures, centering on BCGs. See Section 4.5 for further details on the variations.

T_x Type	Lensing Center	Slope α	Normalization M_0
core-excised	X-ray	1.53 $\pm$.69	-1.52 $\pm$.88
core-excised	BCG	1.41 $\pm$.76	-1.45 $\pm$.86
non-core-excised	X-ray	1.92 $\pm$.88	-1.95 $\pm$1.08

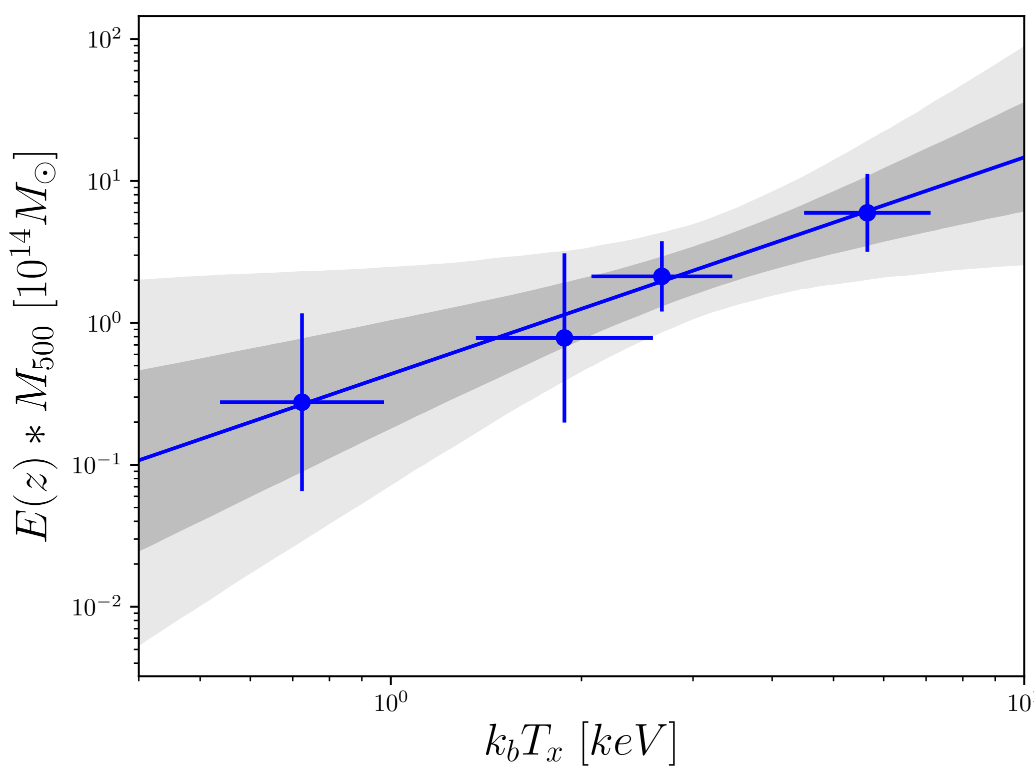

Figure 4.2 Measured $M - T_x$ scaling relation, using stacked weak lensing measurements of 133 clusters of the DES-SV-XCS sample. This analysis uses core-excised temperatures, and assumes X-ray barycenter to be cluster center. Shaded regions show 1 and 2σ bounds.

4.5 Scaling Relation Variations

In order to understand possible sources of bias in our results, we measure the $M - T_x$ scaling relation under multiple conditions. This includes testing the effect of cluster centering on our weak lensing results, as well as the effect of core-excision on X-ray measurements. Table 4.2 gives pertinent additional information for each cluster in our sample.

4.5.1 BCG Centering

Accurate pinpointing of cluster centers is imperative for weak lensing studies. Off-centering radial bins dampens the lensing signal, underestimating the cluster (or stack) mass (Johnston et al. (2007a)). As the intra-cluster medium is a good tracer for a halo's dark matter distribution, the X-ray barycenter is usually considered a good representation of the cluster center. However, most large-scale studies operate only with optical data, using the BCG (brightest cluster galaxy or bright central galaxy) as the center. While the BCG is usually close to the true center, there are concerns that this approach leads to miscentering and subsequent significant suppression of the lensing signal (Johnston et al. (2007a), Melchior et al. (2017)).

As we have both X-ray and optical data for our cluster sample, we can examine the effect of possible miscentering on the resulting scaling relation. BCGs for each cluster are found by visual examination, choosing the brightest galaxy near each cluster center. Figure 4.3 shows the separations between X-ray and BCG centers for the sample.

We re-measure $\Delta\Sigma$ profiles for each stack using the same process described in Chapter III, using BCGs as lensing centers instead of X-ray barycenters. The radial binning for each stack remains the same as given in Table 3.7. The resulting masses

Table 4.2. Additional data for the DES-XCS cluster sample, along with selected data from Tables 3.2-3.5. Column 1 is the cluster name given by XCS, and column 2 gives the DES tiling in which it is observed. Columns 3 and 4 give the position of the cluster's X-ray barycenter, and columns 5 and 6 give the position of the BCG. Columns 7-9 give the core-excised (CE) X-ray temperature, along with upper and lower bounds on uncertainties, and columns 10-12 give the same for non-core-excised (NCE) temperatures.

XCS Name	RA	Dec	RA BCG	Dec BCG	k_bT_x CE $[keV]$	$k_bT_x lower$ CE $[keV]$	$k_bT_x upper$ CE $[keV]$	k_bT_x NCE $[keV]$	$k_bT_x lower$ NCE $[keV]$	$k_bT_x upper$ NCE $[keV]$
J021757.3-045140.8	34.48875	-4.86133333	34.495122	-4.867418	0.23517	0.180649	0.374945	0.23459	0.178973	0.382354
J021653.2-041723.7	34.22166667	-4.28991667	34.219329	-4.290587	0.256319	0.192879	0.49693	1.1053	0.934871	1.37455
J021648.4-043321.3	34.20166667	-4.55591667	34.20241	-4.555307	0.339173	0.0	0.611885	0.339173	0.0	0.611885
J021755.3-052708.0	34.48041667	-5.45222222	34.479789	-5.448029	0.342073	0.297728	0.413773	0.522294	0.42492	0.601842
J233403.8-554903.9	353.5158333	-55.81775	353.522625	-55.818514	0.595134	0.462371	0.760975	2.97359	2.00575	5.17914
J232940.9-544715.3	352.4204167	-54.78758333	352.416708	-54.789478	0.606448	0.537242	0.671771	1.43196	1.18926	1.89111
J022456.1-050802.0	36.23375	-5.13388889	36.233924	-5.133166	0.6191	0.59328	0.644432	2.4421	1.98162	2.97272
J003429.6-434715.7	8.62333333	-43.78769444	8.622485	-43.78807	0.650408	0.604296	0.696994	0.719214	0.672018	0.770787
J234054.4-554256.6	355.2266667	-55.71572222	355.225967	-55.715726	0.674556	0.533798	0.865319	0.691642	0.601308	0.816133
J070411.4-563929.1	106.0475	-56.65808333	106.043374	-56.661813	0.728678	0.453689	1.197	1.58957	1.35244	1.97893
J021547.3-045030.6	33.9481	-4.8375	33.948143	-4.837531	0.73741	0.553912	1.04452	0.725892	0.526893	1.24683
J021843.7-053257.6	34.68208333	-5.54933333	34.690684	-5.548422	0.775081	0.679998	0.927261	0.707044	0.640303	0.784332
J232645.9-534839.3	351.69125	-53.81091667	351.691576	-53.811935	0.866581	0.789444	0.959474	0.792466	0.750835	0.836769
J021741.6-045148.0	34.42333333	-4.86333333	34.419578	-4.862209	0.925108	0.729506	1.20761	0.861466	0.728693	1.59228
J022318.6-052708.2	35.8275	-5.45227778	35.834135	-5.45415	0.953531	0.895091	1.01451	0.837709	0.781905	0.900545
J233204.9-551242.9	353.0204167	-55.21191667	353.019449	-55.21227	1.04931	0.914511	1.24556	3.00794	2.31709	4.07483
J022246.3-035151.2	35.69291667	-3.86422222	35.689159	-3.862943	1.11861	0.888381	5.14505	4.28931	3.20237	6.31974
J233133.8-562804.6	352.8908333	-56.46794444	352.89961	-56.466588	1.122	0.926874	1.54072	0.302166	0.224269	0.590902
J234120.8-560358.3	355.3366667	-56.06619444	355.335175	-56.066063	1.15369	0.763955	2.04919	4.12868	2.53715	7.80364
J043706.9-542919.0	69.27875	-54.48861111	69.287588	-54.4798	1.15974	0.962535	1.45717	1.28437	1.05248	1.76082
J023052.9-042050.7	37.72041667	-4.34741667	37.720812	-4.347756	1.25558	1.19326	1.3251	1.29762	1.23734	1.36076
J234311.1-555249.8	355.79625	-55.8805	355.795924	-55.881383	1.29433	1.14344	1.48213	1.36682	1.19416	1.62612
J095924.7+014614.1	149.8529167	1.77058333	149.851492	1.773234	1.29764	1.18519	1.41924	5.04037	4.06599	6.45071
J022349.7-053643.5	35.962	-5.612194	35.9604	-5.611	1.31395	1.04757	1.85403	1.26849	0.864837	7.16869
J022726.5-043207.1	36.86041667	-4.53530556	36.858446	-4.53723	1.31658	1.2222	1.42734	2.27214	1.9069	2.83433
J233706.9-541909.8	354.27875	-54.31938889	354.284169	-54.322018	1.3225	1.05266	1.75577	1.61127	1.23733	2.19026
J022454.1-032846.3	36.22541667	-3.47952778	36.227665	-3.476956	1.34859	1.03484	1.88463	1.20417	0.884637	1.74652
J022401.9-050528.4	36.00791667	-5.09122222	36.009003	-5.090715	1.35068	1.14641	1.67069	1.40052	1.24194	1.62953
J022347.6-025127.1	35.94833333	-2.85752778	35.954099	-2.857176	1.35508	1.21223	1.56132	1.8065	1.53418	2.25966
J021940.8-055043.7	34.919917	-5.845472	34.924826	-5.846542	1.36081	1.12005	1.91082	1.36081	1.12005	1.91082
J022433.9-041432.7	36.14125	-4.24241667	36.13845	-4.238674	1.41376	1.3264	1.51493	1.43501	1.34485	1.54295
J100023.1+022358.0	150.0909	2.3912	150.09092	2.391251	1.42181	1.28034	1.6143	1.34888	1.22703	1.49193
J021945.5-044834.3	34.93958333	-4.80952778	34.936125	-4.812368	1.42625	1.09382	2.41272	1.38057	1.14807	1.99169
J004157.8-442026.5	10.49083333	-44.34069444	10.486495	-44.334383	1.47265	1.1986	6.80398	1.56316	1.27732	2.10871
J022808.6-053543.6	37.03583333	-5.59544444	37.035652	-5.594735	1.48318	1.27338	1.83874	1.28042	1.09817	1.62048
J233637.8-524409.4	354.1575	-52.73594444	354.154442	-52.737594	1.52956	1.31903	1.90467	1.80514	1.47873	2.36419
J022318.3-051209.8	35.82625	-5.20272	35.819074	-5.208269	1.58621	1.12652	4.05797	1.43885	1.16705	1.92748

Table 4.3. Table 4.2, contd. Additional data for the DES-XCS cluster sample, along with selected data from Tables 3.2-3.5. Column 1 is the cluster name given by XCS, and column 2 gives the DES tiling in which it is observed. Columns 3 and 4 give the position of the cluster's X-ray barycenter, and columns 5 and 6 give the position of the BCG. Columns 7-9 give the core-excised (CE) X-ray temperature, along with upper and lower bounds on uncertainties, and columns 10-12 give the same for non-core-excised (NCE) temperatures.

XCS Name	RA	Dec	RA BCG	Dec BCG	k_bT_x CE $[keV]$	$k_bT_x lower$ CE $[keV]$	$k_bT_x upper$ CE $[keV]$	k_bT_x NCE $[keV]$	$k_bT_x lower$ NCE $[keV]$	$k_bT_x upper$ NCE $[keV]$
J022307.9-041257.2	35.78291667	-4.21588889	35.794975	-4.214364	1.6135	1.25913	3.13495	2.26399	1.50636	0.0
J022303.2-043620.3	35.76333333	-4.60563889	35.765517	-4.605096	1.6225	1.31176	2.26561	1.78432	1.3898	2.5737
J003321.0-433737.1	8.3375	-43.62697222	8.340581	-43.62355	1.6497	1.35909	2.18443	2.17849	1.69915	2.88395
J100027.1+022131.7	150.1129167	2.35880556	150.11435	2.356499	1.65084	1.31396	2.25364	1.65507	1.44133	1.98877
J022405.8-035505.5	36.02416667	-3.91819444	36.024027	-3.921251	1.65112	1.16401	3.03758	5.13313	2.99764	10.8335
J023052.4-045123.5	37.71833333	-4.85652778	37.722796	-4.858408	1.65765	1.32269	2.54678	1.65765	1.32269	2.54678
J095901.2+024740.4	149.755	2.79455556	149.75632	2.794723	1.66163	1.39325	2.18372	1.45171	1.26585	1.70731
J022103.2-050612.0	35.26333333	-5.10333333	35.266661	-5.099087	1.66678	1.10726	2.65435	2.56164	1.91714	3.73739
J022204.5-043239.4	35.51875	-4.54427778	35.519001	-4.550023	1.68655	1.43939	2.09332	2.14548	1.74674	3.22686
J021943.8-045314.1	34.9325	-4.88725	34.922889	-4.875183	1.70321	1.44634	2.1419	1.26905	1.09746	1.55977
J003518.1-433402.4	8.82541667	-43.56733333	8.814985	-43.56601	1.70535	1.6307	1.7875	1.75817	1.71538	1.80447
J022532.0-035509.5	36.38333333	-3.91930556	36.385272	-3.919279	1.71997	1.34262	2.30656	3.59184	2.70182	5.01752
J022357.5-043520.7	35.98958333	-4.58908333	35.989682	-4.586111	1.7876	1.49906	2.21237	1.66766	1.41513	2.03346
J022342.3-050200.9	35.92625	-5.03358333	35.927369	-5.033576	1.80665	1.43772	2.52818	1.88506	1.4585	2.73389
J023037.2-045929.5	37.655	-4.99152778	37.661547	-4.990949	1.84803	1.62556	2.17681	1.85959	1.63304	2.22859
J233835.2-543729.5	354.6466667	-54.62486111	354.647749	-54.624178	1.85557	1.5382	2.40552	4.9494	1.38816	10.9678
J022042.7-052550.0	35.17791667	-5.43055556	35.17565	-5.431059	1.93471	1.5444	2.52561	1.77766	1.54846	2.13079
J232804.7-563004.5	352.0195833	-56.50125	352.01955	-56.501411	1.94646	1.65068	2.3638	1.99884	1.71457	2.42862
J232952.7-532105.2	352.4695833	-53.35144444	352.465109	-53.351743	1.97668	1.49779	2.98688	1.73054	1.11477	3.32784
J003545.5-431756.0	8.93958333	-43.29888889	8.932651	-43.297347	1.99521	1.44678	2.75588	0.787328	0.6866	0.943212
J095902.7+025544.9	149.76125	2.92913889	149.761335	2.929103	2.02349	1.75137	2.38555	3.35576	2.99061	3.79697
J235058.9-552208.4	357.747917	-55.368361	357.752417	-55.370402	2.03796	1.70634	2.55327	2.13853	1.85979	2.53799
J233546.6-535039.3	353.9441667	-53.84425	353.954497	-53.8385	2.04402	1.67195	2.57088	2.30115	1.81531	3.06471
J233037.2-554340.2	352.655	-55.72783333	352.654366	-55.727435	2.06867	1.56648	3.04236	2.37036	1.78909	3.54412
J043021.9-613158.8	67.59125	-61.533	67.591639	-61.533533	2.08008	1.37525	6.99705	8.67224	8.19006	9.20406
J022524.8-044043.4	36.35333333	-4.67872222	36.352957	-4.679182	2.08725	1.30789	4.46585	2.30038	2.09459	2.55087
J042017.5-503153.9	65.07291667	-50.53163889	65.074195	-50.531716	2.11122	1.95557	2.29472	2.33985	2.15636	2.55533
J041644.8-552506.6	64.18666667	-55.4185	64.186695	-55.416764	2.16923	1.82157	2.71095	2.45885	2.02333	3.1665
J021734.7-051327.6	34.39458333	-5.22433333	34.392413	-5.22752	2.1785	1.74224	3.01444	2.18322	1.78411	2.91826
J235009.3-551957.9	357.539583	-55.33275	357.539493	-55.333109	2.17856	1.83411	2.66587	1.95121	1.6705	2.33785
J233216.0-544205.5	353.0666667	-54.70152778	353.064584	-54.703202	2.18402	1.80567	2.77462	3.4907	2.84911	4.3336
J065744.2-560817.0	104.4341667	-56.13805556	104.433734	-56.138378	2.2019	2.00394	2.42992	2.27955	2.03756	2.58763
J022722.4-032142.8	36.84333333	-3.36188889	36.843313	-3.360918	2.24681	2.0882	2.43619	2.14801	2.01099	2.29134
J023009.8-054039.3	37.54083333	-5.67758333	37.539524	-5.675963	2.29182	1.26567	4.25778	2.77151	1.60086	4.4558
J233000.5-543706.3	352.5020833	-54.61841667	352.501689	-54.6188	2.30973	2.13561	2.51156	2.65124	2.47596	2.8485
J022509.7-040137.9	36.29041667	-4.02719444	36.293654	-4.030517	2.31896	1.72342	3.67876	2.12751	1.61909	3.19455
J095951.2+014045.8	149.9633333	1.67938889	149.964143	1.68036	2.35732	2.15382	2.6094	2.11241	1.92488	2.34695

Table 4.4. Table 4.2, contd. Additional data for the DES-XCS cluster sample, along with selected data from Tables 3.2-3.5. Column 1 is the cluster name given by XCS, and column 2 gives the DES tiling in which it is observed. Columns 3 and 4 give the position of the cluster's X-ray barycenter, and columns 5 and 6 give the position of the BCG. Columns 7-9 give the core-excised (CE) X-ray temperature, along with upper and lower bounds on uncertainties, and columns 10-12 give the same for non-core-excised (NCE) temperatures.

XCS Name	RA	Dec	RA BCG	Dec BCG	k_bT_x CE $[keV]$	$k_bT_x lower$ CE $[keV]$	$k_bT_x upper$ CE $[keV]$	k_bT_x NCE $[keV]$	$k_bT_x lower$ NCE $[keV]$	$k_bT_x upper$ NCE $[keV]$
J023026.7-043444.5	37.61125	-4.57902778	37.615592	-4.563563	2.36937	1.81555	3.52659	2.52644	1.88449	3.79308
J234142.9-555748.9	355.42875	-55.96358333	355.432969	-55.96369	2.37922	2.05101	2.83087	2.87017	2.39692	3.54839
J233955.1-561519.6	354.9795833	-56.25544444	354.974981	-56.250822	2.44045	1.60948	4.04356	1.52526	1.18426	2.6808
J041629.2-553254.9	64.12166667	-55.54858333	64.12194	-55.549422	2.45203	1.79293	4.22874	1.69075	1.42859	2.12128
J232713.8-560333.5	351.8075	-56.05930556	351.80767	-56.060549	2.46776	2.0058	3.12617	2.40552	2.00762	2.98873
J003306.4-433340.0	8.27666667	-43.56111111	8.2762	-43.565589	2.47798	1.54221	5.75969	2.64805	1.58967	5.98561
J022829.7-031256.6	37.12375	-3.21572222	37.122987	-3.217662	2.48747	2.04088	3.08723	3.34385	2.39122	4.83023
J022917.7-055345.9	37.32375	-5.89608333	37.32229	-5.901518	2.48861	1.96206	3.29452	3.50321	2.68703	4.98871
J003346.3-431729.7	8.44291667	-43.29158333	8.443268	-43.291959	2.50623	2.35327	2.67049	2.29467	2.19538	2.4037
J022417.1-050314.8	36.07125	-5.05411111	36.070802	-5.056811	2.50831	1.75951	4.08258	2.66496	1.91165	4.47756
J233644.6-534806.9	354.1916	-53.7949	354.183453	-53.795907	2.54074	1.67795	4.64263	2.06167	1.60698	2.82141
J233345.8-553826.9	353.4408333	-55.64080556	353.441511	-55.637993	2.55753	1.75264	4.1716	1.89563	1.47768	2.88114
J100043.0+014559.2	150.1791667	1.76644444	150.180033	1.768896	2.58357	2.17911	3.15885	2.64107	2.20601	3.26218
J022024.7-050232.0	35.10291667	-5.04222222	35.103215	-5.042116	2.5947	2.31125	2.94407	2.25947	1.85698	2.92853
J234231.5-562105.9	355.63125	-56.35163889	355.630908	-56.353086	2.68328	2.3208	3.14821	2.97439	2.59699	3.44256
J021529.0-044052.8	33.87083333	-4.68133333	33.867607	-4.678078	2.68598	2.25595	3.33397	2.77805	2.32904	3.39459
J233745.5-562757.7	354.4395833	-56.46602778	354.43556	-56.465257	2.7336	2.11926	3.65245	2.41256	1.97575	3.00463
J021832.5-050053.3	34.63541667	-5.01480556	34.624193	-5.027242	2.77872	2.3373	3.35064	2.37361	2.05936	2.79796
J003548.1-432232.8	8.95041667	-43.37577778	8.947983	-43.379386	2.86782	2.43418	3.44477	2.93555	2.52366	3.48053
J233043.1-530321.7	352.6795833	-53.05602778	352.679947	-53.057191	2.93258	2.05814	4.48744	2.91062	1.98445	4.85067
J233607.6-535232.4	354.0316667	-53.87566667	354.029719	-53.876581	2.94754	2.34066	3.90463	2.98276	2.40198	3.78011
J003627.6-432830.3	9.115	-43.47508333	9.119422	-43.475432	2.98548	1.7816	5.18471	1.53676	1.31361	1.92381
J021803.4-055526.5	34.51416667	-5.92402778	34.515362	-5.93098	3.03237	1.73798	12.454	1.71783	1.38398	2.31454
J034025.8-284031.3	55.108125	-28.673722	55.10494	-28.677497	3.06766	2.87918	3.27405	3.06766	2.87918	3.27405
J003428.0-431854.2	8.61666667	-43.31505556	8.614189	-43.316563	3.07993	2.92718	3.24303	3.15205	3.0103	3.30347
J034106.0-284132.2	55.275	-28.69227778	55.278285	-28.693408	3.13824	2.28628	4.92239	4.28773	2.85625	7.19617
J234806.2-560121.1	357.0258333	-56.02252778	357.023144	-56.023839	3.14762	2.54428	4.03638	3.1886	2.38094	4.71198
J234730.6-553322.9	356.8775	-55.55636111	356.859894	-55.5675	3.188	2.53698	4.1592	2.06715	1.72199	2.54623
J022457.9-034849.4	36.24125	-3.81372222	36.238737	-3.814703	3.21416	2.7727	3.76913	3.35509	2.893	3.95195
J042226.4-514025.8	65.61	-51.67383333	65.610213	-51.675323	3.22887	2.96279	3.53116	2.89227	2.6841	3.13064
J100047.3+013927.8	150.1970833	1.65772222	150.189817	1.657398	3.23242	3.08027	3.42052	2.96585	2.81534	3.12955
J232956.6-560808.0	352.4858333	-56.13555556	352.483023	-56.135664	3.31132	2.77724	4.03831	2.79761	2.49038	3.16854
J043218.6-610351.9	68.0775	-61.06441667	68.069697	-61.063601	3.31441	2.6053	4.49172	3.48001	2.574	5.19985
J043327.2-612717.6	68.36333333	-61.45488889	68.365926	-61.451741	3.33872	2.57596	4.49711	3.40319	2.51752	4.55457
J022709.9-041800.5	36.79125	-4.30013889	36.788282	-4.303973	3.38586	2.57342	4.80427	3.85064	2.76809	5.82839
J022403.8-041332.8	36.01583333	-4.22577778	36.017409	-4.224018	3.50943	3.25569	3.79799	3.61859	3.38862	3.86838
J003339.4-435422.6	8.41416667	-43.90627778	8.414447	-43.90772	3.61297	2.34937	6.75705	3.93335	2.68543	6.52135

Table 4.5. Table 4.2, contd. Additional data for the DES-XCS cluster sample, along with selected data from Tables 3.2-3.5. Column 1 is the cluster name given by XCS, and column 2 gives the DES tiling in which it is observed. Columns 3 and 4 give the position of the cluster's X-ray barycenter, and columns 5 and 6 give the position of the BCG. Columns 7-9 give the core-excised (CE) X-ray temperature, along with upper and lower bounds on uncertainties, and columns 10-12 give the same for non-core-excised (NCE) temperatures.

XCS Name	RA	Dec	RA BCG	Dec BCG	k_bT_x CE $[keV]$	$k_bT_x lower$ CE $[keV]$	$k_bT_x upper$ CE $[keV]$	k_bT_x NCE $[keV]$	$k_bT_x lower$ NCE $[keV]$	$k_bT_x upper$ NCE $[keV]$
J051141.2-515420.8	77.92166667	-51.90577778	77.928812	-51.910231	3.82909	3.45697	4.28096	4.10785	3.73877	4.53637
J022400.3-032520.5	36.00125	-3.42236111	36.002486	-3.426587	3.96039	2.25182	9.6884	2.75101	2.00641	4.02327
J232633.3-550116.3	351.63875	-55.02119444	351.640193	-55.019833	3.96843	3.32605	4.78923	3.12119	2.77371	3.56474
J034004.2-283159.2	55.0175	-28.53311111	55.012031	-28.534752	4.02992	2.06039	7.39042	1.91226	1.65079	2.36952
J023138.4-043439.1	37.91	-4.57752778	37.912841	-4.577184	4.12793	1.49112	12.2527	1.96584	1.39897	4.69794
J095823.4+024850.9	149.5963	2.8189	149.600089	2.821181	4.4599	3.78328	5.3204	4.0545	3.61358	4.59965
J232801.9-545550.1	352.0079167	-54.93058333	352.008244	-54.928931	4.47352	2.26773	9.74588	5.04996	2.91903	9.76764
J095737.1+023428.9	149.4045833	2.57469444	149.404209	2.573747	4.48033	3.79843	5.36205	4.49512	3.94461	5.16067
J021441.2-043313.8	33.67166667	-4.55383333	33.671242	-4.567278	4.49236	4.35318	4.64711	4.74372	4.62007	4.87248
J041805.0-474941.8	64.52083333	-47.82827778	64.52372	-47.827636	4.78799	3.72724	6.30757	4.73788	3.64357	6.53636
J023337.7-053026.5	38.407083	-5.507361	38.4157	-5.511	4.88583	4.14034	5.82911	5.08888	4.32704	6.13817
J100201.4+021334.2	150.505917	2.226167	150.505034	2.225095	4.88741	4.322	5.59096	4.74441	4.22451	5.38167
J095940.7+023110.8	149.9195833	2.51966667	149.923436	2.525051	4.97681	4.40607	5.69434	5.32837	4.66485	6.11874
J022543.9-031147.1	36.43291667	-3.19641667	36.438533	-3.208459	5.01447	4.44121	5.74944	3.66568	3.43894	3.91147
J034025.8-282830.6	55.1075	-28.47516667	55.111495	-28.473905	5.02908	3.2456	9.56934	2.10325	1.64939	2.92904
J232842.9-553357.4	352.17875	-55.56594444	352.179009	-55.566831	5.17507	3.7352	7.28742	4.48216	3.4242	6.12241
J023142.2-045253.1	37.92583333	-4.88141667	37.921533	-4.882582	5.42064	5.2736	5.57406	4.16464	4.1506	4.20888
J051636.6-543120.8	79.1525	-54.52244444	79.155705	-54.500463	6.25923	6.14724	6.37558	6.04171	5.93301	6.15739
J041722.7-474847.1	64.34458333	-47.81308333	64.346186	-47.8132	6.7404	6.34136	7.18995	6.52259	6.25423	6.81098
J043818.3-541916.5	69.57625	-54.32125	69.573584	-54.322326	7.98878	7.67708	8.31925	8.00688	7.75788	8.27312
J065828.8-555640.8	104.62125	-55.944861	104.658755	-55.957166	9.38927	9.22382	9.56305	9.42547	9.28534	9.56907
J224844.9-443141.7	342.1870833	-44.52825	342.18318	-44.530805	11.0916	10.8634	11.3294	10.9813	10.818	11.1489

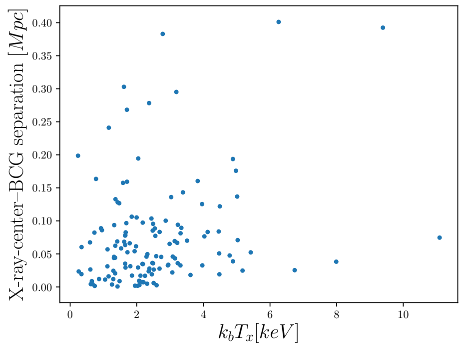

(a)

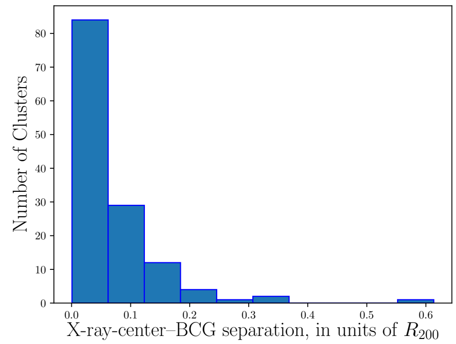

(b)

Figure 4.3 Separations between X-ray and BCG centers: (a) Separation in Mpc, plotted against temperature. (b) Histogram of separations, in units of R_{200}.

Table 4.6. Best-fit M_{500} for each stack, centered on cluster BCGs. Column 1 is the stack id, column 2 gives the best-fit mass, and columns 3 and 4 give the lower and upper bounds respectively on 1σ uncertainties.

Temperature Bin Name	Best-fit M_{500} [$10^{14}\mathrm{M}_{\odot}$]	$M_{500,lower}$ [$10^{14}\mathrm{M}_{\odot}$]	$M_{500,upper}$ [$10^{14}\mathrm{M}_{\odot}$]
bin0	0.0508	~ 0	0.283
bin1	1.89	0.901	3.38
bin2	1.15	0.416	2.23
bin3	3.83	1.48	6.95

are given in Table 4.6. Observed and best-fit lensing profiles and likelihoods with 1σ bounds are shown in Figure 4.4.

We follow the same procedure for constraining the scaling relation as we did with our primary analysis, including modeling log-normal uncertainties for input into the Bayesian framework. The exception is bin0, where $M_{500,lower} \sim 0$—we use $\sigma_{M,bin} = M_{500,upper}/M_{500}$ instead. The resulting scaling relation parameters are given in Table 4.1, and comparisons to our primary analysis are shown in Figure 4.5.

4.5.2 Non-core-excised Temperatures

Galaxy cluster profiles may exhibit cooler central regions than the rest of the ICM due to processes such as radiative cooling (Fabian (1994), Henning et al. (2009)). These "cool cores" can bias measurements of T_x, affecting subsequent constraints

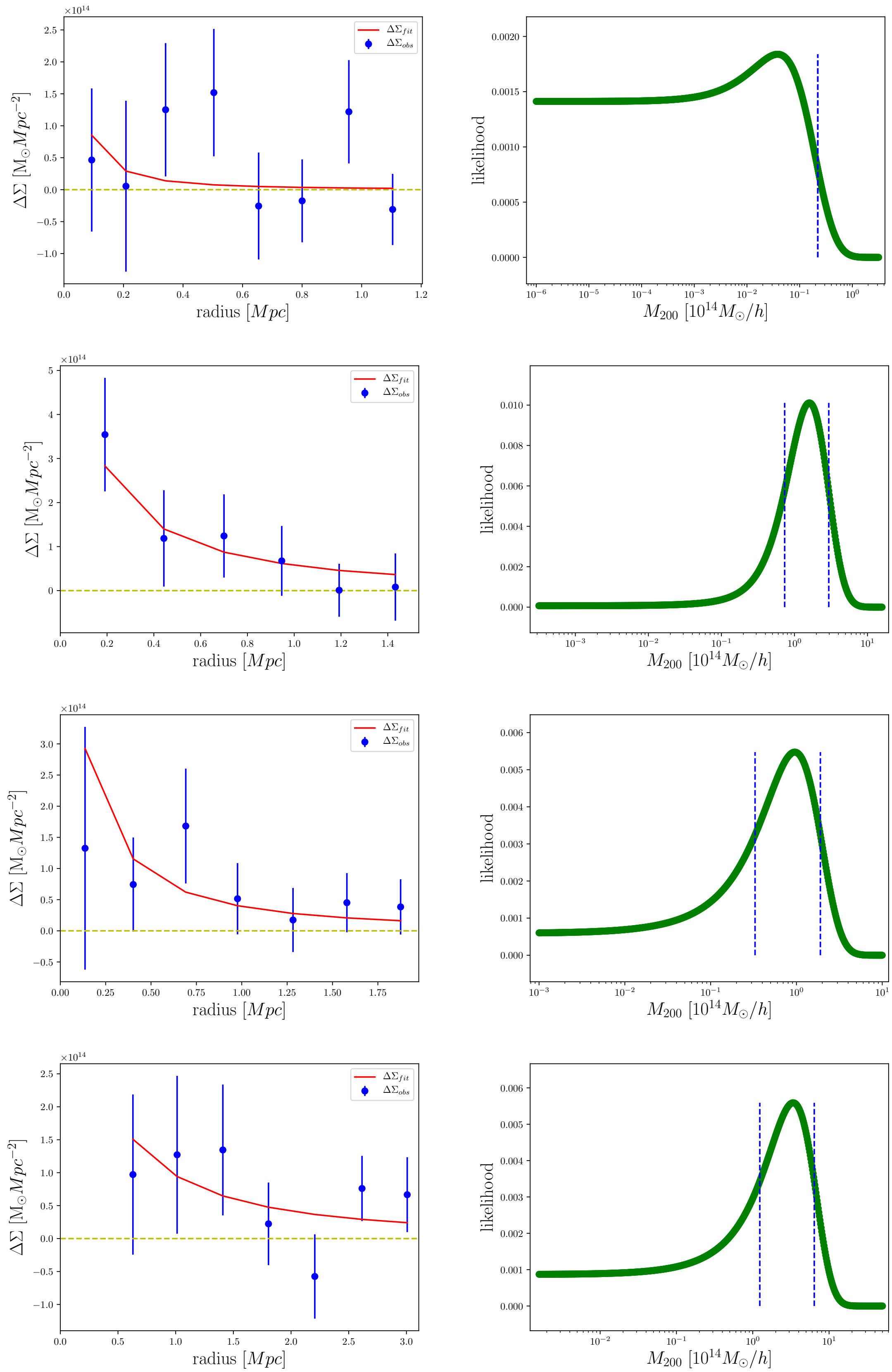

Figure 4.4 Lensing signals and best-fit models using BCG centering. (left) Best-fit $\Delta\Sigma$ profiles for each T_x bin, overlaid on the measured $\Delta\Sigma$ values. (right) Likelihoods for our model masses for each bin, with 1σ uncertainties marked. Bins go from low to high T_x, from top to bottom.

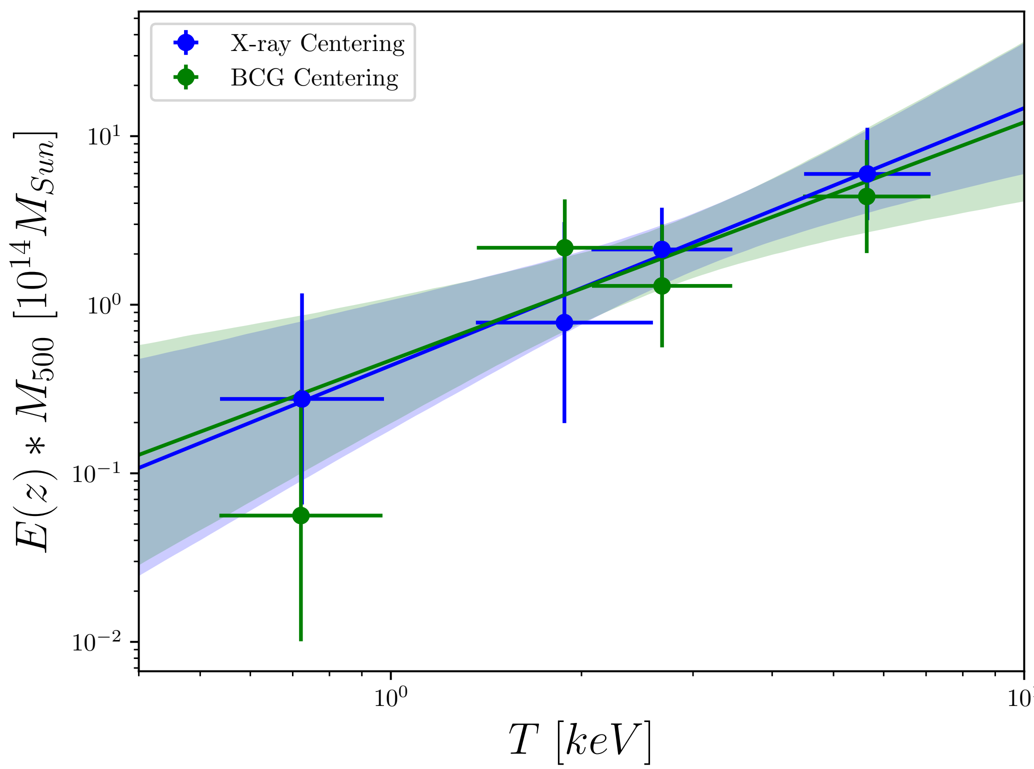

Figure 4.5 Comparing measured $M - T_x$ scaling relations: using X-ray barycenters vs BCGs as cluster centers. Shaded regions show 1σ bounds.

on scaling relations. It has been observed that excluding cluster cores from X-ray calculations decreases the scatter in scaling relations (Vikhlinin et al. (2009a))—as such, most recent cluster X-ray studies measure temperatures using spectra outside the cluster core (e.g., Kettula et al. (2013), Vikhlinin et al. (2009b), Mantz et al. (2010), among others). For our primary analysis, we use core-excised T_x measurements, where spectra from a central region of radius $.15R_{200}$ have been excluded from calculations.

To understand possible effects of cool cores on the $M-T_x$ relation, we constrain the scaling law using non-core-excised temperatures as well, where spectra from within the entire detection aperture are used. Figure 4.6 shows the variations between the two different T_x measurements.

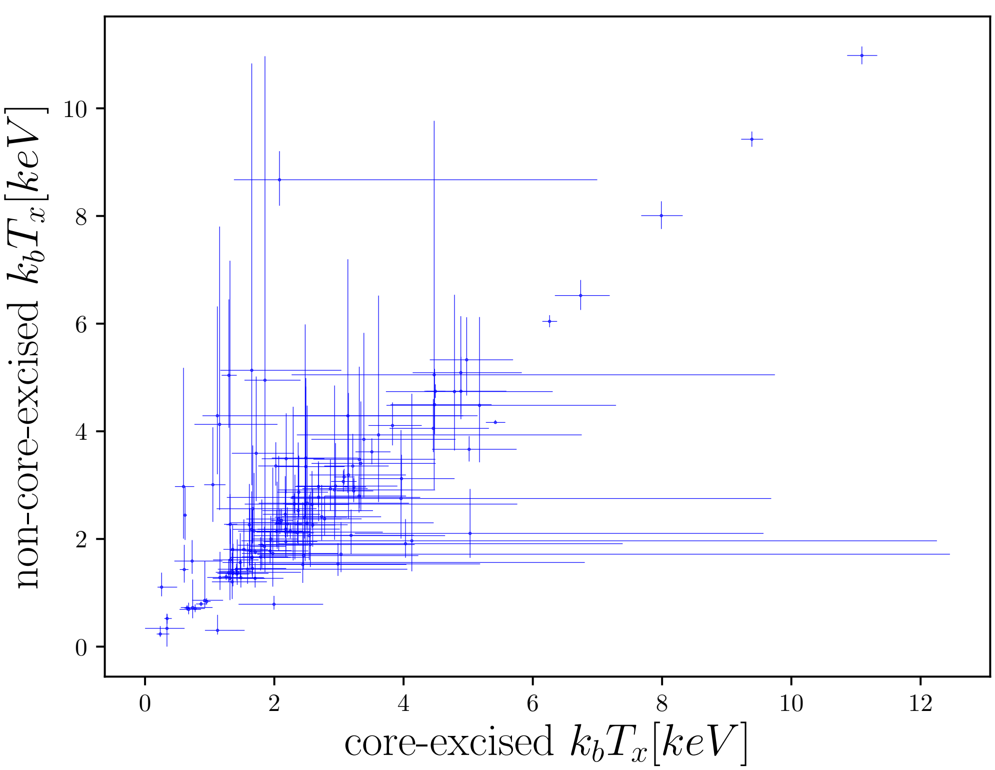

Figure 4.6 Comparison between core-excised and non-core-excised cluster temperatures.

We use the same cluster stacks and measured masses as our primary analysis, given in Tables 3.7 and 3.8, and substitute in non-core-excised T_x values. The resulting scaling relation parameters are given in Table 4.1, and comparisons to our primary analysis are shown in Figure 4.7. Note that this method varies somewhat from our primary method - clusters are not binned strictly by non-core-excised temperatures, but rather left in the bins defined by core-excised measurements. This allows us to compare results for each bin. A more independent scaling relation between mass and non-core-excised temperatures would be obtained by binning the sample directly using these values, and is worth exploring in future works.

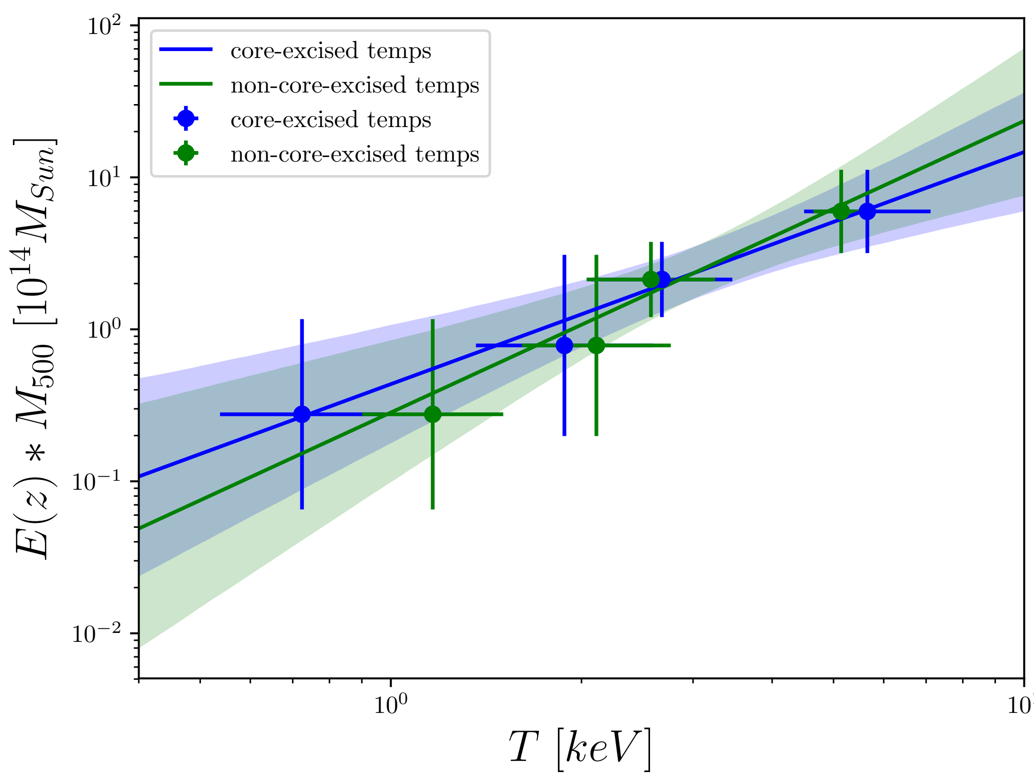

Figure 4.7 Comparing measured $M - T_x$ scaling relations: using core-excised vs non-core-excised temperatures. Shaded regions show 1σ bounds.

4.6 Discussion and Summary

In this chapter, we constrain the galaxy cluster mass-temperature scaling relation using the DES-SV-XCS cluster sample. This is the largest sample of clusters currently used to constrain the $M - T_x$ relation where both optical and X-ray data come from homogeneous sources. We use stacked weak lensing masses derived from DES optical data (see Chapter III) and core-excised temperatures from XCS X-ray data.

The wide T_x range of this sample gives us unprecedented ability to probe the $M - T_x$ relation in the low-mass regime. Our measured slope, $\alpha = 1.53 \pm .69$, is consistent with the self-similar model in virial equilibrium.

Figure 4.8 shows our scaling relation overlaid with several measurements from previous literature. For relevancy in comparison, we only look at other scaling relations measured using core-excised temperatures. We find our constraints to be consistent with these studies to within 1σ uncertainties. The green line in the figure shows results from Mantz et al. (2010), who use masses calculated assuming hydrostatic equilibrium and measure a steeper scaling relation slope than other recent studies. While our results match up well to measurements by Kettula et al. (2013), who observed a significant difference between their slope (constrained using weak lensing masses) and ones calculated using hydrostatic measurements, our uncertainties are too high to either confirm or rule out hydrostatic bias, based on our comparison with the Mantz2010 relation..

Centering the lensing analysis on BCGs rather than X-ray centers does not produce any significant changes in our scaling relation. Though the $\Delta\Sigma$ profiles are noisier and look suppressed near the cluster centers, the final masses agree within 1σ uncertainties.

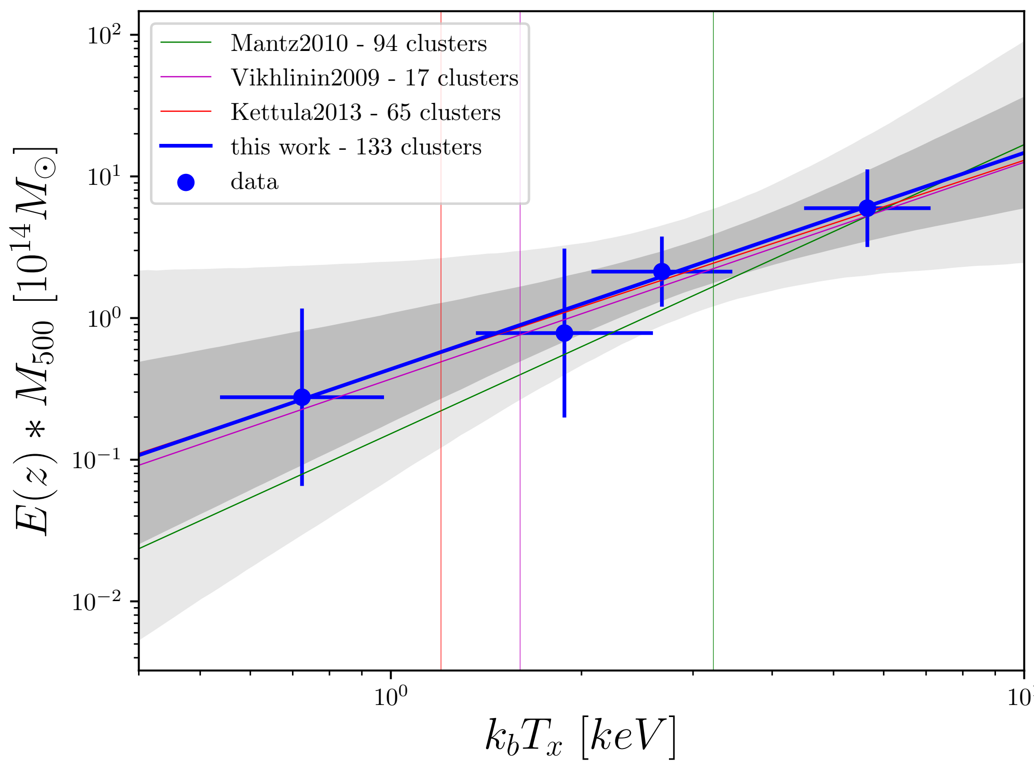

Figure 4.8 Our measured $M - T_x$ scaling relation, with 1 and 2σ bounds, compared with results from Kettula et al. (2013), Vikhlinin et al. (2009b), and Mantz et al. (2010). Vertical lines mark lower bounds on temperature of the samples used in the scaling relations marked with the same colors.

Including spectra from cluster cores in the T_x measurements also does not change the scaling relation significantly. We compare our results to a $M - T_x$ scaling relation measured using non-core-excised temperatures by Mantz et al. (2010) and find them to be consistent with each other (see Figure 4.9) . It is interesting to note that excising the core seems to lower temperatures for low-T_x clusters, but increases temperatures for high-T_x clusters. This matches with measurements of cluster temperature profiles presented in Section 5 of Vikhlinin & Kravtsov (2006), where low-T_x clusters exhibit a much sharper temperature rise and fall near the core. For several of our low-T_x clusters, it is likely that temperature profiles keep rising within the $.15R_{200}$ range—though they may drop off into a cool core at smaller radii, the presence of this higher-temperature gas would be noted by our non-core-excised temperature measurements. Rasmussen & Ponman (2007) find that the ratios of core to peak temperatures are higher for low-T_x systems, and that their peak temperatures occur closer to their cores—this also aligns with our observations.

4.6.1 Future Prospects

Our ability to distinguish between scaling models, measure possible biases, and examine effects of variations on cluster properties depends directly on the size of the uncertainties on our measured $M - T_x$ relation. Working with DES Science Verification data, we measure a scaling relation that is consistent with the expected self-similar model, but is not constrained enough to rule out or confirm hydrostatic bias. While replacing X-ray centers with BCGs as lensing centers changes resulting stack masses by considerable amounts, both measurements are still consistent within the large 1σ uncertainties.

The DESY3-XCS sample will contain clusters from the entire Dark Energy Survey footprint, and will be backed up by galaxy ellipticity data from the first three years

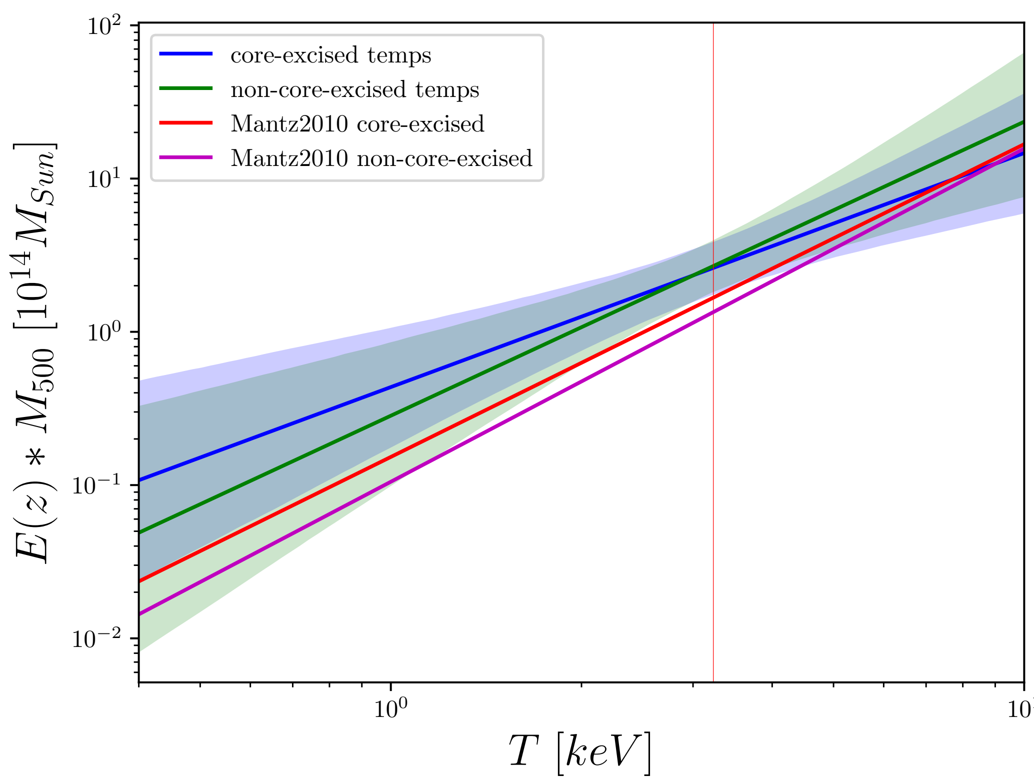

Figure 4.9 Our measured $M - T_x$ scaling relations, using both core-excised and non-core-excised temperatures, compared with corresponding results from Mantz et al. (2010). The vertical lines marks the lower bound on core-excised temperatures used by Mantz et al. (2010). Shaded regions bound 1σ regions of our fits.

of DES operations. This increases the dataset two-fold: not only will we gain a substantial number of clusters, but many clusters will have a much deeper and/or denser sample of background galaxies (see Section 3.8 for details on galaxy count increase). The DESY3-XCS cluster sample is currently being assembled, and is expected to contain at least ~ 400 clusters, possibly more. This would at a minimum almost triple our lens sample. The DES-Y3 shape galaxy shape catalogs are expected within the next few months. Greater numbers of background galaxies will cause the uncertainties on mass measurements to shrink, and a larger cluster sample will likely allow an increase in the number of temperature bins. Both these effects should lead to lower uncertainties in the resulting scaling law. Given enough data, it may be possible to constrain not only the slope and normalization, but the scaling law scatter as well.

Despite the greater quantities of data, it is unclear whether future DES-XCS cluster samples will be large enough to constrain the $M - T_x$ scaling relation independent of cosmological parameters. Our analysis framework is dependent on an assumed cosmology in order to measure angular diameter distances, crucial both for measuring $\Delta\Sigma$ and for converting sky separations into Mpc. A cosmology-independent analysis would require the use of shear as the lensing estimator, rather than $\Delta\Sigma$, which subsequently requires careful treatment of the range of cluster background galaxies—this we have already done with our use of individual source-lens pairs to model the lensing signal, and can modify our analysis easily to use shear instead of the surface mass density contrast. However, to conduct a stacked-cluster weak lensing analysis without converting background galaxy separations into Mpc would require tight binning in redshift, as nearer clusters of the same mass will spread out far more in angular coordinates. Requiring z-binning in addition to T_x binning demands a far higher number of clusters in order to maintain detectable lensing signals, especially in the low-T_x and high-z regimes. It is unclear whether the overlap of the DES and XCS footprints will provide such a large sample of clusters. Studies of this type may instead fare better with samples where XCS has greater overlap with an optical survey, such as the SDSS-XCSDR2 cluster set, containing 1255 clusters (Manolopoulou et al. (in prep.)). Given such a large sample of clusters, our analysis method is adaptable for use for constraining the scaling relation independent of cosmology.

CHAPTER V

Conclusion

This dissertation combines information about galaxy clusters from the Dark Energy Survey (DES) and the XMM Cluster Survey (XCS) with observations of galaxies from DES to measure the relation between cluster mass and temperature, a step in the path towards using cluster abundances to understand dark energy.

We begin in this endeavor by measuring the shapes of galaxies. Following in the footsteps of the Dark Energy Survey weak lensing team, we measure galaxy shapes in areas of the sky that were observed as part of the DES Science Verification (SV) run, but left out of the official DES SV shear catalog. We validate these additional measurements by comparing their ensemble qualities to those of the official catalog, showing that the extra areas are usable for our studies. We present this data, shapes for $\sim 590,000$ galaxies in the DES-SV sky—an approximately 27% addition to the official catalog—for public use. We also include a brief description of how to measure shapes with Im3shape, documenting for use in any future such ventures.

We then use weak gravitational lensing to measure direct masses for a sample of 133 galaxy clusters, stacking them into four bins by core-excised temperatures in order to strengthen the observed signal, and adopting X-ray barycenters as lensing centers. In order to work with the inhomogeneous nature of SV data, we develop a method of modeling the lensing signal that takes into account the sparsity (or abundance) of galaxy data behind any given cluster, and check its robustness by subjecting it to various tests. This method builds up the theoretical model profile by incorporating information about observed individual source-lens pairs, making sure that clusters contribute to the model in a way that is representative of their contributions to the observed signal. Thus, this method maximizes the data we can use in cluster weak lensing studies by allowing us to include clusters for which we have incomplete background galaxy samples. For example, clusters near the edges of fields of view, clusters with inhomogeneous data due to weather conditions, and high-z clusters can now be examined through stacked weak lensing methods. See Appendix A for details on how to access and run this pipeline, which we name LensStack.

Having measured best-fit masses for four temperature bins, we adopt a Bayesian framework to constrain the mass-temperature scaling relation. We find our results to be consistent with the self-similar model and virial collapse, with a scaling relation slope $\alpha = 1.53 \pm .69$, but find our uncertainties too high to discern the presence (or absence) of hydrostatic bias in cluster mass measurements. In exploring the effect on the scaling law of several variations in our dataset, we find that neither the use of non-core-excised cluster temperatures, nor the adoption of cluster BCGs as lensing centers, affects the results beyond the range of uncertainties.

The limiting factor in our analysis is, of course, the quantity and quality of data. DES SV only covers a small part of the sky, leading to a small cluster sample. Furthermore, the SV run was meant to be a test run, a time to fix any remaining issues with instrumentation or analysis methods. Due to this, galaxy data quality is not consistent across the whole SV sky. However, shape catalogs from DES's Y3 dataset—containing information from the first three years of observing—will likely be available by the end of this year, providing a more homogenous and dense galaxy sample around many of our clusters. The list of clusters cross-matched between DES Y3 and XCS is also under development, and will contain anywhere from twice to five times as many clusters as our current sample. We look forward to the use of these samples, and of course larger samples from upcoming surveys such as LSST, to measure this scaling relation with greater precision, possibly constraining the scatter as well. Should a large enough cluster sample become available ($\sim 4-5$ times the size of our current sample, with the same depth of field), our analysis method is well-prepared to (with a few modifications) constrain the $M-T_x$ scaling law independent of underlying cosmology—a step in the path of using this relation to constrain dark energy.

It has ever been in the nature of humankind to explore, to learn, to attempt to comprehend the universe we inhabit. Millenia of curiosity have revealed to us a growing, quickening cosmos, and now challenge us to understand the very fabric of space and time. We honor this legacy of learning by adding this little drop to the sea, a strand to the cosmic web of knowledge.

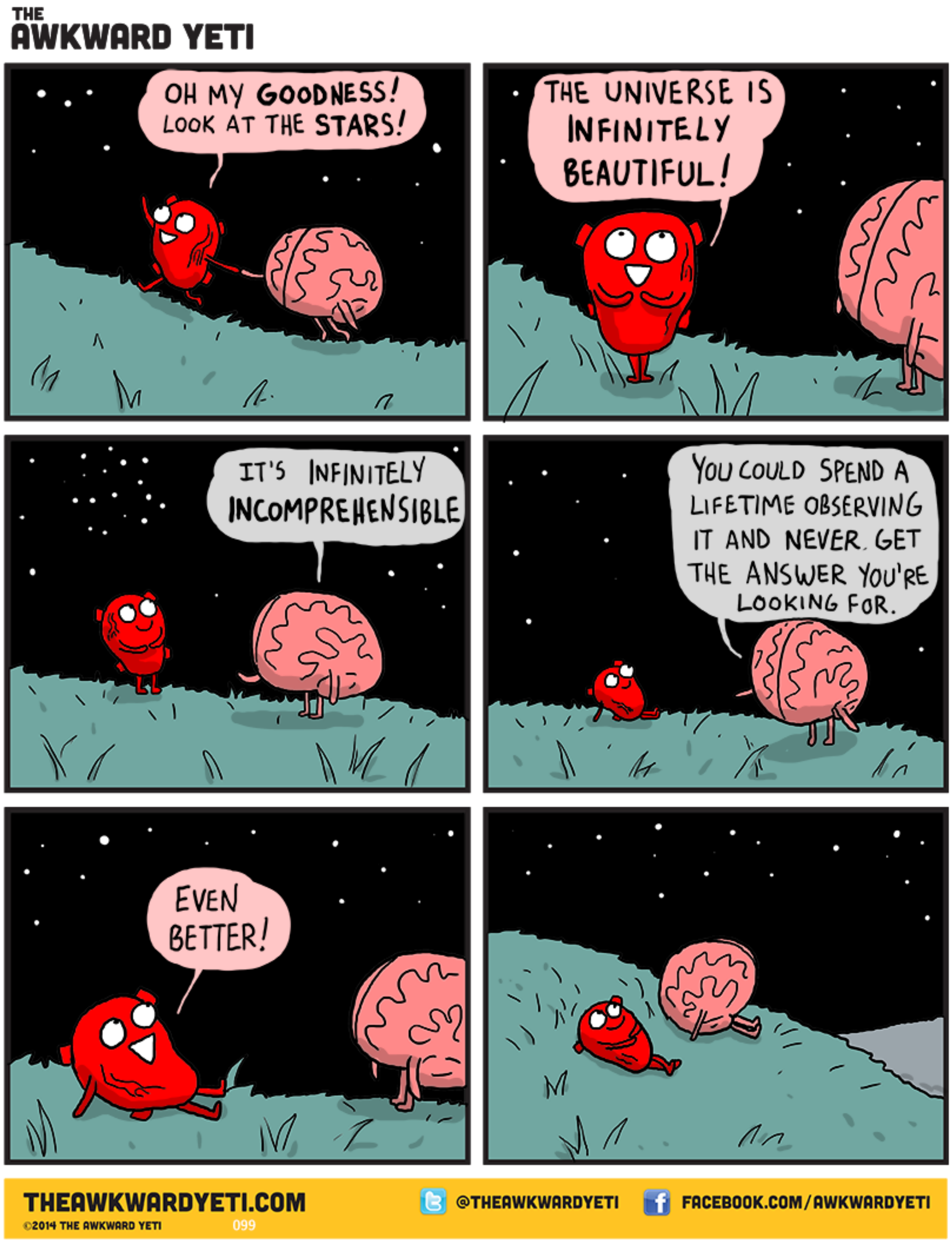

Figure 5.1 Inspiration, from http://theawkwardyeti.com/comic/stars/

APPENDICES

APPENDIX A

Accessing and Using LensStack

In this dissertation, we develop a stacked cluster weak lensing pipeline, LensStack, which enables us to incorporate clusters into our lensing analysis regardless of background data quality. Given a list of galaxy clusters, as well as background galaxy catalogs for each cluster, this code measures the stacked weak lensing mass of the list, providing tangential and perpendicular shear and $\Delta\Sigma$ measurements along the way. Further details about exact procedures can be found in Chapter III.

In this appendix, we present this pipeline for public use, and briefly describe how to run it. LensStack can be downloaded at:

https://github.com/rutudas/LensStack.git

Currently, this repository is presented as a combination of Python scripts and, after being cloned, does not require any further installation.

The repository contains the following files:

- README.md: contains everything in this appendix, as well as additional details
- measure_lensing_signal.py: measures shear and $\Delta\Sigma$ around a given stack of clusters
- fit_mass.py: finds the best-fit mass of the cluster stack

- plot_obs_fit.py: plots the best-fit model $\Delta\Sigma$, overlaid with the observed signal
- mass_conversions.py: converts between M_{200} and M_{500}
- paramfile.py: list of parameters. Some have default values, some (such as catalog locations) must be specified by user.

A.1 Python and Package Requirements

This repository was built using Python 2.7, and likely requires this version to run. We have not tested it using Python 3.x, and thus cannot comment on compatibility. Future updates may include a Python 3.x-compatible version, time allowing.

Several Python packages are required for use with this code. We require the usual list of packages associated with scientific analysis (these are included with most Python distributions):

- numpy
- math
- os
- matplotlib
- pickle
- time

We also require the following astronomy/cosmology-specific packages, some of which probably need to be separately installed:

- astropy (version 1.3.2 is compatible): generic astronomy/astrophysics package
- pyfits: package to work with FITS files
- GalSim: simulates dark matter halos, among other cosmological applications. Can be found at https://github.com/GalSim-developers/GalSim.git

A.2 Running LensStack

To run LensStack, follow these steps:

- Prepare input data files as described below.
- Enter parameters into paramfile.py
- Run measure_lensing_signal.py
- (optional) Check resulting lensing signal and decide whether to change radial binning (if so, go back to second step). Also check which radial bins to include in fitting, and adjust paramfile.py accordingly (for example, one may want to exclude the innermost radial bin if it contains too few background galaxies for proper error measurement).
- Run fit_mass.py.
- (optional) Run plot_obs_fit.py to visually examine data and fit.

A.2.1 Required Inputs

The following catalogs are required for running this pipeline, formatted as detailed:

List of Clusters

This list, formatted as a single FITS file, describes a single cluster stack. Data must be arranged into the following columns, with the specified column names (not case-sensitive):

- name: some sort of unique identifier for each cluster. Galaxy shape catalogs for each cluster will be identified using this name.
- ra: right-ascension of cluster, in degrees
- dec: declination of cluster, in degrees
- z: cluster redshift

- color_1: cluster color using two filters (we used $r - i$)
- color_2: a second cluster color, using two different filters (we used $i - z$).

Note: this code uses colorcuts to distinguish background galaxies. We use two different colorcuts—if only one set of colors is available, it must be listed twice (once labeled "color_1" and once labeled "color_2") for the code to run properly.

Set of Galaxy Shape Catalogs

This is a set of FITS files. Each file in this set should provide shape data for galaxies in the area of sky around a particular cluster. We used $80' \times 80'$ cutouts of sky around each cluster, and found the radial range sufficient even for the most nearby clusters.

Files for each cluster should be named as "["name" from cluster list].fits" and all placed in the same folder (to be specified by the user in the parameter list).

Each file should contain the following columns, with the specified column names (not case-sensitive). The essential columns are:

- ra: right-ascension of galaxy, in degrees
- dec: declination of cluster, in degrees
- e1: first component of ellipticity in the parametrization described by Eqn. 2.1
- e2: second component of ellipticity in the parametrization described by Eqn. 2.1
- mag1a: magnitude of galaxy through first filter in "color_1" from cluster catalog (in our case, r)
- mag1b: magnitude of galaxy through second filter in "color_1" from cluster catalog (in our case, i)

- mag2a: magnitude of galaxy through first filter in "color_2" from cluster catalog (in our case, i)
- mag2b: magnitude of galaxy through second filter in "color_2" from cluster catalog (in our case, z)
- z: galaxy redshift

Note: the signs on e1 and/or e2 may need to be flipped, depending on how the parametrization is defined. Neither needs a sign flip if the parametrization matches IM3SHAPE's conventions. The best way to test this is to run the code once—if a distinct positive lensing signal is returned, the parametrizations match. If only noise is returned, it is likely either e1 or e2 needs to be multiplied by -1.

We understand datasets vary, and some of the following columns may not be available. We provide information on how to format each non-essential column, in case the corresponding data is not available/relevant. To be compatible with this code, all columns must be included (this may change over future updates, but is a requirement as of now). Descriptions of most of these quantities can be found in Section 2.1.1. The non-essential columns are:

- identifier: unique galaxy identifier (not essential, but makes it easier to run follow-up checks on outputs)
- w: weight for each galaxy (if not available, set all values to 1)
- snr: signal-to-noise ratio for each galaxy (if not available, set to any constant number, and set snr_cut in parameter file to a lower number)
- rgpp_rp: R_{gp}/R_p (if not available, set to any constant number, and set rgpprp_cut in parameter file to a lower number)
- nbc_m: multiplicative noise bias correction (if not available, set all values to 0)

- nbc_c1: additive noise bias correction for e1 (if not available, set all values to 0)
- nbc_c2: additive noise bias correction for e2 (if not available, set all values to 0)
- error_flag: IM3SHAPE flag (in not available, set all values to 0)
- info_flag: IM3SHAPE flag (in not available, set all values to 0)

List of Parameters

The list of parameters, paramfile.py, contains several required components, and several components that can be run with defaults unless the user chooses otherwise.

The parameters the user must provide are:

- cluster_filename: string containing location of cluster list
- shapecat_folder: string containing location of folder containing galaxy shape catalogs
- output_folder: string containing location in which to store outputs
- run_name: an identifier given to each run, common to all scripts (outputs will be marked with this identifier, allowing multiple scripts to access the same results)

Parameters that have defaults, but can be changed:

- start: center of first radial bin
- step: width of each radial bin
- stop: where to end radial bins: bin centers are defined by np.arange(start,stop,step)
- rstart: index of first radial bin to be used for fitting
- numbin: number of radial bins to use for fitting
- masses: array of masses to use as models for fitting

Other parameters also exist, for setting data quality cuts or defining cosmology. These are further detailed in comments in paramfile.py.

A.2.2 Outputs

This pipeline provides several outputs. Running measure_lensing_signal.py returns arrays for stacked tangential and perpendicular shear and $\Delta\Sigma$, arrays for their associated errors, an array containing the number of background galaxies per cluster per radial bin, a list of background galaxy redshifts per cluster, and, for good measure, a list of all background galaxies used in the stack, with associated properties. These are all saved as pickle files. This script also outputs plots of the $\Delta\Sigma$ signal for visual inspection of results.

Running fit_mass.py returns the best-fit mass in terms of M_{200} and M_{500}, along with 1σ uncertainties, all in one pickle file. It also stores the input masses and the resulting likelihood of fits as pickle files, and plots the likelihood against the array of masses.

Running plot_obs_fit.py plots the best-fit $\Delta\Sigma$ profile, overlaying it on the observed signal.

Further details on how these arrays/files are arranged are given in the README.md file.

APPENDIX B

Running Im3shape

Upon endeavouring to measure additional shape catalogs using the tried-and-tested IM3SHAPE v9 pipeline, we were dismayed to find that no central documentation existed, even within the collaboration itself, detailing all the necessary steps (and possible pitfalls). This resulted in months of delays as we attempted to track down missing pieces of data or code, or doubled-back in the process to complete an earlier step of which we had previously been unaware. IM3SHAPE is available in the public domain for anyone to use—to prevent others from repeating these issues, and to generally document the process for future reference and experiment repeatability, we provide a list of steps detailing the necessary components of running this pipeline. This list was compiled partially by referring to the DES SV shape catalog paper (Jarvis et al. (2016)), but mostly through multiple conversations/emails with the primary authors of said work.

B.0.1 Necessary repositories/modules/programs:

IM3SHAPE and the associated noise bias calibration pipeline require several packages to function properly:

- IM3SHAPE repository: https://bitbucket.org/joezuntz/im3shape-git
- MEDS python module: https://github.com/esheldon/meds

- FITSIO python module: https://github.com/esheldon/fitsio
- UCL_DES_SHEAR_GIT - https://bitbucket.org/joezuntz/ucl_des_shear_git
- GREAT-DES repository: https://github.com/tomaszkacprzak/GREAT-DES
- TKTOOLS repository: https://github.com/tomaszkacprzak/tktools
- GalSim: https://github.com/GalSim-developers/GalSim.git

B.0.2 Steps to Measure Shapes

Necessary Inputs

In order to run Im3shape, one must start with:

- MEDS files for the areas of sky to be examined
- PSF measurements at the positions of objects for every exposure in the MEDS file
- PSF blacklist: a list of exposures for which PSF measurements failed—to be used to exclude these exposures from shape measurements

See Section 2.1 (or Sections 4 and 5, and Appendix A, of Jarvis et al. (2016)) for more details on these files and measurements.

The PSF information must then be added to the MEDS file. This can be done using a script in the UCL_DES_SHEAR_GIT repository: ucl_des_shear_git/utils/meds_tools /collect_psf.py by running the following command in a terminal:

```
python collect_psf.py meds.txt v4
```

Here, "meds.txt" is a text file containing paths to the MEDS files to be run (one on each line). Unfortunately, it seems as though this script is specialized to be used with DES —the "v4" refers to the version of PSF runs, and this script must be run in a particular online DES repository. However, it may be possible to modify it slightly for use in other filesystems—one would have to contact Joe Zuntz, the creator of this repository and Im3shape (contact information available through the official repository pages).

Running Im3shape

Once we have the MEDS files, with PSF information added, we can move on to running the Im3shape pipeline. To measure shapes for a MEDS file, run the following command in a terminal:

```
python -m py3shape.analyze_meds $MEDS $INI $CAT $OUT $RANK $SIZE
```

- MEDS is the path to the MEDS file
- INI is a parameter file. The required parameters are described in the Im3shape readme file.
- CAT is a text file containing a list of object identifiers that tells Im3shape which objects to run on. These should match up with object identifiers in the MEDS file. If running for all objects in the MEDS file, we can type "all" in place of CAT.
- OUT is the base name for the output, which includes both the directory for the output and a name for the run. For example, if OUT is 'some_folder/results' then the output files will be stored in some_folder, and the filenames will be 'results.main.txt' and 'results.epoch.txt'.
- RANK and SIZE are integers with RANK¡SIZE. This will assume that the job is to be split up into SIZE separate chunks and that this command is number RANK in that group (starting at 0).

As mentioned in Section 2.1.1, this pipeline fits each galaxy to both bulge and disc models, keeping the result with the maximum likelihood. In order to do this, the above command must be run twice for all galaxies, once for the bulge model and once for the disc model. The model to be used is specified in the INI parameter file.

Note: This method of running Im3shape focuses on examining MEDS files one at a time. If one wants to examine multiple MEDS files at once, this can be done through the use of mpi4py. The functionality is built into the pipeline, and further details on that procedure can be obtained by examining the Im3shape readme file or by contacting the creator of the pipeline, Joe Zuntz (contact information available through the official repository).

Postprocessing

The outputs from each run of Im3shape are two catalogs, named [OUT].main.txt and [OUT].epoch.txt. The "main" file contains the measured shapes and corrections, while the "epoch" file contains information about every exposure used to fit each galaxy. These catalogs must go through postprocessing to choose between the bulge and disc models, and to format them for the next steps. In order to avoid researcher's bias during data analysis, this postprocessing also blinds the catalogs, multiplying each e1 and e2 by some number between .9 and 1 (the same number for all galaxies), as described in Section 7.5 of Jarvis et al. (2016). Postprocessing follows these steps:

- import the necessary scripts into a python environment, using "from des_post. postprocess import process_text". des_post is a subdirectory of the ucl_des_shear_git) package.
- run the following command in python:

process_text(main_file, epoch_file, out_main, out_epoch, band, blind=True,quiet=True, report=False)

The first two inputs are the raw Im3shape outputs, "out_main" and "out_epoch" are paths to where the postprocessed catalogs should be saved, and band is the filter used for measuring shapes ('g', 'r', 'i', or 'z'). The outputs are FITS files, and should be named as such.

- now we run the merging code that chooses between the bulge and disc models. Import the module in python: "from des_post.merge_bulge_disc import merge"
- run the following command in python:

  merge(bulge_main, bulge_epoch, disc_main, disc_epoch, bord_main, bord_epoch)

  The first four files are the postprocessed result files from the previous step. "bord_main" and "bord_epoch" are the names that will be given to the merged output files, again in FITS format.

Noise Bias Calibration

The final step is to apply the noise bias correction described in Section 7.3 of Jarvis et al. (2016). In a terminal, run:

python /GREAT-DES/nbc-v7/nbc_v7.py -c nbc.yaml -a apply_calibration_to_file –filename_to_calibrate [filename]

The [filename] should be the postprocessed merged "bord_main" file. The "nbc.yaml" file can be found in the same directory as this script. The output file will automatically be placed in the same folder as the input file. Its name will be the same as the input file's, with the letters "nbc" inserted before the ".fits" extension.

The output of this step gives the final shape catalog for the analyzed MEDS file. All included columns of the catalog are described in the documentation for the official release of DES-SV shapes[1]. After many measurements and corrections, we are done.

[1] https://des.ncsa.illinois.edu/releases/sva1

Bibliography

Ade, P. A. R., Aghanim, N., Arnaud, M., et al. 2011, Astronomy & Astrophysics, 536, A11

Arnaud, M., Pointecouteau, E., & Pratt, G. W. 2005, Astronomy and Astrophysics, 441, 893

Bassett, B. A., & Hlozek, R. 2009, Baryon Acoustic Oscillations, 42, arXiv:0910.5224

Bertin, E. 2011, Astronomical Data Analysis Software and Systems XX, 442, 435

Bertin, E., & Arnouts, S. 1996, Astronomy and Astrophysics Supplement Series, 117, 393

Bower, R. G., Lucey, J. R., & Ellis, R. S. 1992, Monthly Notices of the Royal Astronomical Society, 254, 601

Bryan, G. L., & Norman, M. L. 1998, The Astrophysical Journal, 1, 80

Das, R., Collaboration, D. E. S., & Group, X. C. S. in prep., 1

DeRose, J., Wechsler, R., & Busha, M. T. in prep.

DES Collaboration, Abbott, T. M. C., Abdalla, F. B., et al. submitted, arXiv:1708.01530

Eckmiller, H. J., Hudson, D. S., & Reiprich, T. H. 2011, Astronomy & Astrophysics, 535, A105

Efron, B. 1982, The Jackknife, the Bootstrap and Other Resampling Plans (Society for Industrial and Applied Mathematics), https://epubs.siam.org/doi/pdf/10.1137/1.9781611970319

Fabian, A. C. 1994, Annual Review of Astronomy and Astrophysics, 32, 277

Flaugher, B., Diehl, H. T., Honscheid, K., et al. 2015, Astronomical Journal, 150, arXiv:1504.02900

Henning, J. W., Gantner, B., Burns, J. O., & Hallman, E. J. 2009, Astrophysical Journal, 697, 1597

Hoekstra, H., Bartelmann, M., Dahle, H., et al. 2013, Space Science Reviews, 177, 75

Hoekstra, H., & Jain, B. 2008, arXiv:0805.0139

Howell, D. A. 2011, Nature Communications, 2, 310

Hu, W. 2001, arXiv:0210696v1

Hu, W., & Kravtsov, A. V. 2003, The Astrophysical Journal, 584, 702

Huterer, D., & Shafer, D. L. 2018, Reports on Progress in Physics, 81, arXiv:1709.01091

Jarvis, M., Sheldon, E., Zuntz, J., et al. 2016, Monthly Notices of the Royal Astronomical Society, 460, 2245

Johnston, D. E., Sheldon, E. S., Tasitsiomi, A., et al. 2007a, The Astrophysical Journal, 656, 27

Johnston, D. E., Sheldon, E. S., Wechsler, R. H., et al. 2007b, arXiv:0709.1159

Kaiser, N. 1986, Monthly Notices of the Royal Astronomical Society, 222, 323

Kettula, K., Finoguenov, A., Massey, R., et al. 2013, Astrophysical Journal, 778, 74

Lloyd-Davies, E. J., Romer, A. K., Mehrtens, N., et al. 2011, Monthly Notices of the Royal Astronomical Society, 418, 14

Mahdavi, A., Hoekstra, H., Babul, A., et al. 2013, Astrophysical Journal, 767, arXiv:1210.3689

Manolopoulou, M., Hilton, M., Giles, P. A., et al. in prep.

Mantz, a., Allen, S. W., Ebeling, H., Rapetti, D., & Drlica-Wagner, a. 2010, Monthly Notices of the Royal Astronomical Society, 406, 1773

Mcclintock, T., Varga, T. N., Gruen, D., et al. submitted, arXiv:arXiv:1805.00039v1

Medezinski, E., Oguri, M., & Nishizawa, A. J. 2018, Publications of the Astronomical Society of Japan, arXiv:1706.00427

Mehrtens, N., Romer, A. K., Hilton, M., et al. 2012, Monthly Notices of the Royal Astronomical Society, 423, 1024

Melchior, P., Gruen, D., McClintock, T., et al. 2017, Monthly Notices of the Royal Astronomical Society, 469, 4899

Merten, J., Meneghetti, M., Postman, M., et al. 2015, The Astrophysical Journal, 806, 4

Miralda-Escude, J. 1991, The Astrophysical Journal, 370, 1

Navarro, J. F., Frenk, C. S., & White, S. D. M. 1996, The Astrophysical Journal, 462, 563

Okabe, N., Takada, M., Umetsu, K., Futamase, T., & Smith, G. P. 2010, Publications of the Astronomical Society of Japan, 62, 811

Old, L., Skibba, R. A., Pearce, F. R., et al. 2014, Monthly Notices of the Royal Astronomical Society, 441, 1513

Old, L., Wojtak, R., Mamon, G. A., et al. 2015, Monthly Notices of the Royal Astronomical Society, 449, 1897

Pereira, M. E. S., Soares-Santos, M., Makler, M., et al. 2017, MNRAS, 1372, 1361

Rasmussen, J., & Ponman, T. J. 2007, Monthly Notices of the Royal Astronomical Society, 380, 1554

Rowe, B. T., Jarvis, M., Mandelbaum, R., et al. 2015, Astronomy and Computing, 10, 121

Rykoff, E. S., Rozo, E., Busha, M. T., et al. 2014, Astrophysical Journal, 785, arXiv:1303.3562

Sánchez, C., Carrasco Kind, M., Lin, H., et al. 2014, Monthly Notices of the Royal Astronomical Society, 445, 1482

Sarazin, C. 1988, Cambridge Astrophysics Series, doi:10.1103/RevModPhys.58.1

Sheldon, E. S., Annis, J., Bo, H., et al. 2001, The Astrophysical Journal, 554, 881

Stern, C., Dietrich, J. P., Bocquet, S., et al. submitted, arXiv:1802.04533

Sun, M., Voit, G. M., Donahue, M., et al. 2009, Astrophysical Journal, 693, 1142

Sunyaev, R., & Zeldovich, Y. 1972, The Observation of Relic Radiation as a Test of the Nature of X-Ray Radiation from the Clusters of Galaxies

Viana, P. T., Mehrtens, N., Harrison, C. D., et al. 2013, Astronomische Nachrichten, 334, 462

Vikhlinin, A., & Kravtsov, A. 2006, The Astrophysical Journal, 640, 691

Vikhlinin, A., Burenin, R. A., Ebeling, H., et al. 2009a, The Astrophysical Journal, 692, 1033

Vikhlinin, A., Kravtsov, A. V., Burenin, R. A., et al. 2009b, The Astrophysical Journal, 692, 1060

Voit, G. M. 2005, Reviews of Modern Physics, 77, 207

Wechsler, R., DeRose, J., & Busha, M. T. in prep.

Weinberg, D. H., Mortonson, M. J., Eisenstein, D. J., et al. 2013, Physics Reports, 530, 87

Wright, C. O., & Brainerd, T. G. 2000, The Astrophysical Journal, 534, 34

Zhang, Y., Miller, C., Mckay, T., et al. 2016, Astrophysical Journal, 816, 98

Zuntz, J., Sheldon, E., Samuroff, S., et al. submitted, arXiv:1708.01533